

FILE COPY APOS.R.TK. 89-0568

RECEIVED
MAY 15 1989

D

Final Scientific Report

AFOSR Grant No. 85-0146

February 6, 1985 to August 5, 1988

EXPERIMENTAL AND NUMERICAL INVESTIGATION OF COHERENT STRUCTURES IN TURBULENT WAKE FLOWS

Submitted to:

Air Force Office of Scientific Research

Submitted by:

Dr. Frank H. Champagne, Professor
Department of Aerospace and
Mechanical Engineering

UNCLASSIFIED

SECURITY CLASSIFICATION OF THIS PAGE

ADA207866

REPORT DOCUMENTATION PAGE

1a. REPORT SECURITY CLASSIFICATION Unclassified		1b. RESTRICTIVE MARKINGS	
2a. SECURITY CLASSIFICATION AUTHORITY		3. DISTRIBUTION/AVAILABILITY OF REPORT Approved for public release, Distribution unlimited	
2b. DECLASSIFICATION/DOWNGRADING SCHEDULE			
4. PERFORMING ORGANIZATION REPORT NUMBER(S)		5. MONITORING ORGANIZATION REPORT NUMBER(S) # AFOSR-TR-89-6568	
6a. NAME OF PERFORMING ORGANIZATION University of Arizona	6b. OFFICE SYMBOL (If applicable) NA	7a. NAME OF MONITORING ORGANIZATION AFOSR/NA Bolling AFB, DC 20339	
8c. ADDRESS (City, State and ZIP Code) Aerospace and Mechanical Engineering Building #16 Tucson, Arizona 85721		7b. ADDRESS (City, State and ZIP Code) # Same as 8c	
8a. NAME OF FUNDING/SPONSORING ORGANIZATION AFOSR	8b. OFFICE SYMBOL (If applicable) NA	9. PROCUREMENT INSTRUMENT IDENTIFICATION NUMBER AFOSR-85-0146	
8c. ADDRESS (City, State and ZIP Code) Bolling Air Force Base Division of Air Force Science, Bldg. 410 Washington, D. C. 20332-6448		10. SOURCE OF FUNDING NOS. PROGRAM ELEMENT NO. 61102F PROJECT NO. 2307 TASK NO. A2 WORK UNIT NO.	
11. TITLE (Include Security Classification) Experimental and Numerical Investigation of Coherent Structures in Turbulent Wake Flows			
12. PERSONAL AUTHOR(S) Dr. Frank H. Champagne			
13a. TYPE OF REPORT Final Scientific	13b. TIME COVERED FROM 2-6-85 TO 8-5-88	14. DATE OF REPORT (Year, Month, Day) 89/4/28	15. PAGE COUNT 78
16. SUPPLEMENTARY NOTATION N/A			
17. COSATI CODES		18. SUBJECT TERMS (Continue on reverse if necessary and identify by block number)	
FIELD	GROUP	SUB. GR.	
19. ABSTRACT (Continue on reverse if necessary and identify by block number) Large scale coherent structures have been observed in two-dimensional wakes behind bluff bodies as well as non-vortex shedding bodies. There is a strong indication that these large scale structures are related to the two-dimensional instability modes of the slowly diverging mean wake flow. The Orr-Sommerfeld equation admits two solution modes for the two-dimensional plane wake. These are the sinuous mode with antisymmetric streamwise fluctuations and the varicose mode with symmetric streamwise fluctuations. The wake response to controlled sinuous and varicose types of disturbance waves was investigated. Sinuous disturbances at several amplitudes and frequencies were introduced to the wake of a flat plate by oscillating a small trailing edge flap. The Strouhal numbers of the disturbance waves were specially chosen so that the downstream location of the neutral point was well within the range of measurements. The streamwise variation of the half width of the wake and the centerline deficit was dependent on the amplitude level and showed dramatic deviations, starting near the neutral point, at large forcing levels from the well known square root behavior of the			
20. DISTRIBUTION/AVAILABILITY OF ABSTRACT UNCLASSIFIED/UNLIMITED <input checked="" type="checkbox"/> SAME AS RPT. <input type="checkbox"/> DTIC USERS <input type="checkbox"/>		21. ABSTRACT SECURITY CLASSIFICATION # UNCLASSIFIED	
22a. NAME OF RESPONSIBLE INDIVIDUAL Dr. James J. McMichael		22b. TELEPHONE NUMBER (Include Area Code) (202)767-4935	22c. OFFICE SYMBOL AFOSR/NA

19. Abstract (continued)

unforced case. The measured coherent Reynolds stresses were observed to change sign in the neighborhood of the neutral point as predicted from linear stability theory. The extent of the validity of linear stability theory was investigated. The wake was also forced with a sinuous disturbance of lower Strouhal number that was amplified over the entire range of measurements. The linear and nonlinear evolution of the sinuous wave was studied. A perturbation analysis was carried out to determine the interaction of the fundamental wave with the mean flow and the generation of the first harmonic. The measured mean flow distortion and first harmonic were reasonably well predicted from the analysis.

The varicose mode, which is often ignored because its amplification rates are considerably less than those of the sinuous mode, was also investigated experimentally. Combined model forcing experiments on the wake were undertaken to study the interaction between modes. No nonlinear interactions between the two modes seemed to be present, at least in the experiments performed. An eddy viscosity model, coupled with the slowly diverging linear equations, predicts the streamwise variation of both modes reasonably well and describes the transverse distributions of the perturbation amplitudes for both modes, but it fails to predict the distribution of phase for the varicose mode.

INTRODUCTION

The stability of free shear flows has been studied by many investigators in the last several decades. The challenge of understanding the transition phenomenon provided the initial incentive to apply the ideas of stability theory to two-dimensional wakes. The laminar wake velocity profile has inflection points and is dynamically unstable. The stability of the mean velocity profile in a turbulent wake is of interest because it also contains inflection points. In the far wake flow field, the turbulent fluctuations are quite small in comparison to the instantaneous streamwise velocity component, so the mean velocity profile is very similar to that of the instantaneous velocity. The two-dimensional turbulent wake flow is a good test case for examining the possible link between the instability modes of the Orr-Sommerfeld equation and the large scale coherent structures observed in fully turbulent wake flows.

The present work, in many respects, is a continuation of the work described in Wygnanski, Champagne and Marasli (1986). The main objectives of the present research were to experimentally study the response of a turbulent wake of a flat plate to spatially traveling disturbance waves, to determine the applicability of linear stability theory to describe the evolution of the disturbance waves, and to attempt to describe the non-linear effects of mean flow distortion and the generation of a harmonic using a perturbation analysis.

The Orr-Sommerfeld equation admits two solution modes for the two-dimensional plane wake. These are the sinuous mode with antisymmetric streamwise disturbances and the varicose mode with symmetric streamwise disturbances. The varicose mode is often ignored because its amplification rates are considerably less than those of the sinuous mode. Our earlier measurements, presented in Wygnanski et al. (see attached paper), were limited to one sinuous case with a particular frequency and amplitude. In the present study, both sinuous and varicose disturbances of various frequencies and amplitudes were introduced into the turbulent wake of a flat plate. For details on the plate, see the attached papers.

SINUOUS MODE

A 40Hz sinuous wave was first studied. The sinuous disturbance waves were introduced into the wake by oscillating a small flap attached to the trailing edge of the plate. The unforced (base) flow field was measured with the flap at rest aligned with the axis of the plate. The 40Hz wave was chosen as a linear stability analysis of the base flow indicated that this wave would be amplified over the entire range of measurements. A triple decomposition was used to determine the coherent (wave), random, and mean parts of any velocity component signal. The forcing level, defined as $(\bar{u}_{rms}/u_0)_{max}$, where u_0 is the centerline velocity deficit, was 15% at the initial measurement location, $x = 10$ inches. \bar{u} is the coherent or wave contribution to the streamwise velocity component. This forcing level was termed low. The mean growth rate of the forced wake was initially the same as that for the unforced wake, but as the introduced disturbance wave amplifies as it moves downstream, the rate of growth of the wake increases. The coherent Reynolds stress augments the turbulent Reynolds stress which in turn can be related to the rapid divergence of the forced wake through the time averaged streamwise momentum equation (see Marasli, 1989). In the range of measurements considered, the nonlinear interactions are not strong enough to affect the shape of the normalized mean velocity profile, but the initial effects

of nonlinearity are observed in the increased spreading rate of the wake. Stability calculations to determine amplification curves for both the unforced and forced cases were performed. The transverse distribution of the amplitudes and phases of the streamwise and lateral velocity components of the perturbation wave were computed from linear stability theory using the measured mean velocity profiles. Both viscous and inviscid calculations were made, but as the eigenfunction shapes for the sinuous mode are relatively insensitive to Reynolds number, only the inviscid results are required. Agreement between the experiments and theory is excellent especially in the early stages where the nonlinearity has not affected the flow significantly. Finally, a perturbation analysis along the lines of that presented by Cohen and Wygnanski (1987) was developed to study the interaction between the fundamental wave and the mean flow and the generation of the first harmonic. The details of the analysis and comparison with experimental results are presented in Marasli (1989). The general features of the mean flow distortion and first harmonic were predicted successfully by the analysis.

Sinuous disturbances at several amplitudes and frequencies were introduced into the wake to attempt to control the growth rate of the turbulent wake behind the flat plate. The Strouhal numbers of the disturbances were specially chosen so that the downstream location of the neutral point (where the spatial amplification rate obtained from linear stability theory vanishes) was well within the range of measurements. The streamwise variation of the half width of the wake and the centerline velocity deficit was dependent on the amplitude level and showed dramatic deviations (starting from the neutral point) at large forcing levels from the well known square root behavior of the unforced case. The measurement coherent Reynolds stresses were observed to change sign in the neighborhood of the location of the neutral point as predicted from linear viscous theory. Data sets with similar amplitude of forcing but different frequencies and free stream velocities collapse on one curve by a suitable definition of Strouhal number. The extent of the validity of linear theory to describe the problem is discussed in an attached paper titled "Effect of Spatially Traveling Sinuous Waves on the Growth of a Two-Dimensional Turbulent Wake". This paper has been accepted for presentation at the Fourth Asian Congress of Fluid Mechanics to be held in Hong Kong this summer.

VARICOSE MODE

In our earlier experiments reported in Wygnanski et al. (1986), we studied the sinuous mode in the wake of the flat plate. Some aspects of the evolution of the disturbance waves, like the local transverse profile shape of the disturbance eigenfunction and the streamwise growth of the disturbance waves, were predicted well by linear, inviscid stability theory. It is conjectured that a combination of many waves of different frequencies, generated from the instability of the mean velocity profile, eventually constitute the turbulent field. The centerline streamwise turbulence intensity in a two-dimensional turbulent wake is non-zero while the u -component of the sinuous mode is identically zero on the centerline. Therefore, the sinuous mode alone was thought by Wygnanski et al. to be inadequate to describe the turbulent field. Thus the varicose mode was presumed to have some importance in the overall picture, since the u -component of this mode has a maximum at the centerline. Streamline calculations performed by Wygnanski et al. using a combination of the two modes revealed structures that resembled the smoke wire picture taken in the unforced wake of the flat plate. Further, flow visualization pictures taken in

the near wakes of various bodies by several authors have shown flow patterns that could be attributed to the varicose mode. Therefore, an experimental investigation of the varicose mode was undertaken to clarify some of the above points.

It should be pointed out that the presence of the varicose mode is not necessary for non-zero turbulence intensity at the wake centerline. The nonlinear interaction of a fundamental sinuous wave with itself generates a first harmonic that has a symmetric u -component with a maximum at the centerline. This would support the contention that the sinuous mode alone is in fact adequate to describe the entire turbulent field.

The varicose mode was generated by oscillating two flaps 180° out of phase. The flaps were placed symmetrically above and below the plate. The experiments demonstrated that, although it is possible to generate a nearly pure symmetric disturbance wave, it is very difficult to do as the flow is very sensitive to the slightest asymmetries which might be present in the experiments. These asymmetries are preferentially amplified, resulting in the eventual distortion of an initially prominent symmetric wave. It was therefore necessary to decompose phase averaged measurements of the streamwise component of the velocity fluctuations into their symmetric and antisymmetric parts, and the results were compared with the appropriate theoretical eigenfunctions from linear stability theory. The lateral distribution of the amplitude and the phase of each mode agree reasonably well with their theoretical counterparts from the Orr-Sommerfeld equation. Slowly diverging linear theory predicts the streamwise variation of the sinuous mode quite well, but fails to do so for the varicose mode. An eddy viscosity model, coupled with the slowly diverging linear equations, predicts the streamwise variation of both modes reasonably well and describes the transverse distributions of the perturbation amplitudes for both modes, but it fails to predict the distribution of phase for the varicose mode. Further details can be found in the attached JFM paper "Model Decomposition of Velocity in a Plane, Turbulent Wake".

REFERENCES

1. Wygnanski, I., Champagne, F., and Marasli, B., 1986, J. Fluid Mech. 168, 31-71.
2. Marasli, B., "Spatially Traveling Waves in a Two-Dimensional Wake," Ph.D Thesis, University of Arizona, 1989.
3. Cohen, J. and Wygnanski, I. 1987, J. Fluid Mechanics, 176, 191-220.
4. Marasli, B., Champagne, F. H., and Wygnanski, I. J., 1989, J. Fluid Mech., 198, 255-273.

Modal decomposition of velocity signals in a plane, turbulent wake

By B. MARASLI, F. H. CHAMPAGNE AND I. J. WYGNANSKI

Department of Aerospace and Mechanical Engineering, University of Arizona,
Tucson, AZ 85721, USA

(Received 9 October 1986 and in revised form 5 March 1988)

The Orr-Sommerfeld equation admits two solution modes for the two-dimensional plane wake. These are the sinuous mode with antisymmetric streamwise fluctuations and the varicose mode with symmetric streamwise fluctuations. The varicose mode is often ignored because its amplification rates are considerably less than those of the sinuous mode. An experimental investigation of the varicose mode in a two-dimensional turbulent wake was undertaken to determine if this mode of instability agrees as well with linear stability theory, as did the sinuous mode in previous experiments (Wygnanski, Champagne & Marasli 1986). The experiments demonstrated that, although it is possible to generate a nearly pure symmetric disturbance wave, it is very difficult to do as the flow is very sensitive to the slightest asymmetries which might be present in the experiments. These asymmetries are preferentially amplified, resulting in the eventual distortion of an initially prominent symmetric wave. It was therefore necessary to decompose phase-averaged measurements of the streamwise component of the velocity fluctuations into their symmetric and antisymmetric parts, and the results were compared with the appropriate theoretical eigenfunctions from linear stability theory. The lateral distribution of the amplitude and the phase of each mode agree reasonably well with their theoretical counterparts from the Orr-Sommerfeld equation. Slowly diverging linear theory predicts the streamwise variation of the sinuous mode quite well, but fails to do so for the varicose mode. An eddy-viscosity model, coupled with the slowly diverging linear equations, predicts the streamwise variation of both modes reasonably well and describes the transverse distributions of the perturbation amplitudes for both modes, but it fails to predict the distribution of phase for the varicose mode.

1. Introduction

Large-scale coherent structures in the small-deficit wake behind a flat plate were observed by Wygnanski, Champagne & Marasli (1986) using combined hot-wire and flow-visualization techniques.† Evidence was presented that these large-scale structures, which resemble the Kármán vortex street in appearance, can be described

† Note the following corrections to Wygnanski *et al.* (1986):

- (i) In table 1, the value of θ for the 6.35 mm diameter cylinder at a Reynolds number of 5800 is 3.51 mm, not 2.64 mm.
- (ii) Equation (2.3) should read:

$$V(t) = \frac{P_1(E_1) - P_2(E_2)}{(A_{3,2} - A_{3,1})}, \quad U(t) = P_1(E_1) + A_{3,1}V.$$

by linear stability theory. Theoretical calculations based on linear, inviscid stability theory showed excellent agreement with the measured transverse distributions of amplitudes and phases of externally imposed sinuous waves on the fully turbulent wake behind the flat plate. When the divergence of the mean flow was incorporated into the analysis, the spatial amplification of the sinuous waves in the streamwise direction was successfully predicted. Although the sinuous disturbances represent the predominant mode of instability from linear theory, the possible importance of the varicose disturbances (those that have a symmetrical streamwise component about the wake centreline) was considered. Varicose disturbances have relatively smaller amplification rates and are usually neglected in stability analyses. The varicose mode, however, may at times dominate the shape of the large structures (Papailiou & Lykoudis 1974; Rockwell, Ongoren & Unal 1985; Williamson 1985) and, even when the prevailing instability is mainly sinuous in nature, a small varicose component was shown to alter the gross behaviour of the calculated streakline patterns (Wygnanski *et al.* 1985). The latter provided the initial motivation for the present study, the purpose of which is to investigate the significance of the varicose mode in two-dimensional, small-deficit, turbulent wakes. One should note that the varicose mode has not been investigated experimentally in either laminar or turbulent wakes, and its existence was by no means assured, particularly in a fully turbulent environment.

2. Description of experiments

The wakes were generated in the University of Arizona's low-speed wind-tunnel facility. The zero-pressure-gradient test section is nominally 61 by 91 cm in cross-section and 6 m long. The speed in the test section was 7.5 m/s for the present experiments, while the free-stream disturbance level in the streamwise velocity component was 0.03 %. The tunnel is equipped with chilled water coils to maintain the temperature of the flow constant. The flat-plate wake generator was a solid aluminium plate 30 cm long, 61 cm wide, and 0.635 cm at its point of maximum thickness. The leading edge was rounded, and the trailing edge was tapered to 1 mm thickness over the last 10 cm of the plate surface. Trip wires, placed 3 cm from the leading edge, generated a turbulent boundary layer before the tapered section was reached. The Reynolds number based on the momentum thickness, θ , was approximately 1400 for the present data.

In the previous experiments by Wygnanski *et al.* (1986), sinuous waves were generated by oscillating a small flap (5 mm in length) hinged to the trailing edge of the plate. For the present experiments, sinusoidal varicose disturbances, which are symmetrically distributed about the wake centreline, were generated by oscillating two small flaps 180° out of phase. The flaps were placed symmetrically above and below the plate, approximately 18 cm from the leading edge and just upstream of the tapered trailing-edge region of the plate, as indicated by the sketch shown in figure 1. The insert shown in figure 1 presents details of the flap arrangement. The dashed lines show the maximum range of motion of the flaps, which was set such that the flaps did not touch the plate. Scotch tape was used as the hinge to attach the flaps to the ramps. Nylon ribbons were used to connect the downstream edge of each side of the flaps to matched loudspeakers, which were located on each side of the plate just outside the tunnel sidewalls. The forcing level is specified by the maximum value of the measured r.m.s. of the streamwise component of the perturbation wave at $x/\theta = 200$. For the varicose mode, the maximum occurs at the centreline.

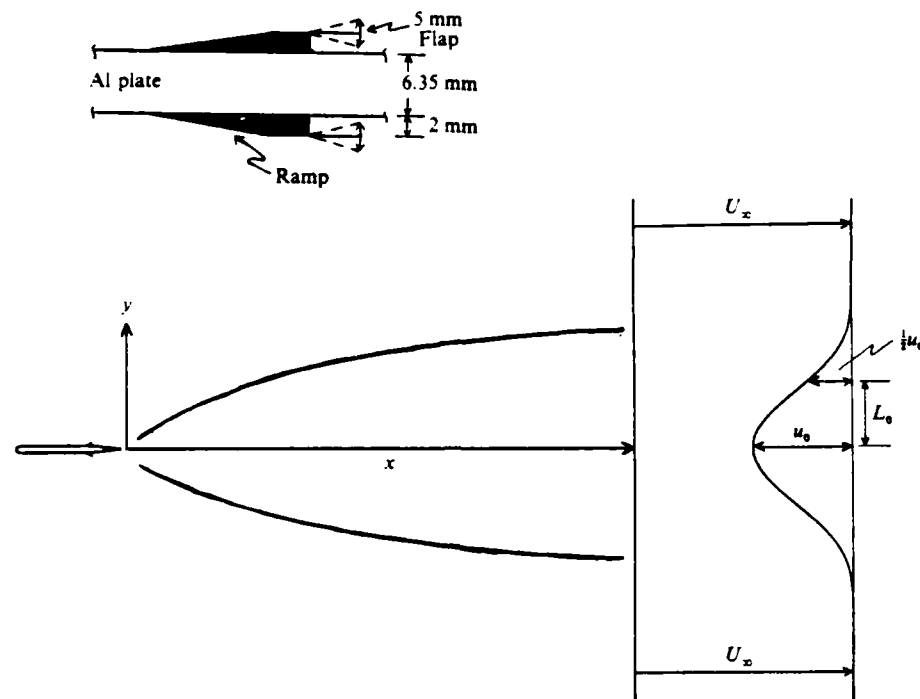


FIGURE 1. Schematic of plate and wake defining the nomenclature. The insert shows the details of the flap arrangement.

3. Theoretical background

The instantaneous streamwise (u) component velocity signal is represented by

$$\bar{U} = \bar{U} + \bar{u} + u', \quad (1)$$

where \bar{U} is the mean or time-averaged part, \bar{u} is the periodic wave contribution, and u' is the turbulent part (Reynolds & Hussain 1972). Another quantity that will be referred to often is the total fluctuating signal,

$$u = \bar{u} + u'. \quad (2)$$

Assume that the perturbation stream function for a wavy disturbance superimposed on a parallel flow $\bar{U}(y)$ has the form

$$\psi(X, \eta, t) = \text{Re}[\phi(\eta) e^{i(xX - \beta t)}]. \quad (3)$$

where $X = x/L_0$, $\eta = y/L_0$, $\beta = 2\pi f L_0 / U_x$ is the non-dimensional frequency and $x = \alpha_r + i\alpha_i$ is a non-dimensional complex quantity whose real part represents the wavenumber while its imaginary part represents the spatial amplification rate: x is non-dimensionalized by L_0 . The growth or decay of such disturbances, as long as they remain sufficiently small to permit linearization of the equations of motion, are governed by the Orr-Sommerfeld equation which, in non-dimensional form, is given by

$$\left(U^* - \frac{\beta}{x} \right) (\phi'' - x^2 \phi) - U^{**} \phi - \frac{1}{i\alpha R \rho} (\phi''' - 2x^2 \phi'' + x^4 \phi) = 0. \quad (4)$$

where $U^* = U/U_x$; Re is the Reynolds number of the basic flow, chosen here to be $U_x L_0/\nu$; U_x is the free-stream velocity; L_0 is the wake half-width (see figure 1); and ν is the kinematic viscosity.

At large values of the transverse coordinate, i.e. $\eta \rightarrow \pm \infty$, $U^* \rightarrow 1$, and $U^{**} \rightarrow 0$, equation (4) reduces to

$$\phi'' - [\gamma^2(\eta) + \alpha^2] \phi'' + \alpha^2 \gamma^2(\eta) \phi = 0. \quad (5)$$

where $\gamma^2(\eta) = i\alpha Re(U^* - \beta/\alpha) + \alpha^2$. This equation has four independent solutions for each side of the flow, which can be described by

$$\phi(\eta) = \sum_{n=1}^4 A_n e^{i\eta p_n} \quad \text{as} \quad \eta \rightarrow -\infty, \quad \phi(\eta) = \sum_{n=1}^4 B_n e^{i\eta q_n} \quad \text{as} \quad \eta \rightarrow +\infty. \quad (6)$$

where

$$p_{1,2} = \pm \alpha, \quad p_{3,4} = \pm \gamma(-\infty),$$

$$q_{1,2} = \pm \alpha, \quad q_{3,4} = \pm \gamma(+\infty).$$

The disturbances must decay exponentially with increasing distance from the centreline of the wake, and this decay leads to $A_2 = A_4 = B_1 = B_3 = 0$.

In order to satisfy these boundary conditions, a shooting technique described by Betchov & Szweczyk (1963) is used for low Reynolds numbers ($U_x L_0/\nu < 800$). For large Reynolds numbers, a Gram-Schmidt orthonormalization technique is used, as described by Bellman & Kalaba (1985) and utilized by Wazzan, Okamura & Smith (1968) and others.

The inviscid case is much simpler and the boundary conditions are

$$\phi' \pm i\alpha\phi = 0. \quad (7)$$

for $\eta \rightarrow \pm \infty$, which requires the disturbance to decay exponentially on both sides of the wake.

4. Generation of varicose mode

It was extremely difficult to generate purely symmetrical disturbances because any lack of symmetry in the generating mechanism resulted in a combination of modes. The results of one attempt to generate a pure varicose mode are given in figure 2. Data on the transverse distributions of \bar{u}^2/u_0^2 for downstream locations in the range $100 < x/\theta < 1400$ are shown. The flaps were driven 180° out of phase at 35 Hz, and a rake of nine hot wires was used to obtain the data. This excitation frequency corresponds to a Strouhal number based on momentum thickness, $St = f\theta/U_x$, of 0.0127. The maximum value of the r.m.s. of the u -component of the perturbation velocity at $x/\theta = 200$ was $(\bar{u}_{rms}/u_0)_{max} = 11.7\%$. The data indicate that the flow is self-preserving, but the self-preserving distribution for this case differs slightly from that for the unforced case (\bar{u}^2/u_0^2), which is shown in figure 3 for comparison. The flow in both cases is fully turbulent and, in the forced case, only $\sim 10\%$ of the total fluctuations are coherent, which is also reflected by comparing the maximum value of $(\bar{u} + u')^2/u_0^2$ for the forced case and \bar{u}^2/u_0^2 for the unforced case. The ratio of $\bar{u}_{CL}^2/\bar{u}_{max}^2$ is 0.76 for the unforced case and 0.80 for the forced case. One should note that, in general, due to the presence of the artificially introduced coherent motion, the flow is not expected to be as self-preserving as the unforced case. The fact that it is should be attributed to the low level of forcing, which perhaps justifies the application of linear theory.

The mean velocity distributions for each wake are self-preserving, although the

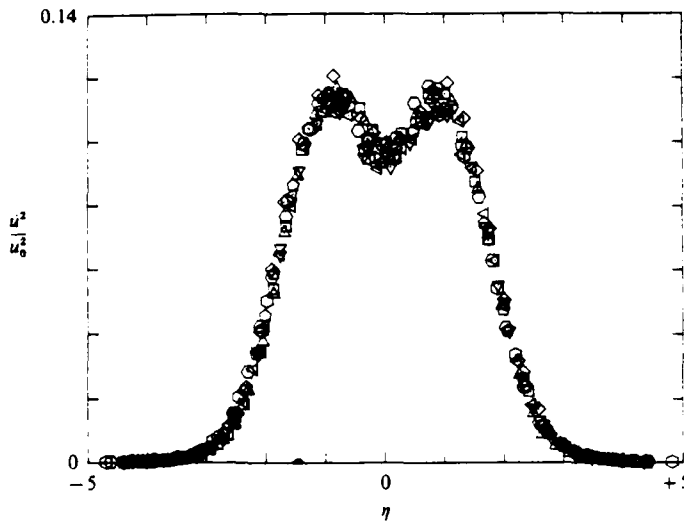


FIGURE 2. The measured distribution of \bar{u}^2/u_0^2 for the varicose forced wake. Different symbols represent different downstream locations in the range $100 < x/\theta < 1400$.

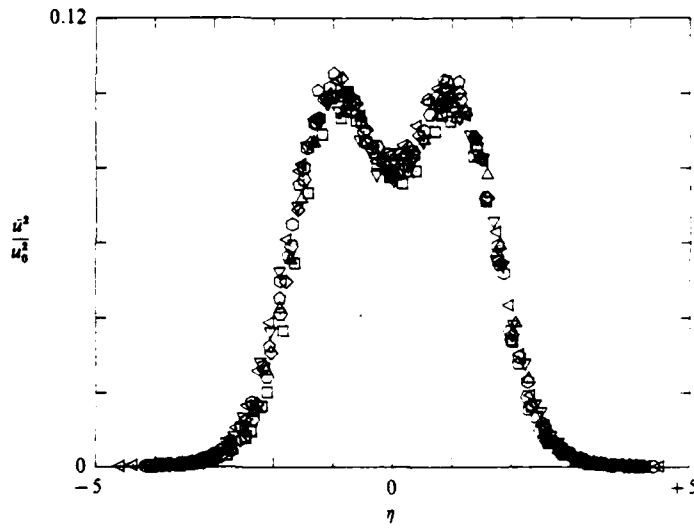


FIGURE 3. The measured distribution of \bar{u}^2/u_0^2 for the unforced wake

wakes developed at slightly different rates in the downstream direction. The streamwise development of the characteristic scales u_0 and L_0 can be expressed as

$$\left[\frac{U_r}{u_0} \right]^2 = \frac{x - x_0}{\theta W_0^2}, \quad (8)$$

$$\left[\frac{L_0}{\theta} \right]^2 = \Delta_0^2 \frac{x - x_0}{\theta}, \quad (9)$$

where W_0 and Δ_0 are constants for a given self-preserving wake. The values of W_0 and Δ_0 for the unforced wake are 1.68 and 0.304, respectively; while those for the varicose

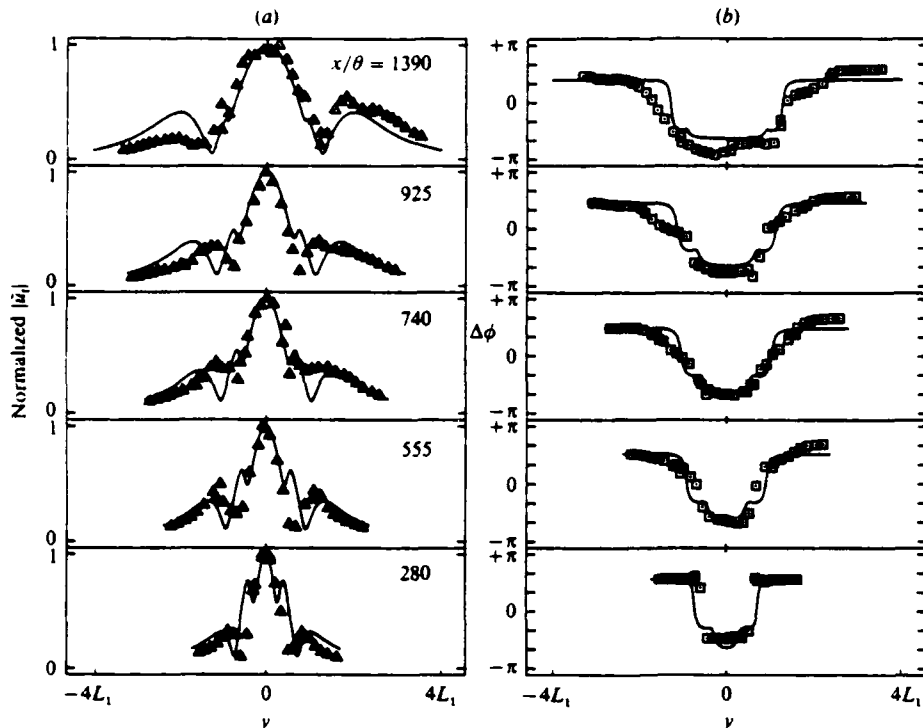


FIGURE 4. (a) The amplitude distributions of the u -component of the disturbance wave for $f = 35$ Hz: Δ , phase-averaged measurements; —, theoretical varicose L_1 is the value of L_0 at $x/\theta = 1390$. (b) The phase distributions of the disturbance wave: \square , phase-averaged measurements; —, theoretical varicose.

forced wake are 1.62 and 0.312. The mean field is therefore affected slightly by the forcing. The virtual origin $x_0 = 0$ and the momentum thickness $\theta = 2.9$ mm for all sets of data presented in this paper. The self-preserving mean velocity profiles are, however, effectively identical for the two wakes. That is, plots of the self-preserving function $f(\eta)$, defined by

$$f(\eta) = \frac{U_x - \bar{U}(x, y)}{u_0(x)} = \exp[-0.637\eta^2 - 0.056\eta^4]. \quad (10)$$

are representative of the profiles for the two wakes.

The distributions of the amplitudes and phases of the velocity perturbations associated with the varicose waves are shown in figure 4(a, b) for five downstream locations. The data, shown by the symbols, were obtained by recording the velocity signal together with the sinusoidal signal activating the flaps. The velocity signals were phase-averaged over 500 cycles of the flap motion, and the Fourier transform applied on the phase-averaged data provided the amplitudes and phase estimates of the spectral elements of the coherent velocity field. The subscript f denotes the component at the fundamental forcing frequency. The abscissa in the figures is dimensional y and the scaling is identical in all figures. The ordinate in figure 4(a) is normalized amplitude and in figure 4(b) is relative phase shift. The results are displayed in this form to indicate the downstream evolution of the wave. The solid lines represent the theoretical results computed from inviscid, linear stability theory

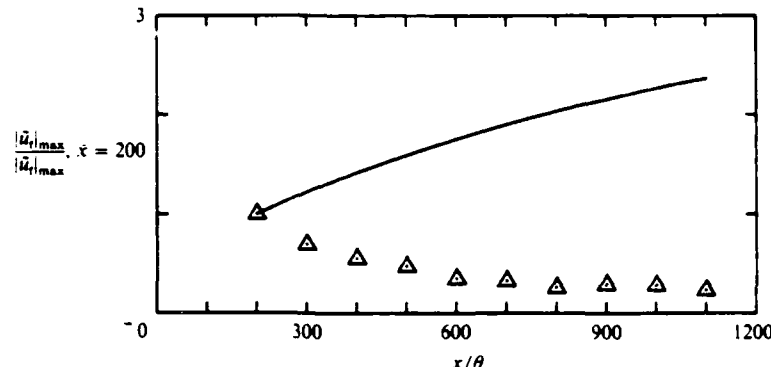


FIGURE 5. The downstream growth of the centreline value of the u -component disturbance amplitude, $f = 35$ Hz: Δ , measurements; —, theoretical linear theory including effects of mean flow divergence.

using the local measured mean velocity profiles. The measured and theoretical amplitude results are normalized by their respective maxima for each downstream location. The disturbance wave remained symmetric for more than 1000 momentum thicknesses before becoming contaminated by asymmetries. There is reasonable agreement between the experimental and theoretical results, even though the wake is fully turbulent. Some of the fine details, such as the minor lobes closest to the centreline shown in the theoretical curves, are not evident in the experimental results. These lobes will subsequently be shown to be related in part to the use of the inviscid approximation.

Another set of measurements was taken at a higher excitation frequency of 50 Hz, $St = 0.0179$, which according to linear theory should evolve sooner. The forcing level at the initial measuring station $x/\theta = 200$ was $(\tilde{u}_{rms}/u_0)_{max} = 11.5\%$. Again, the agreement between the experimental and theoretical amplitude and phase distributions was satisfactory. In this case, the disturbance wave was not detectable beyond $x/\theta > 700$.

The success of inviscid linear theory ends for the varicose mode when the streamwise growth of the disturbance is considered. A comparison between the experimental and theoretical results for the 35 Hz case is shown in figure 5. The theoretical prediction includes the effects of the divergence of the mean flow using the analysis presented by Wygnanski *et al.* (1986). The theoretical results indicate a monotonic growth of the amplitude of \tilde{u}_t on the centreline of the wake, whereas the measurements show a decrease. This discrepancy will be discussed in a subsequent section.

The experiments demonstrated that it is possible to generate a nearly pure symmetric disturbance wave. The difficulty encountered in doing so indicates that the flow is very sensitive to the slightest asymmetries which might be present in the experiments. These asymmetries are preferentially amplified, resulting in the eventual destruction of an initially prominent symmetric wave. It was therefore evident that the total phase-averaged velocity signal should be decomposed into its symmetric and antisymmetric modes in order to study the downstream evolution and interaction.

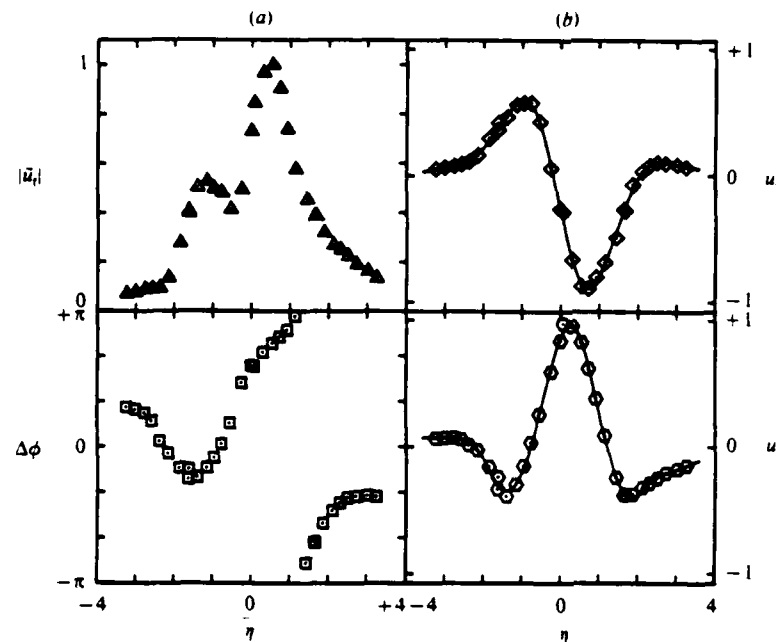


FIGURE 6. (a) The transverse distribution of the amplitude and phase of the forced wave in polar form. (b) As (a) but presented in terms of real and imaginary parts. Symbols represent data, while the solid lines represent the curve fit to data.

5. Decomposition procedure

To decompose the phase-averaged data into modes, we shall take advantage of the fact that the sinuous and varicose modes have \tilde{u} -components that are odd and even functions, respectively, of y . Therefore, if we separate the measured perturbations into odd and even parts, we may have a means of separating the sinuous and varicose modes. The amplitude and phase distributions of the separated parts would then have to be examined and compared to the theoretical distributions of the sinuous and varicose modes.

The decomposition procedure is given as follows. First, we measured the transverse distribution of the phase-averaged u -component, \tilde{u} , using an array of nine hot wires. Typically, 36 points were used to define a distribution. The phase-averaged data for each y -position was Fourier transformed to determine \tilde{u}_r , the component of the velocity perturbation associated with the forced wave at the forcing frequency. The transverse distribution of the amplitude and phase (polar form) of \tilde{u}_r are shown in figure 6(a) for some example data. The triangles and squares represent the data. The same data are shown in figure 6(b) but in terms of their real and imaginary parts, where the subscripts r and i represent real and imaginary, respectively. To obtain the odd and even parts of these distributions, the centreline location was estimated using the measured mean velocity profile. Then, as we generally did not have data at exactly equidistant positions about the centreline, we fitted a curve to the measured data. Fourier series in y (or η) were used as a curve fit to the real and imaginary parts separately. The fitted curves are shown for the example data by the solid lines in figure 6(b). The curve fit to each was separated into its odd and even parts, indicated in figure 7(a, b) by the dashed lines and solid lines, respectively. The

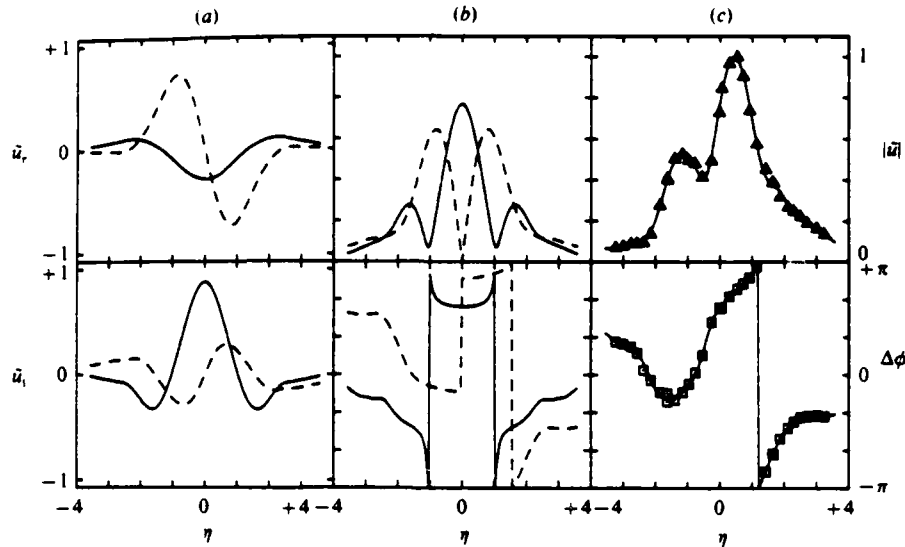


FIGURE 7. (a) The odd and even parts of the curve fit: ---, odd part, —, even part. (b) As in (a) but expressed in polar form. (c) —, superposition of odd and even parts; symbols represent original data.

respective odd and even parts are expressed in polar form in figure 7(b), while their superposition, which restores the original data, is shown in figure 7(c) by the solid lines. The symbols in figure 7(c) represent the original data, which agree well with the estimated distributions obtained from the curve fits to the real and imaginary parts. This agreement demonstrates that the curve fitting was done satisfactorily without introducing any bias. Note, for the example data, that the amplitude distribution has a large even component, although it is asymmetric. One should also recognize the resemblance of the decomposed parts, shown in figure 7(b), to the sinuous and varicose modes computed from linear stability theory.

6. Combined modal forcing of the wake

By applying a small phase difference to the relative motion of the two flaps, a sinuous component was also introduced. This provides a means of simultaneously forcing the wake with both modes to study their possible interaction. The results of combined forcing at a frequency of 28 Hz ($St = 0.0109$) in terms of the lateral distribution of \bar{u}^2/u_0^2 are shown in figure 8. The forcing level $(\bar{u}_{rms}/u_0)_{max}$ was 12.0% at $x/\theta = 200$. The flow appears to be self-preserving, but the \bar{u}^2 distribution is asymmetric. The mean velocity profile retains its symmetry, and the mean spreading rate is given by the values of W_0 and A_0 equal to 1.61 and 0.312, respectively. Again, the amplitude of the coherent fluctuations is small, and the wake maintains a nearly self-preserving form.

The measured amplitude and phase distributions of \bar{u}_t for five downstream locations are shown in figure 9. The ordinate for each is the normalized amplitude of \bar{u}_t . The abscissa is y and has the same scale for each plot. The wake growth with x is evident. The amount of asymmetry changes initially with x but appears to remain nearly constant in the far wake ($x/\theta > 750$). The solid lines in figure 9 will be discussed at the end of §7. These distributions were decomposed into their odd and

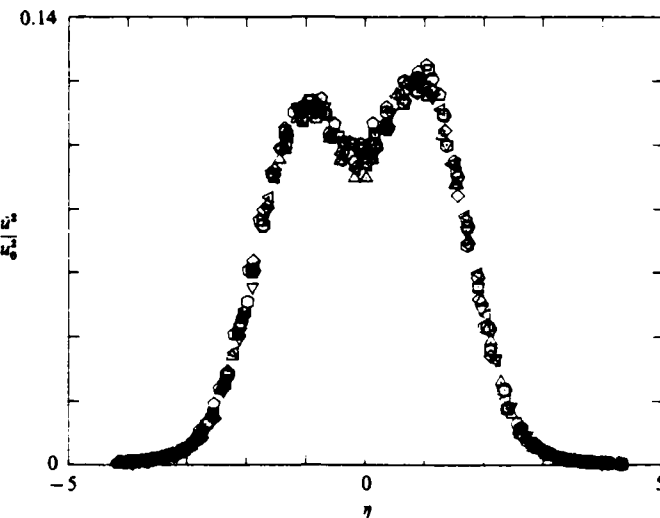


FIGURE 8. The measured distributions of \bar{u}^2/u_0^2 for the forced wave. Combined mode forcing, $f = 28$ Hz.

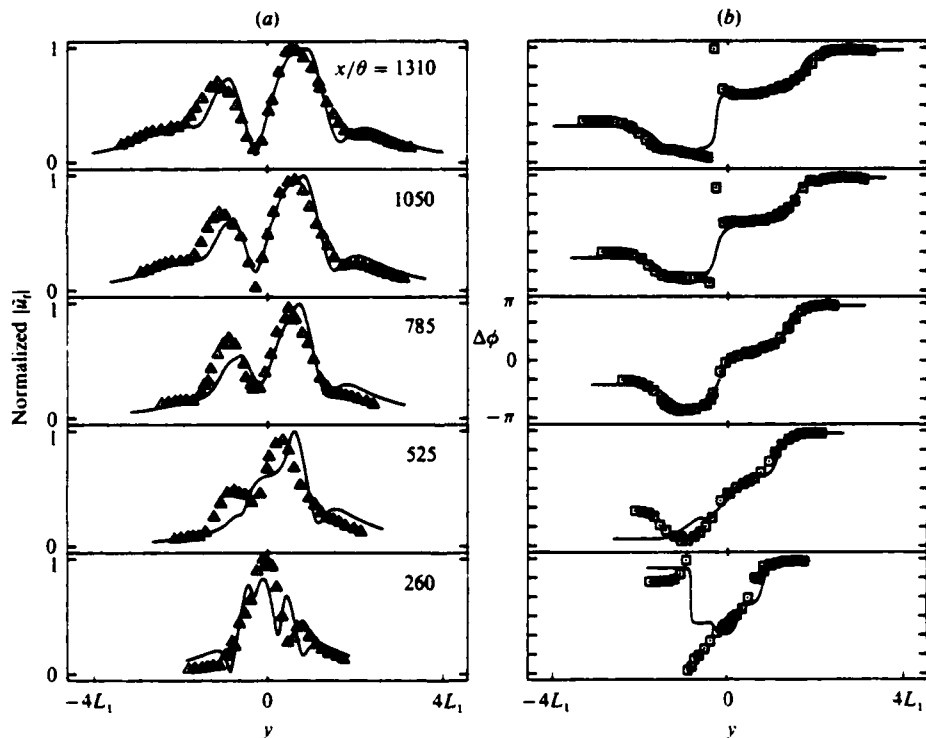


FIGURE 9. (a) The amplitude distributions of the u -component of the disturbance wave: Δ , the measured phase-averaged results; —, linear superposition of modes using equation (11). L_1 is the value of L_0 at $x/\theta = 1310$. (b) The phase distributions of the u -component of the disturbance wave: \square , measured; —, superposition of theoretical modes.

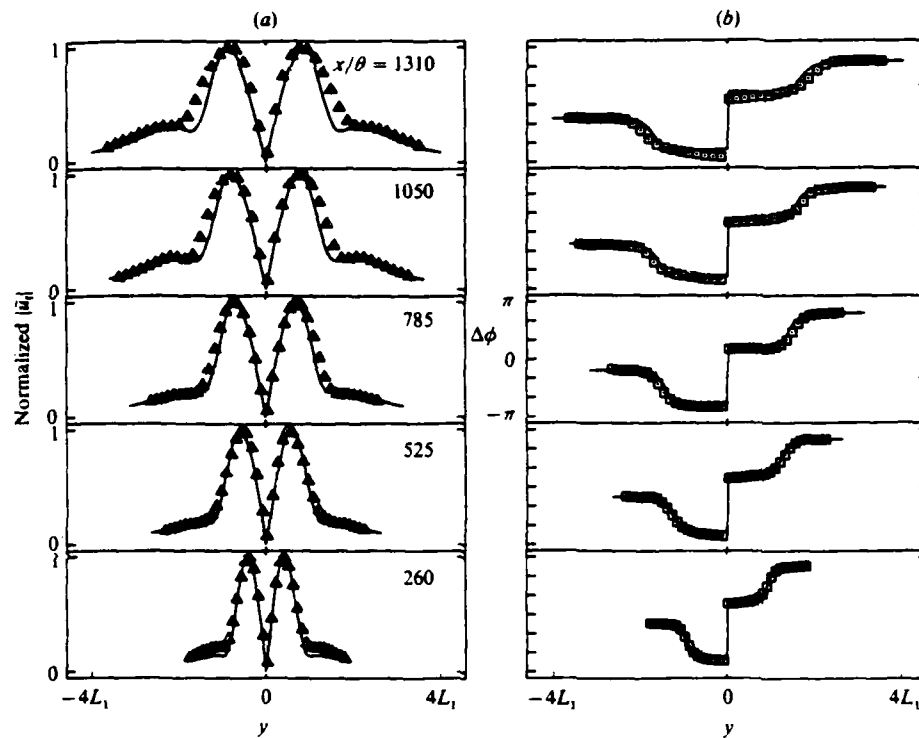


FIGURE 10. (a) The amplitude distributions of the antisymmetric component: Δ , measured: —, theoretical sinuous. L_1 is the value of L_0 at $x/\theta = 1310$. (b) The phase distributions of the antisymmetric component: \square , measured: —, theoretical sinuous.

even parts. The resulting odd part for each downstream location is plotted in figure 10(a), designated by triangles. The ordinate is the normalized amplitude and the abscissa is y , again. The solid lines represent the normalized amplitude of the theoretical sinuous mode computed from linear, inviscid stability theory using the measured mean velocity profiles. The comparison between the theoretical and measured phase distributions is shown in figure 10(b). The agreement between the measured odd parts and the theoretical sinuous mode is excellent. Thus, the measured odd part undoubtedly corresponds to the sinuous mode obtained from the stability theory.

The amplitude and phase distributions for the even parts at each downstream location are shown in figure 11(a, b). The solid lines represent the theoretical varicose distributions. The agreement is quite satisfactory, though it is not as good as for the sinuous model, but the even part appears to correspond to the varicose mode of linear stability theory.

The relative intensity of the two modes was obtained by integrating the amplitude distributions across the flow for each mode and taking the ratio of the two. The downstream evolution of the ratio is shown in figure 12. Initially, the amplitude of the varicose mode is about twice that of the sinuous mode but, in accordance with linear theory (parallel flow), the sinuous mode eventually dominates and an equilibrium ratio of $A_v/A_s = 0.5$ is reached for $x/\theta > 800$, at least for this particular experiment. It is surprising that a non-vanishing constant ratio is achieved, but the generality of this intriguing result is yet to be established.

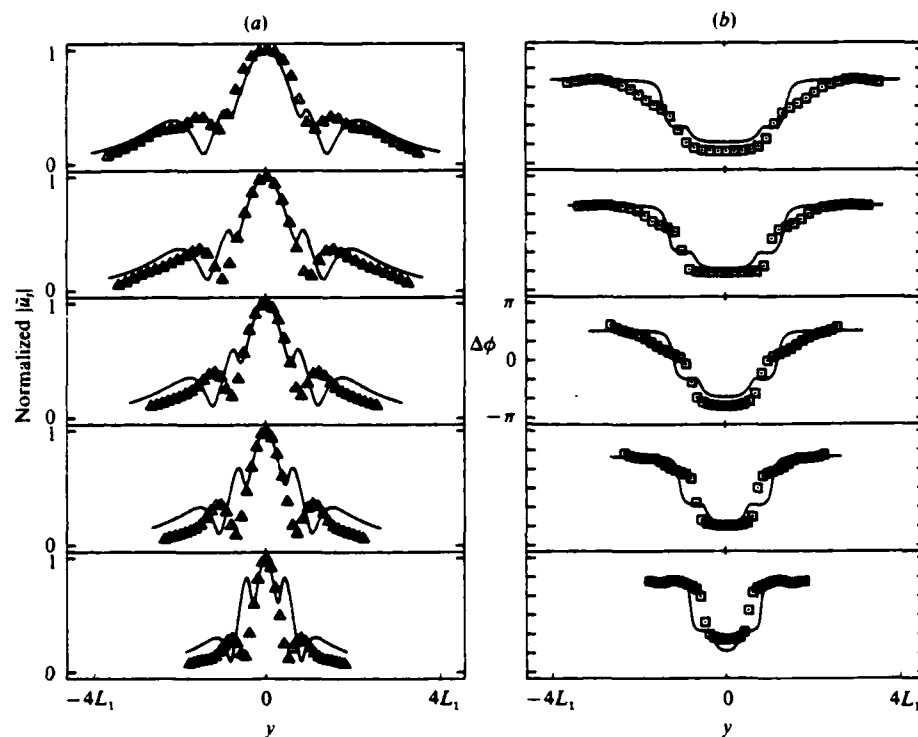


FIGURE 11. (a) The amplitude distributions of the symmetric component: Δ , measured; —, theoretical varicose. L_1 is the value of L_0 at $x/\theta = 1310$. (b) The phase distributions of the symmetric component: \square , measured; —, theoretical varicose.

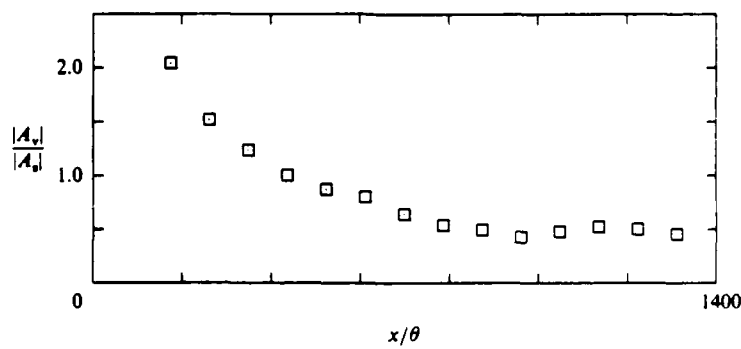


FIGURE 12. The relative ratio of the two modes.

The spatial growth of the maximum of the sinuous and varicose components of the disturbance wave is shown in figure 13. The slowly diverging analysis presented in Wygnanski *et al.* (1986) was used to obtain the theoretical prediction for each mode represented by the solid lines. The growth of the sinuous mode is predicted quite well by linear theory, as it was in the case presented by Wygnanski *et al.* (1986). The growth of the varicose mode is not well predicted, however, which was also the case for the purely varicose forcing presented previously. An interesting point to note regarding the spatial amplification of the two modes is that, for the same mean flow

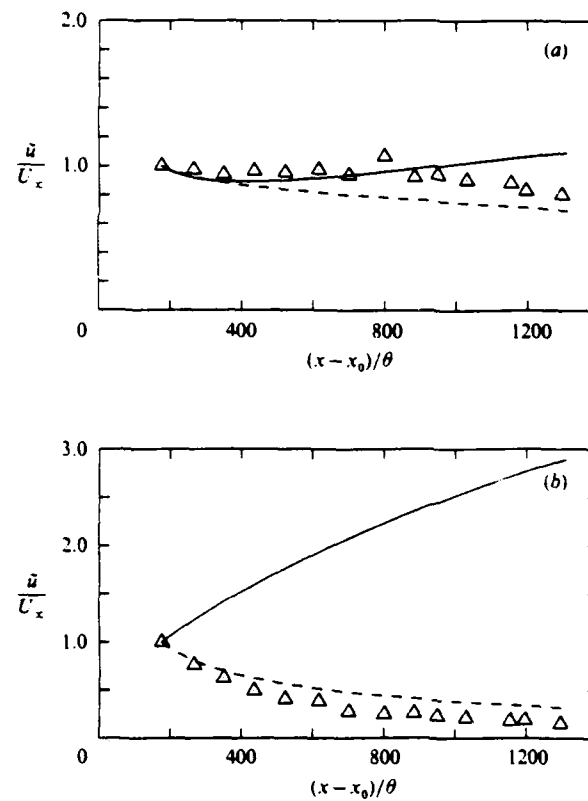


FIGURE 13. The spatial variation of the maximum value of \tilde{u}_t for $f = 28$ Hz for (a) the sinuous mode and (b) the varicose mode: Δ , measured; —, inviscid; ---, $Re_\eta = 30$.

and frequency, the varicose mode is predicted to amplify more than the sinuous mode, although the growth rates from parallel theory are much larger for the latter. This point is confirmed by T. F. Balsa (private communication), who performed the calculations independently, utilizing a different computational scheme. Apparently, the divergence effects which inhibit the rate of amplification of a particular mode are much more severe on the propagation of the sinuous mode than the varicose mode. The experimental results, however, do not seem to support this theoretical observation and some conjectures will be presented regarding this discrepancy and its possible implications for the evolution of laminar near wakes. The dashed lines will be discussed subsequently.

7. Superposition of modes

The agreement between the amplitudes and phases of the odd and even parts of the phase-averaged data and the theoretical sinuous and varicose modes (figures 10 and 11) suggests that a proper superposition of the theoretical modes should agree well with the experimental phase-averaged results.

The proposed superposition is as follows:

$$\phi'_{\text{TOT}}(y) = c_s \phi'_s(y) + c_v \phi'_v(y). \quad (11)$$

where ϕ'_{TOT} = measured disturbance (\bar{u}_t), ϕ'_s = theoretical sinuous eigenfunction, ϕ'_v = theoretical varicose eigenfunction; and c_s and c_v are complex constants given by

$$c_s = \frac{\int_{-x}^x \phi'_{TOT} \phi'_s dy}{\int_{-x}^x \phi'_s \phi'_s dy} \quad (12)$$

and

$$c_v = \frac{\int_{-x}^x \phi'_{TOT} \phi'_v dy}{\int_{-x}^x \phi'_v \phi'_v dy} \quad (13)$$

The composite theoretical curves, indicated by the solid lines, are compared with the experimental data in figure 9 and, as expected, the agreement between the two is quite good.

8. Effects of viscosity

The Reynolds number based on the free-stream velocity, the half-width of the wake, and the molecular viscosity is about 10^4 for most of the data presented here and, therefore, viscous effects are not expected to be of importance. However, if one considers the appropriate velocity scale to be the velocity deficit of the wake, which is typically 5% of the free-stream velocity, the ensuing Reynolds numbers are of the order of 500. This motivated a brief study of the stability of the viscous wake. For this purpose, the full Orr-Sommerfeld equation (4) has to be considered together with the appropriate boundary conditions (presented in §3). The Orr-Sommerfeld equation was solved numerically using the Gram-Schmidt orthonormalization technique with double precision complex arithmetic, which provided valid solutions for rather high Reynolds numbers.

The calculations were done using the mean-flow parameters corresponding to the combined modal forcing experiment. Figure 14(a) shows the amplification rates versus the non-dimensional frequency β of the sinuous mode for a constant value of the velocity deficit $u_0/U_\infty = 12.3\%$, which corresponds to the initial streamwise location of the experiment. Three cases are presented. The solid curve represents the inviscid solution. The dashed line corresponds to the viscous solution for $Re_\theta = U_\infty \theta/\nu = 1400$, and at this Reynolds number the difference between the inviscid and viscous amplification rates is hardly visible. The Reynolds number based on θ is the appropriate choice for the experiments, as θ is the proper lengthscale characterizing the wake generator. Recall that θ is a constant for the zero-pressure-gradient wake. For this velocity deficit, the experimental excitation frequency 28 Hz corresponds to $\beta = 0.282$, and it is amplified. The third curve, which is indicated by the dotted-dashed lines, represents calculations done at a much lower Reynolds number, namely at $Re_\theta = 30$, and the growth rates are more visibly lower than their inviscid counterparts. The reason for the choice of this quite low Re will be evident in the next section. Figure 14(b) shows the calculated growth rates using the parameters corresponding to the final x -station of our measurements ($u_0/U_\infty = 4.5\%$). The nomenclature is the same as in figure 14(a). At this location, $f = 28$ Hz corresponds to $\beta = 0.772$, which is comfortably in the amplified region of all the cases presented. The streamwise variation of the growth rate, $-\alpha_1$, for the sinuous mode is presented

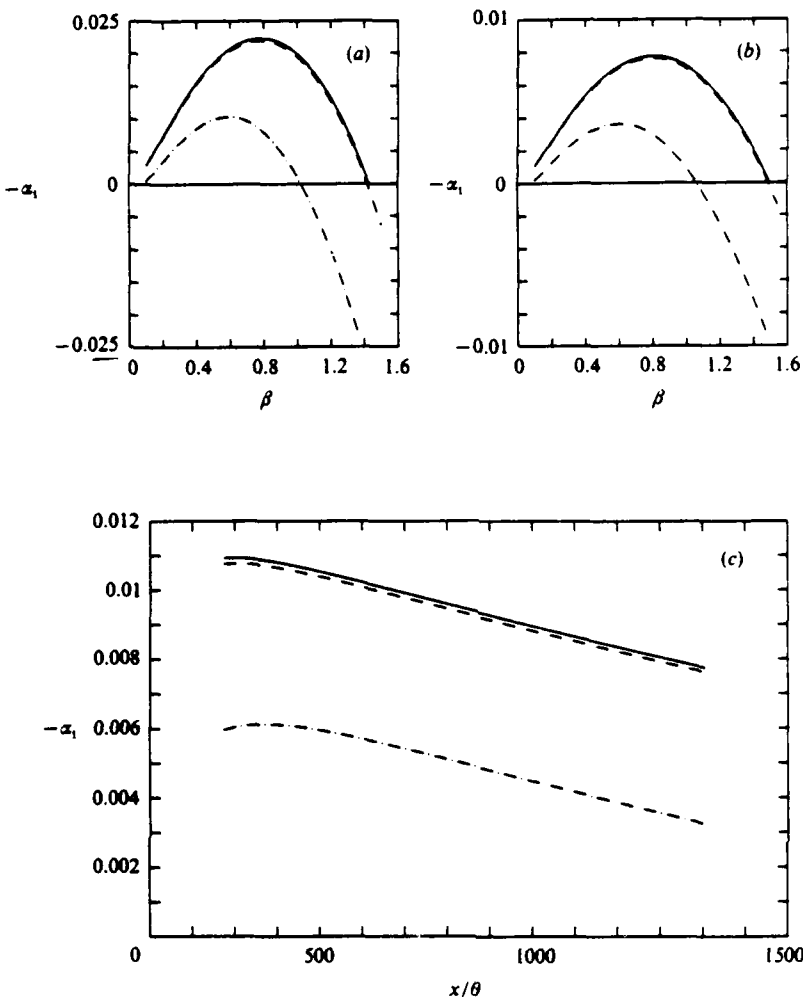


FIGURE 14. Amplification rates for the sinuous mode: (a) versus β , $u_0/U_z = 0.123$; (b) versus β , $u_0/U_z = 0.045$; (c) versus x/θ : —, inviscid; - - -, $Re_n = 1400$; - · - -, $Re_n = 30$. Recall that x_1 is non-dimensionalized by L_0 .

in figure 14(c). For the present case, the amplification rates decay almost linearly with x . It is certainly evident that the viscous effects are negligible for this case. The wavenumber α_1 and the phase speed are not shown as they are not significantly affected by viscosity.

The varicose mode is observed to be affected more by viscosity. Figure 15(a, b, c) depicts similar calculations for the varicose mode using the experimental mean-flow parameters. The nomenclature is the same as in figure 14(a, b, c). The growth rates at $Re_n = 1400$ are approximately 10% less than their inviscid counterparts. However, this difference cannot explain the discrepancy between the experimental results and the inviscid predictions shown in figure 13(b). But, a dramatic difference is seen for the $Re_n = 30$ calculations – the disturbances are damped at this low Reynolds number. Again, the phase speed and α_1 are essentially unaffected.

There is no significant change in the shape of the eigenfunction for the sinuous

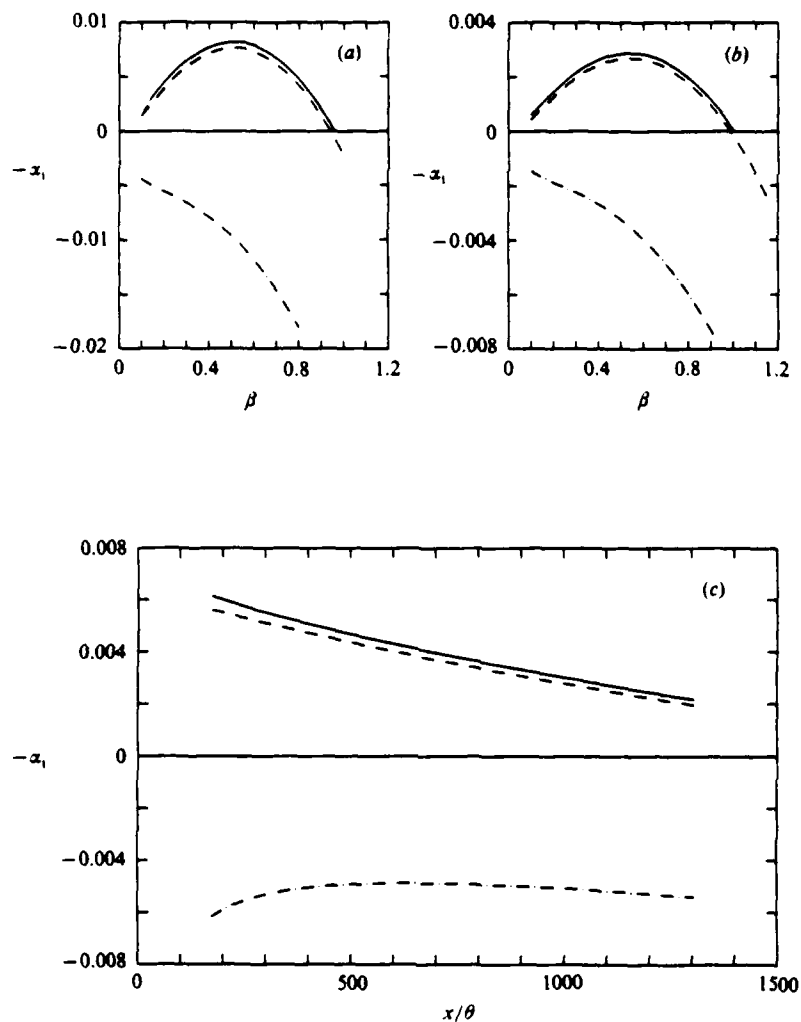


FIGURE 15. Amplification rates for the varicose mode. (a) versus β , $u_0/U_x = 0.123$; (b) versus β , $u_0/U_x = 0.045$; (c) versus x/θ ; —, inviscid; - - -, $Re_\eta = 1400$; - - - , $Re_\eta = 30$.

mode when viscous effects are included, as can be seen from figure 16(a). The u -amplitude distribution of the velocity perturbation for the inviscid case is compared with the viscous solutions for $Re_\eta = 1400$ and 30. The distributions are normalized using their respective maxima. The parameters corresponding to $x/\theta = 400$ of our measurements were used in the computations of the presented cases ($u_0/U_x = 8.1\%$, $\beta = 0.428$). The shape of the predicted varicose eigenfunction is more significantly affected, as viscosity tends to eliminate the kinks occurring in the u -amplitude distribution, as shown in figure 16(b). The velocity gradients in the varicose mode are much larger than those occurring in the sinuous mode, thus making the higher-derivative terms in (4) of considerable importance, and the viscosity works towards smoothing those large gradients.

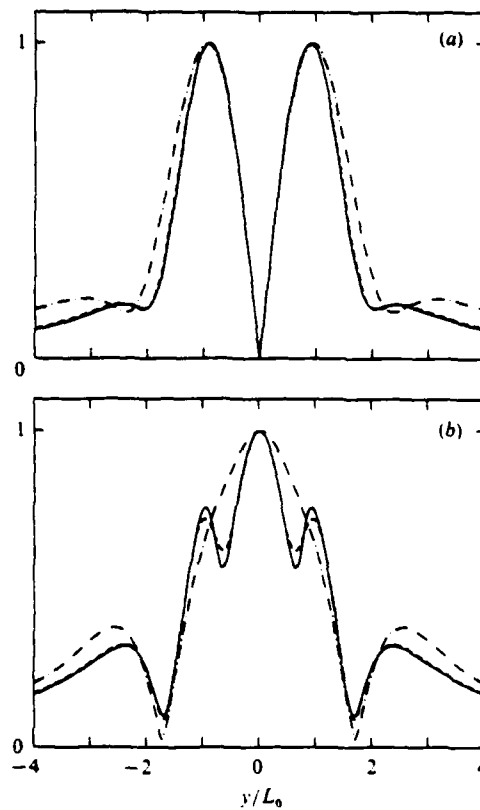


FIGURE 16. The u -amplitude distributions for (a) the sinuous mode and (b) the varicose mode where $u_0/U_\infty = 0.081$ and $\beta = 0.428$: —, inviscid; - - -, $Re_\eta = 1400$; - · - , $Re_\eta = 30$.

9. Effects of turbulence

The effects of the turbulent fluctuations on the spatial propagation of the perturbation waves are completely ignored in the present model. As already mentioned, all theoretical results are computed from linear stability theory using the measured local mean velocity profiles. The base flow is fully turbulent rather than laminar. The viscous effects, as discussed in the previous section, are estimated using the same mean velocity profiles along with the molecular viscosity. We realize that the wave propagation characteristics will be affected by the turbulence, but we also are unaware of any generally accepted method for accounting for such effects. If one considers the dynamical equation for \tilde{u} in the presence of turbulence, as presented by Reynolds & Hussain (1972; equation 2.6), new unknown terms appear, such as the time and phase average of $u'v'$. The simplest way to account for the effects of turbulence is to use an eddy viscosity along with the turbulent base flow as done by Tam & Chen (1979), Liu (1971), Potter (1971), and others. If we adopt a similar model here and replace the molecular kinematic viscosity with an eddy viscosity in (4), this approach leads to a possible explanation regarding the difference in behaviour of the sinuous and varicose modes shown in figure 13(a, b). The magnitude of the eddy viscosity was estimated from our recent Reynolds-stress measurements in the unforced wake of the flat plate. These results indicate that the eddy viscosity is, on

the average, 40 times larger than the kinematic viscosity of the fluid, so the effective Reynolds number for the present data becomes $(Re_n)_{\text{eff}} = 30$. Therefore, if one wants to lump the nonlinear effects stemming from the generation of Reynolds stresses (whether coherent or random) into a model represented by an eddy viscosity, then one should use an effective Re_n which is based on ν_T . It is apparent from figure 14(c) that, at this lower Reynolds number, the sinuous mode is still amplified, although at a smaller rate. On the other hand, figure 15(c) shows that the varicose mode is damped over the entire experimental domain in accordance with the experimental results shown in figure 13(b). The eddy-viscosity model brings improvement to the prediction of the streamwise variation, especially for the varicose mode. Figure 13(a, b) shows the spatial development of the maximum of the two modes. The dashed lines correspond to the calculation using the eddy-viscosity model with $Re_n = 30$. The transverse distributions of the \bar{u} -amplitudes are also well explained, as shown in figure 16(a, b). The dotted-dashed lines represent the eddy-viscosity calculations using $Re_n = 30$. A comparison with the measured distributions shows that, although the general features of the amplitude distributions are predicted quite well, the computed distributions are wider than their measured counterparts. This is undoubtedly caused by the significantly higher values of viscosity used in the $Re_n = 30$ case. Also, although not shown here, the phase distribution for the varicose case is not well predicted (see Marasli 1988). Summarizing these results, linear stability theory predicts the local shapes of the eigenfunction distributions for both modes fairly well, while slowly diverging linear theory does a reasonable job for the streamwise variation of the sinuous mode. On the other hand, the eddy-viscosity model predicts the streamwise variation of both modes reasonably well and describes the transverse distributions of the perturbation amplitudes for both modes, but it fails to predict the distribution of phase for the varicose mode.

The difficulty encountered in generating a varicose disturbance that survived in the far wake is more understandable through this model. Recall, however, that the slowly diverging analysis predicts larger overall amplification for the varicose mode than the sinuous mode in a laminar base flow. For particular wake-generator configurations, the near wakes in a laminar flow could be dominated by varicose instabilities (see, for example, Williamson 1985; Rockwell *et al.* 1985; and Papailiou & Lykoudis 1974). This does not mean that the varicose mode is the dominant instability for the near wakes. For the varicose mode to have a chance, the Reynolds number must be high enough to avoid the viscous effects; on the other hand, the flow must also be free of incoherent fluctuations to maintain a laminar base flow.

The eddy-viscosity model appears to be adequate for understanding some of the features of travelling waves in a fully turbulent base flow; however, its shortcomings have to be kept in perspective. In addition to its problems of describing turbulent flows in general, the fact that turbulence reorganizes itself by interacting with the coherent motion (Hussain 1983; Marasli 1988) is an additional complexity which cannot be described by this model. Nevertheless, a conceptual simplification of the effects of incoherent turbulent fluctuations is provided by this model.

10. Conclusions

It is possible to generate a nearly pure varicose mode of instability in the wake. The sensitivity of the flow to asymmetric disturbances, however, makes it a difficult experimental task. Even the slightest asymmetric disturbance can be preferentially amplified, as the growth rates of sinuous disturbances are much larger than those for

varicose disturbances. Therefore, contamination of the varicose mode by the sinuous mode is difficult to avoid, especially over large downstream distances.

A decomposition technique was developed to separate a phase-averaged distribution into its symmetric and antisymmetric components. The measurements show that these components agree well with their corresponding theoretical counterparts, that is, the varicose and sinuous modes from linear stability theory. The relative strength of the two modes at any downstream location can then be determined by integrating the amplitude distribution across the flow for each mode and taking the ratio of the two. The modal decomposition technique was applied to a case of combined excitation. The relative-strength-ratio measurements show that, initially, the varicose mode was twice as strong as the sinuous mode, but the sinuous mode eventually became dominant because of the larger amplification rates. An equilibrium ratio was approached in the far wake for $x/\theta > 1000$.

Viscosity affects the varicose mode more than it does the sinuous mode. As expected, the amplification rates were found to decrease with decreasing Reynolds number and velocity deficit, but the phase speed of the disturbance remains unaffected. An attempt to account for the effects of turbulence on the spatial propagation of a perturbation wave was made using an eddy-viscosity model. Based on this model, a possible explanation was obtained for the observed discrepancy between the experimental results and the slowly diverging wake prediction for the varicose mode.

This project was supported by the Air Force Office of Scientific Research under contract no. 85-00148. We wish to thank Dr James M. McMichael for his efforts in monitoring the project. We also would like to thank Dr T. F. Balsa for his cooperation in determining the validity of some of our stability calculations.

REFERENCES

BELLMAN, R. E. & KALABA, R. E. 1965 *Quasilinearization and Nonlinear Boundary Value Problems*. Elsevier.

BETCHOV, R. & SZEWZYK, A. 1963 *Phys. Fluids* **6**, 1391.

HUSSAIN, A. K. M. F. 1983 *Phys. Fluids* **26**, 2816.

LIU, J. T. C. 1971 *Phys. Fluids* **14**, 2251.

MARASLI, B. 1988 Spatially traveling disturbances in a plane, turbulent wake. Ph.D. thesis, University of Arizona.

PAPAILOU, D. D. & LYKOURIS, P. S. 1974 *J. Fluid Mech.* **62**, 11.

POTTER, M. C. 1971 *Phys. Fluids* **14**, 1323.

REYNOLDS, W. C. & HUSSAIN, A. K. M. F. 1972 *J. Fluid Mech.* **54**, 263.

ROCKWELL, D., ONGOREN, A. & UNAL, M. 1985 AIAA paper 85-0529, presented at *AIAA Shear Flow Control Conference*, Boulder.

TAM, C. K. W. & CHEN, K. C. 1979 *J. Fluid Mech.* **92**, 303.

WAZZAN, A. R., OKAMURA, T. T. & SMITH, A. M. O. 1968 Spatial and temporal stability charts for the Falkner-Skan boundary-layer profiles. Rep. DAC-67086. Douglas Aircraft Company, Long Beach.

WILLIAMSON, C. H. K. 1985 *J. Fluid Mech.* **159**, 1.

WYGNANSKI, I., CHAMPAGNE, F. H. & MARASLI, B. 1986 *J. Fluid Mech.* **168**, 31.

On the large-scale structures in two-dimensional, small-deficit, turbulent wakes

By I. WYGNANSKI, F. CHAMPAGNE AND B. MARASLI

Aerospace and Mechanical Engineering Department, University of Arizona,
Tucson, AZ 85721, USA.

(Received 9 December 1983 and in revised form 1 November 1985)

A systematic study of two-dimensional, turbulent, small-deficit wakes was carried out to determine their structure and the universality of their self-preserving states. Various wake generators, including circular cylinders, a symmetrical airfoil, a flat plate, and an assortment of screens of varying solidity, were studied for a wide range of downstream distances. Most of the generators were tailored so that their drag coefficients, and therefore their momentum thicknesses, were identical, permitting comparison at identical Reynolds numbers and aspect ratios. The flat plate and airfoil had a small, trailing-edge flap which could be externally driven to introduce forced sinuous oscillations into the wake. The results indicate that the normalized characteristic velocity and length scales depend on the initial conditions, while the shape of the normalized mean velocity profile is independent of these conditions or the nature of the generator. The normalized distributions of the longitudinal turbulence intensity, however, are dependent on the initial conditions.

Linear inviscid stability theory, in which the divergence of the mean flow is taken into account, predicts quite well the amplification and the transverse distributions of amplitudes and phases of externally imposed sinuous waves on a fully developed turbulent wake generated by a flat plate. There is a strong indication that the large structures observed in the unforced wake are related to the two-dimensional instability modes and therefore can be modelled by linear stability theory. Furthermore, the interaction of the two possible modes of instability may be responsible for the vortex street-type pattern observed visually in the small-deficit, turbulent wake.

1. Introduction

Turbulent, plane wakes generated by circular cylinders in the absence of a pressure gradient have been the subject of numerous experimental investigations, the most notable of which are those by Townsend (1947, 1949). The results of these studies, along with results obtained in other free shear flows, led to the early ideas of self-preservation and Reynolds number independence proposed by Townsend (1956). It was postulated that, sufficiently far downstream from the cylinder, an asymptotic self-preserving state is achieved for which the flow can be described by a single velocity scale u_0 and a single lengthscale L_0 (see figure 1). That is, the transverse distributions of mean velocity and Reynolds stress must be independent of the streamwise coordinate x when normalized by these scales. One question under investigation presently is to determine whether and where these scales can be considered unique.

It has been well established (Townsend 1956; Uberoi & Freymuth 1969; Symes &

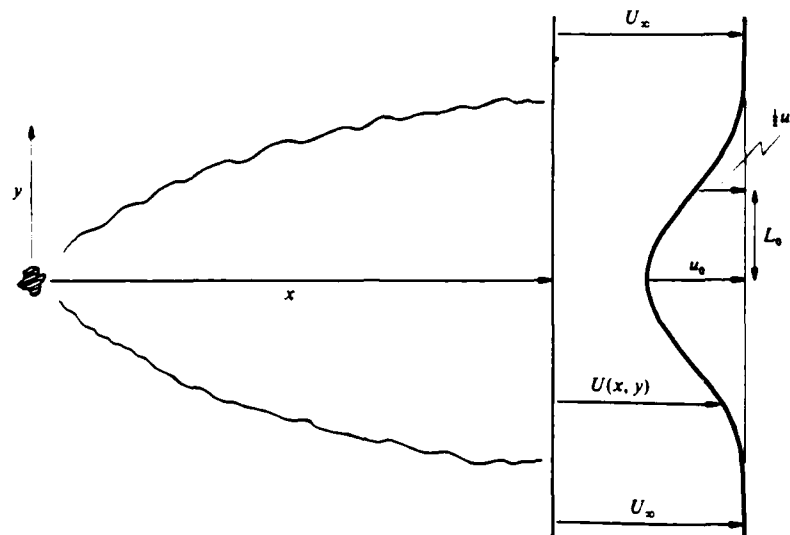


FIGURE 1. A sketch defining the nomenclature.

Fink 1977; Yamada *et al.* 1980) that far-downstream flows are self-preserving and that the velocity and length scales, u_0 and L_0 , vary as $(x - x_0)^{-1}$ and $(x - x_0)^{1/2}$, respectively, as predicted by the equations of motion and the momentum integral constraint. The virtual origin, x_0 , is used to account for viscous or Reynolds-number effects. Furthermore, Townsend (1956) indicated that at sufficiently high Reynolds number, L_0/d and u_0/U_∞ are universal functions of x/d only, where d is the diameter of the cylinder. The initial motivation for the present study stemmed from comparing some early measurements describing the downstream variation of the streamwise component of turbulence intensity. We observed large differences between our data and data reported in the literature that could not be attributed to experimental technique (figure 2). Large differences between the various results are evident, and the trends in the data are quite different at large $x/C_D d$, where C_D is the drag coefficient. At the time (*circa* 1970), most investigators used the cylinder diameter for the purpose of normalization. Considerations based on the equations of motion show that the momentum thickness, θ , should have been used as the normalizing lengthscale for the small-deficit wake. That is, the drag force exerted on the fluid by the cylinder should be used to define the initial flow conditions. We will use 2θ because $C_D d = 2\theta$. It can be shown that the normalized velocity and length scales should vary as

$$\left(\frac{U_\infty}{u_0}\right)^2 \sim \left(\frac{x - x_0}{2\theta}\right), \quad \left(\frac{L_0}{\theta}\right)^2 \sim \left(\frac{x - x_0}{2\theta}\right). \quad (1.1)$$

The data of Townsend (1956), Symes & Fink (1977), and Yamada *et al.* (1980) confirm the above relations and show that mean velocity profiles observed by each investigator are self-similar when scaled by their individual velocity and length scales. However, comparison of the data indicates a possible lack of universality in the behaviour of these scales; that is, different wakes developed differently with downstream distance.

Sreenivasan (1981) examined the manner in which wakes produced by a variety of generators approached self-preserving states. He observed substantial differences

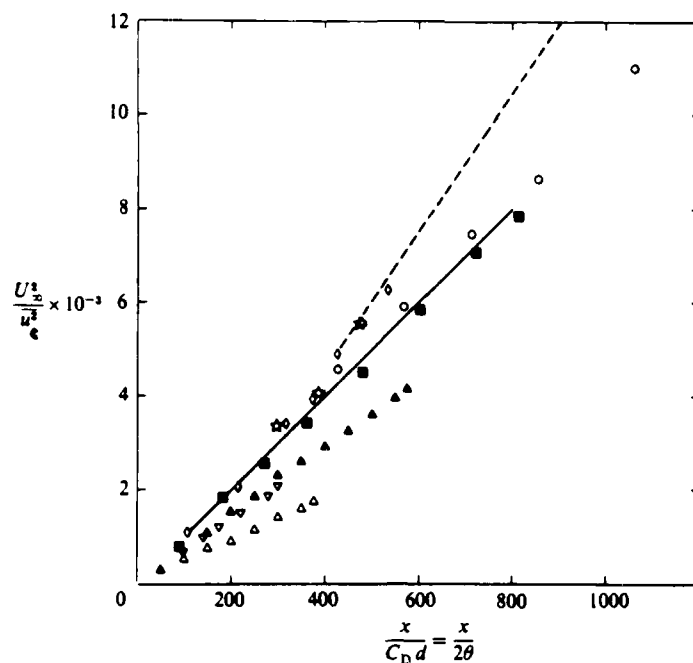


FIGURE 2. Centreline turbulence intensity for wakes generated by circular cylinders. \circ , Marasli (1983), $Re = 1360$, $AR = 384$; \blacksquare , Marasli, $Re = 5900$, $AR = 128$; \diamond , Townsend (1956), $Re = 1360$, $AR = 240$; \cdots , Townsend (1949); $-$, Uberoi & Freymuth (1969), $Re = 4320$, $AR = 192$; \star , Yamada *et al.* (1980), $Re = 4000$, $AR = 80$; ∇ , Champagne (1978), $Re = 19000$, $AR = 32$; \blacktriangle , Symes & Fink (1977), $Re = 6666$, $AR = 150$, no ext. turb. added; \triangle , Symes & Fink, with ext. turb. added.

in the way these flows evolved, even though each flow preserved the shape of the mean velocity profile when normalized by its own characteristic scales. Sreenivasan & Narasimha (1982) suggested that a unique self-preserving state exists for all plane wakes and defined the characteristic constants stemming from their suggestion. We felt at the time that their data did not fully support their conclusion, and the present study compiles further evidence negating it.

A possible explanation for the lack of uniqueness is suggested by the results of Symes & Fink (1977), who investigated the effect of free-stream turbulence on the development of wakes. They showed that the relative scale of the external turbulence, rather than the level of the turbulence intensity, was an important parameter affecting the development of the wake. As each experimental facility has its own characteristic free-stream disturbances, wakes generated in a particular facility may be unique to that facility only. The lack of universality of various small-deficit wake flows might be explained in terms of the instability of the mean velocity profile in the wake. Related to this are the flow visualization results of Cimbala, Nagib & Roshko (1981), which revealed that large coherent structures develop far downstream from the wake generator and these are not necessarily related to the vortices shed from the generator. This was sufficient evidence to suggest that the wake, like the mixing layer, contains large-scale coherent structures which may have a wave-like behaviour. Travelling, large structures were observed in both laminar (Freymuth 1966) and turbulent (Brown & Roshko 1974; Oster & Wygnanski 1982) mixing layers, and their behaviour was explained by an instability mechanism (Michalke 1965;

Gaster, Kit & Wygnanski 1985). The similarity of the patterns occurring in both laminar and turbulent states is not surprising in view of the fact that the instability mechanism is principally inviscid and is controlled by the mean velocity profiles, which are similar in both situations. Gaster *et al.* computed the amplitude distributions and the phase speeds of travelling waves associated with large coherent structures in the plane turbulent mixing layer, and they obtained very good agreement with experimental results by accounting for the effects of mean flow divergence. The mean velocity profile in the wake is also inviscidly unstable, and its shape is not affected by transition from laminar to turbulent flow, suggesting that a similar analysis could predict the evolution of the large-scale structures in this flow as well.

The stability and transition of a plane wake, generated by a thin plate placed parallel to a uniform flow, was considered by many investigators (e.g. Sato & Kuriki 1961; Mattingly & Criminale 1972; Zabuski & Deem 1971). The analysis in these investigations was always concerned with the immediate neighbourhood of the trailing edge, where the velocity deficit was greater than 60% of the free-stream velocity. Sato & Kuriki (1961) limited their analysis to a temporal evolution of the instability at one location in the flow, and Mattingly & Criminale (1972) considered the instability of the wake to natural disturbances in both time and space and concluded that the spatial evolution of a travelling wave gives superior predictions for the disturbance characteristics experimentally observed. The analysis invariably assumed that the flow was parallel and was therefore limited to a prescribed streamwise location in which the width of the wake was defined. The parallel flow assumption represents a severe constraint on predicting growing disturbances in the wake because, in addition to the local width of the flow, the characteristic velocity scale must also change as a result of the divergence.

In contradistinction to the mixing layer, the plane wake is susceptible to both symmetrical (varicose) and antisymmetrical (sinuous) modes of instability. The varicose mode was traditionally disregarded (e.g. Sato & Kuriki 1961) because calculations based on the parallel flow approximations indicated that the most strongly amplified disturbances were sinuous. Data obtained in this investigation attribute the lack of universality of the self-preserving wake, at least partially, to the interaction between the two modes. Certainly, if one is interested in examining the wake over long distances, one cannot neglect the varicose mode of instability.

The scope of the present investigation is limited to the small-deficit wake starting some 100 momentum thicknesses from the generator and extending to 2000 momentum thicknesses downstream. The flow was always incompressible, with free-stream velocities not exceeding 35 m/s and typical Reynolds numbers of a few thousand.

2. Experimental Arrangement

The wakes were generated in the University of Arizona wind tunnel facility. The 80-ft-long tunnel is a closed-circuit type built by Kenney Engineering of California and is nearly identical to its counterparts at Tel Aviv University and the University of Southern California. The test section is 2 ft wide, 3 ft high, and 20 ft long. The top and bottom walls, which are adjustable in height, were adjusted to compensate for boundary-layer growth and to obtain a zero streamwise pressure gradient. A 30 hp. variable-speed motor with tachometer generator and a motor controller drives an axial flow fan with variable-pitch blades. The blades were set to their minimum pitch angle to minimize large-scale turbulence generation. In this configuration, the fan

easily supplied the necessary range of speeds in the test section required for the present study, that is, 2 to 35 m/s. The tunnel is equipped with chilled water cooling coils just downstream of the diffuser section and an electric heating unit just upstream of the fan to control the flow temperature. A Minco platinum resistance thermometer, connected to a special bridge and digital panel display unit, allows measurement of the mean temperature of the flow to ± 0.05 °C.

The plenum chamber contains 4-inch-thick hexcell honeycomb, five 20-mesh stainless-steel screens, and a 4-ft stilling section. Following this section is the 10:1 contraction section with a fifth-order polynomial contour to ensure separation-free acceleration of the flow to the test section. The wake generators were mounted horizontally across the 2-foot span of the test section at a streamwise location 2 feet downstream from the inlet. Measurements of the velocity profile at this plane indicated that the flow was uniform to ± 0.25 %. The free-stream disturbance level in the streamwise velocity component is approximately 0.03 %. The free-stream speed was monitored using a pitot tube placed 1 foot below the wake generator and about 2 inches into the flow. The Pitot tube was connected to an MKS Baratron pressure transducer unit.

Velocities were measured using a rake of nine Disa 55P01 hot-wire probes connected to Disa 55M01 and 56C01 constant temperature anemometers. The rake, which was 1.75 inches in total height, was used to measure the mean streamwise component of the instantaneous velocity. The rake was mounted on an internal traversing mechanism with a swept-forward, thin extension arm, placing the probes upstream of any region of flow interference caused by the mechanism. The mechanism permitted traversing in the streamwise and vertical directions with resolutions of 0.10 and 0.01 inch, respectively. The anemometer signals were conditioned using buck and gain amplifiers and simple low pass RC filters with a 6-dB cutoff point at 10 kHz. The conditioned signals were sent directly to the analog-to-digital converter in the data acquisition system. An LSI 11/23 data acquisition/on-line computer system was used for digital signal processing. The major components of the system include an LSI 11/23 microprocessor, a 15-bit A/D converter with 10 channels of simultaneous sample-and-hold circuitry; a dual-density, 125-ips, tape drive; a 160 M-byte hard disk; 256 K-byte static memory; a printer/plotter; two Tektronix 4006 graphic terminals; a Tektronix 4611 hard-copy unit; and a SKYMNK array processor. The multiple channel capability allows simultaneous, continuous sampling of up to 10 channels, with variable sampling frequency up to 10 kHz. The system can be used as a data logger, i.e. to create digital tapes, or as an on-line computer for real-time analysis.

For calibration, the hot wires were placed in the free stream, well outside the wake, along with a Pitot tube which was mounted near the rake. The bridge voltage signals and the output of the pressure transducer connected to the Pitot tube were sent to the A/D converter. An n th-order polynomial, $U = P_n(E)$, where the independent variable E is the conditioned bridge voltage, was fit to several calibration velocities for each hot wire, thereby providing an overall calibration for each sensor. The wires were calibrated only over the range of velocities to be measured in the wake, typically $0.80 U_\infty$ to $1.05 U_\infty$. Whenever the velocity deficits exceeded $0.20 U_\infty$, a second-order polynomial was used; whereas for $u_0 < 0.10 U_\infty$, a linear fit was adopted, speeding on-line computations.

During the course of the experiments, the temperature of the flow was maintained at ± 0.10 °C of the calibration temperature. The hot wires were continuously checked

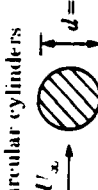
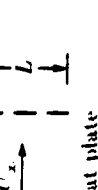
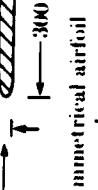
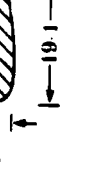
Wake generators	$L_x \times$ width (mm)	$\frac{U_\infty L}{\nu}$	$\frac{U_\infty \theta}{\nu}$	θ (mm)	Remarks
Circular cylinders					
	1.59×610 4.76×610 6.35×610	$1360, 2000, 3000$ $2000, 4000, 5800$ 5800	$640, 925, 1410$ $933, 1930, 3200$ 3220	0.74 $2.23, 2.33, 2.64$ 2.64	$l/d = 384$ Drill rod $l/d = 128$ Drill rod $l/d = 96$ Drill rod
Screws & solid strip					
	8.89×610 6.60×610 4.57×610 2.54×610	— — — —	1980 2010 2040 1970	2.32 2.33 2.39 2.31	Solidity 30% 45% 70% 100% Mesh 28×28 40×40 50×50
Flat plate					
	6.35×610	2780	1035	2.36	Rounded leading edge; tapered to 1 mm.
Symmetrical airfoil					Boundary layer on both sides tripped. Solid aluminum plate
	7.62×610	6500	1996	2.34	Boundary layer tripped. Extruded aluminum tubing filled with sand

TABLE I Summary of wake generators

for drift. The results were sensitive to any minor calibration changes because the maximum velocity deficit was of the order of 5%. Generally, 27-36 data points were taken to define a mean velocity and turbulence intensity profile.

Lateral velocity component fluctuations were measured with a four-probe array of symmetric X-wires. The X-wires were calibrated in the free-stream portion of the wind tunnel using an anemometer response equation of the form

$$U - A_{3,j} V = P_j(E_j) \quad (j = 1, 2), \quad (2.1)$$

where U and V are the calibration velocity components, E_j is the anemometer bridge voltage, and P_j is a second-order polynomial given by

$$P_j(E_j) = \sum_{n=0}^2 A_{nj} E_j^n. \quad (2.2)$$

The X-wires were calibrated at 20 points (4 velocities and 5 yaw angles in the range $\pm 10^\circ$) and the unknown constants A_{nj} , $n = 0, \dots, 3$ and $j = 1, 2$, were solved by least-squares fit. The instantaneous velocity components U and V could then be computed from

$$V(t) = \frac{P_1(E_1) - P_2(E_2)}{A_{3,2} A_{3,1}}, \quad U(t) = P_1(E_1) - A_{3,1} V. \quad (2.3)$$

Again, the wires were calibrated only over the range of velocities to be measured in the wake.

The wake generators used in the present experiments are described in table 1. The circular cylinders were steel, drill rods and the screens and solid strip were stainless steel. The cylinder, screens, and solid strip were all mounted under adequate tension to ensure that the generators were straight and rigid. The screens and solid strip were specially constructed to have the same momentum thickness as the $\frac{1}{16}$ -inch-diameter (4.76 mm) cylinder at $Re_d = 4000$. The aspect ratio \mathcal{L}/d was approximately 240 for the referred cases. To introduce controlled excitations into the wake, a small flap (5 mm in length) was attached to the trailing edge of the flat plate and airfoil. Violin strings were used to connect the downstream edge of each side of the flap to two matched loudspeakers, one located on each side of the plate just outside the tunnel sidewalls. The speakers were driven in phase at the desired amplitudes and frequencies by an audio amplifier fed by a Krohn Hite function generator. The forcing frequency and amplitude were monitored by a frequency counter and r.m.s. meter.

3. Theoretical considerations

3.1. Similarity conditions

For a developing wake flow sufficiently far from the generator, the transverse distributions of mean velocity and Reynolds stresses are assumed to be self-preserving. That is, these distributions assume functional forms which are independent of x when normalized by the velocity and length scales, u_0 and L_0 respectively. This can be expressed in the form

$$\left. \begin{aligned} U &= U_x - u_0 f(\eta), \\ \bar{u}^2 &= u_0^2 g_{11}(\eta), \\ \bar{u}\bar{v} &= u_0^2 g_{12}(\eta), \\ \bar{v}^2 &= u_0^2 g_{22}(\eta), \\ \bar{w}^2 &= u_0^2 g_{33}(\eta). \end{aligned} \right\} \quad (3.1)$$

where $\eta = y/L_0$ and u_0 and L_0 are defined in figure 1. In general, u_0 and L_0 will be functions of the following parameters:

$$u_0, L_0 = \text{fens}(x, \rho, u, U_\infty, F, \mathcal{L}, d, \text{geo}, u'_{\text{FS}}, N_{\text{FS}}, \text{others}) \quad (3.2)$$

where

\mathcal{L} = span of the wake generator.

d = characteristic width of the wake generator.

geo = geometry of the wake generator.

u'_{FS} = amplitude of the free-stream disturbance level.

N_{FS} = nature of the free-stream disturbance.

F = drag force on the wake generator per unit length.

others = magnitude and nature of any vibration of the wake generator.

The conditions under which self-preserving flow is possible can be obtained by substituting the self-preserving distributions into the equations of mean momentum and turbulent kinetic energy and examining the coefficients in the resulting equations. For the small-deficit far wake in the absence of a pressure gradient, i.e. when $u_0/U_\infty \ll 1$, Townsend (1970) obtains the conditions

$$\frac{U_\infty L_0}{u_0^2} \frac{du_0}{dx} \propto \frac{U_\infty}{u_0} \frac{dL_0}{dx}. \quad (3.3)$$

The self-preserving functions are also subject to the momentum integral constraint

$$\frac{F}{\rho U_\infty^2 \theta} = \int_{-\infty}^{\infty} \frac{U}{U_\infty} \left(1 - \frac{U}{U_\infty}\right) dy = \theta. \quad (3.4)$$

where θ is the momentum thickness. In terms of the self-preserving function, f , this becomes

$$\frac{F}{\rho U_\infty^2 \theta} = \frac{u_0 L_0}{U_\infty \theta} \mathcal{J}_1 - \frac{u_0^2 L_0}{U_\infty^2 \theta} \mathcal{J}_2. \quad (3.5)$$

where

$$\mathcal{J}_n = \int_{-\infty}^{\infty} f^n(\eta) d\eta \quad (n = 1, 2). \quad (3.6)$$

are constants for a given wake flow. However, (3.4)–(3.6) are only consistent with (3.3) when $u_0/U_\infty \ll 1$ and the second term in (3.5) is dropped. This places a constraint on the product $(u_0 L_0)$ of the two scales, since in the absence of a pressure gradient, F , θ , and U_∞ are constants independent of x . Dimensional reasoning, along with the linear part of (3.5), indicates the variables, F , ρ , and U_∞ in equation (3.2) should appear in the combination $F/\rho U_\infty$ [see also (3.4)]. It can be easily shown from (3.3) and (3.4) that

$$\frac{u_0}{U_\infty} \sim \left[\frac{F}{\rho U_\infty^2 (x - x_0)} \right]^{\frac{1}{2}} \sim \left[\frac{\theta}{x - x_0} \right]^{\frac{1}{2}}. \quad (3.7)$$

and

$$L_0 \sim \left[\frac{F(x - x_0)}{\rho U_\infty^2} \right]^{\frac{1}{2}} \sim [\theta(x - x_0)]^{\frac{1}{2}}. \quad (3.8)$$

where x_0 , the virtual origin, is commonly assumed to depend on the Reynolds number and geometry of the generator. This indicates that θ is the appropriate normalizing length scale.

If a universal self-preserving state exists independent of initial conditions, free-stream disturbances, and other parameters, the normalized distribution functions f

and g_s are universal functions and u_0 and L_0 , the normalized velocity and length scales, should vary as

$$\left(\frac{U_x}{u_0}\right)^2 = A\bar{x}, \quad (3.9)$$

and

$$\left(\frac{L_0}{\theta}\right)^2 = B\bar{x}, \quad (3.10)$$

where $\bar{x} = (x - x_0)/2\theta$ and A and B are universal constants. The factor 2θ is used to normalize x because $2\theta = C_D d$, which is nearly equivalent to normalization by d since for circular cylinders $C_D \approx 1$. Townsend (1956) and others used d in presenting their cylinder data.

According to Sreenivasan & Narasimha (1982), (3.7) and (3.8) may be written in the form

$$W = \frac{u_0}{U_x} \left(\frac{x}{\theta}\right)^{\frac{1}{2}} \quad (3.11)$$

and

$$\Delta = L_0(x\theta)^{-\frac{1}{2}} \quad (3.12)$$

where W and Δ are universal constants, provided the small-deficit, equilibrium wake is independent of initial conditions existing near the generator (see also Narasimha & Prabhu 1972). These parameters are related to the slopes in the relations (3.9) and (3.10) above. If we define W_0 and Δ_0 by (3.11) and (3.12), where x is replaced by $x - x_0$, then $A = 2/W_0^2$ and $B = 2\Delta_0^2$.

3.2. Linear stability analysis

The propagation of small-amplitude, wavy disturbances in a free shear layer was considered analytically by Bouthier (1972), Crighton & Gaster (1976), and Gaster *et al.* (1985). Since the analysis applied to the plane wake is identical to that presented in the latter reference, only the governing equations and essential features will be presented here.

The equation of motion considered is inviscid and has the following form

$$\frac{\partial \Omega}{\partial t} + U \frac{\partial \Omega}{\partial x} + V \frac{\partial \Omega}{\partial y} = 0, \quad (3.13)$$

where Ω is the vorticity and U and V represent the velocity components in the x - and y -directions, respectively. Upon neglecting the nonlinear terms, which are deemed to be small, and assuming that a given mean flow is parallel to the first order of approximation, the solution for the perturbation equation has a general form

$$\psi = RP \{ \phi(y) \exp [i(\alpha x - \beta t)] \}, \quad (3.14)$$

where RP stands for the real part and the eigenfunction $\phi(y)$ is defined by the inviscid form of the Orr-Sommerfeld equation

$$\left[U(y) - \frac{\beta}{x} \right] (\phi'' - \alpha^2 \phi) - U''(y) \phi = 0, \quad (3.15)$$

in which the primes denote differentiation with respect to y . The wave number α and the disturbance frequency β are eigenvalues determined by the solutions of (3.15).

which decay exponentially on both sides of the wake. Namely, the boundary conditions are

$$\phi'(\pm\infty) \pm \alpha\phi(\pm\infty) = 0. \quad (3.16)$$

Although the divergence of the mean flow may be partially controlled by the stresses resulting from the interaction with the disturbances present, within the realm of the linear approximation the slowly divergent mean flow is assumed to be prescribed by equations (3.1). Since the mean flow is assumed to be known, the conditions of self-preservation are not crucial to the analysis; the only requirement is that the derivatives of the mean stream function ψ with respect to x should be much smaller than the derivatives with respect to y (i.e. the boundary-layer approximation applies).

By analogy with the parallel flow problem, the perturbation solution has the form

$$\psi = RP \left\{ A(x) \phi(x, y) \exp \left[i \int_{x_0}^x \alpha(x) dx - \beta t \right] \right\}, \quad (3.17)$$

where $\alpha(x)$ is a local wavenumber and the eigenfunction $\phi(x, y)$ changes only slowly with x . Since one expects the correction terms resulting from the slow divergence to be small, $\alpha(x)$ and $\phi(x, y)$ at a given streamwise location are still determined locally by (3.15), for which the mean velocity field $U(x, y)$ is known, and the correction term is defined by

$$A(x) = A_0 \exp \left[- \int_{x_0}^x \frac{N(x)}{M(x)} dx \right],$$

where

$$N(x) = \int_{-\infty}^x \left\{ \beta \left[\phi \frac{\partial \alpha}{\partial x} + 2x \frac{\partial \phi}{\partial x} \right] + U \left[\frac{\partial \phi''}{\partial x} - 3\alpha^2 \frac{\partial \phi}{\partial x} - 3\alpha\phi \frac{\partial \alpha}{\partial x} \right] \right. \\ \left. + \phi' \frac{\partial U'}{\partial x} + U'' \frac{\partial \phi}{\partial x} + V [\phi''' - \alpha^2 \phi] \right\} \tilde{\phi} dy, \quad (3.18)$$

$$\text{and } M(x) = \int_{-\infty}^x \{2x\beta\phi + U[\phi'' - 3\alpha^2\phi] - U''\phi\} \tilde{\phi} dy,$$

where $\tilde{\phi}(x, y)$ is the adjoint function of $\phi(x, y)$ given by

$$\left[U(x, y) - \frac{\beta}{\alpha} \right] [\phi'' - \alpha^2 \phi] + 2U' \phi' = 0. \quad (3.19)$$

with the boundary conditions presented by

$$\tilde{\phi}'(\pm\infty) \pm \alpha\tilde{\phi}(\pm\infty) = 0. \quad (3.20)$$

When the mean velocity profile is symmetrical with respect to the line $y = 0$, the inviscid Orr-Sommerfeld equation admits both symmetrical (varicose) and antisymmetrical (sinuous) modes of disturbances. For parallel flow, one may take advantage of the symmetry and substitute a boundary condition on the centreline for the boundary conditions on one side of the wake.

$$\phi(0) = \tilde{\phi}(0) = 1, \quad \phi'(0) = \tilde{\phi}'(0) = 0. \quad (3.21)$$

for the sinuous mode of disturbance, or

$$\phi(0) = \tilde{\phi}(0) = 0, \quad \phi'(0) = \tilde{\phi}'(0) = 1. \quad (3.22)$$

representing the varicose mode. By virtue of the symmetry, one may usually confine attention to the semi-infinite interval $(0, +\infty)$ as in the parallel flow computations.

For a given real frequency β of the disturbance, the complex eigenvalues $\alpha(x)$ and eigenfunctions $\phi(x, y)$ and $\tilde{\phi}(x, y)$ were evaluated at each of the streamwise locations of interest, provided the imaginary part $\alpha_i(x) < 0$ (i.e. the disturbances in the quasi-parallel flow approximation are amplified in the downstream direction), and these solutions were used in determining $A(x)$. The mean velocity field used in solving (3.15), (3.18) and (3.19) was obtained experimentally and was expressed by the exponential distribution

$$\frac{U}{U_\infty} = 1 - \frac{u_0}{U_\infty} \exp[-0.637\eta^2 - 0.056\eta^4]. \quad (3.23)$$

where U_∞ is the free-stream velocity and $u_0(x)$ and $L_0(x)$ are the velocity and length scales discussed in §3.1. Despite the fact that the normalized shape of the velocity profile, $f(\eta)$, remained invariant for all wake generators considered, the eigensolutions had to be re-evaluated for each generator separately since $u_0(x)$ and $L_0(x)$ are dependent on the conditions at the generator, even for the small-deficit wakes.

Sato & Kuriki (1961) considered the temporal evolution of the small-amplitude, sinuous disturbance at a single location in the flow at which $(1 - u_0/U_\infty) = 0.692$. Mattingly & Criminale (1972) extended these calculations to both modes of instability evolving spatially and temporally at five prescribed locations in the immediate vicinity of the trailing edge of a flat-plate [i.e. for $0.44 > (1 - u_0/U_\infty) > 0$]. Since these computations are strongly dependent on u_0/U_∞ , the solutions obtained are of little value in predicting the character of the amplified disturbances in the small-deficit wake for which $u_0/U_\infty \ll 1$. Furthermore, the assumption of parallel mean flow (i.e. the constancy of u_0/U_∞ and of L_0/θ) led to the general belief that the varicose mode has a negligible effect on the flow because its rate of amplification ($-\alpha_i$) is smaller. It will be shown later that even a superposition of the two modes of instability leads to physically acceptable flow patterns associated generally with large coherent structures contained in the wake, in spite of the presence of the turbulent fluctuations, which was not considered in the calculations.

4. Experimental results

4.1. General

The mean flow field in the self-preserving region of a wake, the turbulence intensities, and Reynolds stresses were measured for a variety of two-dimensional wake generators. Data were obtained at distances ranging from 100 to 2000 momentum thicknesses downstream of the generator, where typical velocity deficits on the centreline of the wake varied from $0.15 U_\infty$ to $0.03 U_\infty$. The velocity at which the measurements were done varied from 7 to 20 m/s, corresponding to a range of Reynolds numbers based on the momentum thickness and the kinematic viscosity of air of 650 to 3200. In most instances, the shape and the size of the wake generators were tailored to provide a constant momentum thickness. The effects of Reynolds number and aspect ratio were examined separately in wakes generated by circular cylinders. Forced sinuous disturbances were generated in the wake of a symmetrical airfoil (having a maximum thickness to chord ratio of 30 %) and a flat plate (thickness to chord ratio of 2 %) by an oscillating, small flap mounted at the trailing edge. The results are summarized in table 2.

Wake generator	U_∞ (m/s)	θ (mm)	$\frac{x_0}{2\theta}$	W_0	Δ_0	$W_0 \times \Delta_0$
$\frac{1}{8}$ in. Cylinder	14.5	2.33	-74	1.75	0.289	0.506
30% Solidity screen	14.5	2.31	58	1.82	0.279	0.508
45% Solidity screen	14.5	2.33	27	1.78	0.285	0.507
70% Solidity screen	14.5	2.39	-21	1.67	0.302	0.504
Solid strip 100% solidity	14.5	2.31	-64	1.88	0.270	0.508
Symmetrical airfoil	14.5	2.34	-190	1.56	0.320	0.500
Flat plate	7.45	2.36	5	1.71	0.297	0.508
Flat plate flap freq. = 50 Hz AMP = 0.2 V	7.45	2.36	48	1.48	0.344	0.509
Flat plate flap freq = 50 Hz AMP = 0.3 V	7.45	2.46	61	1.32	0.382	0.504
Flat plate flap freq = 20 Hz AMP = 0.5 V	7.45	2.40	48	1.57	0.323	0.507
$\frac{1}{8}$ in. Cylinder (Chapman 1982)	20.7	2.54	-100	1.74	0.288	0.501
$\frac{1}{8}$ in. Cylinder	21.4	0.737	-170	1.77	0.285	0.504
$\frac{1}{8}$ in. Cylinder	14.5	0.737	-130	1.74	0.287	0.500

TABLE 2.

4.2. The universality of the mean flow field in a small-deficit, plane wake

The wake investigated most extensively is that generated by a circular cylinder, and therefore our investigation started with this wake generator. Some 400 momentum thicknesses downstream, the velocity scale u_0 was indeed proportional to $\bar{x}^{-\frac{1}{4}}$, and the width of the wake L_0 was proportional to $\bar{x}^{\frac{1}{4}}$, suggesting that similarity of the mean flow was indeed attained. The mean velocity profiles were plotted in the similarity coordinates and collapsed quite neatly onto a single curve described by the exponential function

$$f(\eta) = \exp [-0.637\eta^2 - 0.056\eta^4], \quad (4.1)$$

(figure 3). The exponential function traditionally used to describe the mean velocity profile (i.e. $f(\eta) = \exp [-0.693\eta^2]$) overestimates the mean velocity measured at the outer edges of the wake and, therefore, the fourth-order correction term was added. We expected the flow to be independent of Re when all lengthscales were normalized by the momentum thickness, and indeed the values of W_0 and Δ_0 were not affected by changes in Re ranging from $Re_d = 1360$ to $Re_d = 5900$. The aspect ratio of the cylinder was varied from 96 to 384 by changing the diameter of the cylinder and keeping the span constant (i.e. the distance between the sidewalls of the wind tunnel). The two-dimensionality of the mean flow field was checked at $\bar{x} = 430$ by comparing velocity and turbulence intensity profiles obtained at $z/L_0 = 0 \pm 7.5$ and was found to be satisfactory. The values of $W_0 = 1.75$ and $\Delta_0 = 0.287$ fitted quite well all wakes generated by a circular cylinder (the values were averaged over experimental points with $\bar{x} > 200$). This result would give credence to the universal equilibrium concept suggested by Sreenivasan & Narasimha (1982), except that the asymptotic values of

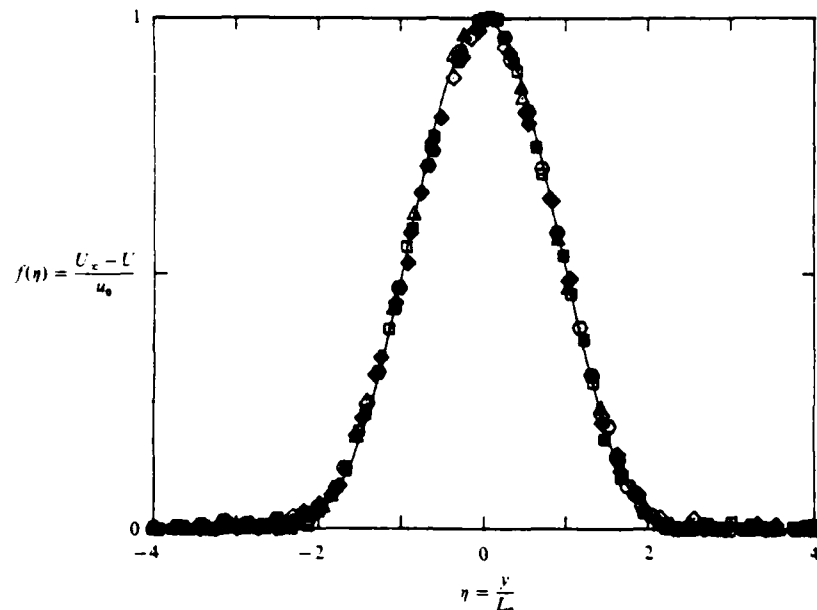


FIGURE 3. The shape of the self-similar mean velocity profile. Data from 30% solidity screen for $200 < \bar{x} < 700$.

the constants suggested by these authors were quite different, i.e. $W_0 = 1.63$ and $\Delta_0 = 0.300$. The present data on the downstream development of the mean flow field behind a circular cylinder agree quite well with those obtained by Symes & Fink (1977) and Yamada *et al.* (1980), but only partially with Townsend's (1956) data. Our data on the mean wake growth, $L_0(x)$, agree with Townsend's but not the corresponding data on $u_0(x)$. It should be noted that there are very little data available on the mean wake growth and $u_0(x)$, even for circular cylinders, and this is undoubtedly attributable to the difficulty of obtaining such data.

The uniqueness of the mean velocity profile and the mean wake development for circular cylinders *in our facility* could lead to the conclusion that either the development of the plane, small-deficit wake is not susceptible to external disturbances or the velocity-dependent external disturbances in our wind tunnel (like the fan-blade passage-frequency, vibrations, etc.) are negligible within the range of variables considered. To answer this question, we could take our cylinders to other wind tunnels and repeat our experiments, but such testing could introduce new uncertainties over which we have no control. To avoid these difficulties, we addressed a related question. That is, in a given facility, are the x development of u_0 and L_0 dependent on the nature of the wake generator, holding all other controllable variables constant? We proceeded, therefore, to investigate wakes produced by a variety of two-dimensional generators. The first family of generators considered were screens with solidity ratios ranging from 30 to 100% (a thin metal strip placed normal to the free stream). The porous screens have numerous advantages: (i) there is no flow reversal in the vicinity of the generator with all its ensuing experimental complications; (ii) the porous screens do not generate vortices in the same way as the circular cylinders do and, therefore, their drag should not be as sensitive to Reynolds number; (iii) the roll-up of vortices in the mixing layers generated in the neighbourhood of the screens is, in

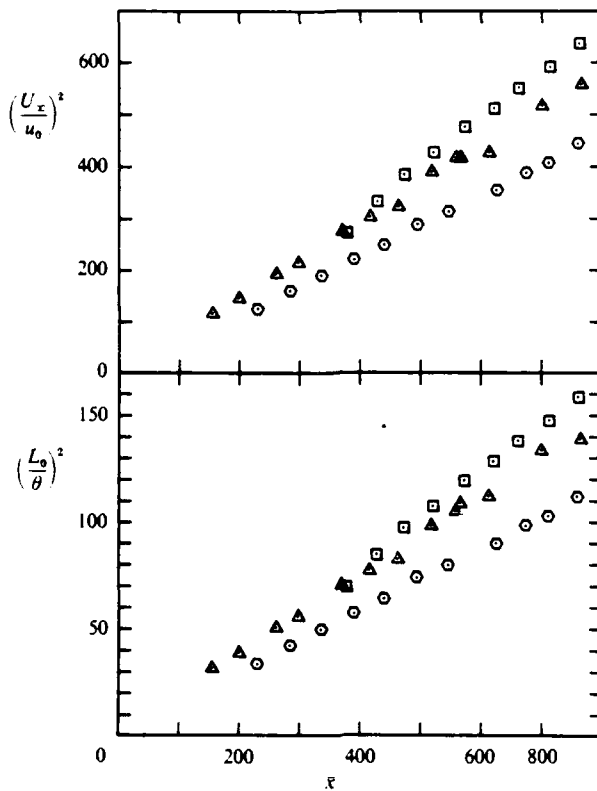


FIGURE 4. The variation of u_0 and L_0 with \bar{x} for three wake generators: \square , airfoil; \triangle , 70% solidity screen; \circ , solid strip.

principle, predictable and dependent on the solidity (Gaster *et al.* 1985); and (iv) the drag of screens having a different solidity can easily be equated by altering the size of the screens. It was decided to maintain the momentum thickness of all four screens constant in order to avoid any questions about the unknown effects of Reynolds number or aspect ratio in the development of the plane, small-deficit wake. The results show that the shape of the normalized mean velocity profile is identical to that obtained for the circular cylinder in all cases considered, yet the values of W_0 range between 1.67 for the 70% solidity screen to 1.88 for the limiting case representing the solidity of 100%.

The value of W_0 decreases with increasing solidity of the screens, provided the porosity suffices to prevent flow reversal in the lee of the screen; however, the value of W_0 for the solid strip (which is regarded as a screen having 100% solidity) is higher than the value of W_0 for the most porous screen investigated (solidity of 30%). This result is attributed to the observed alternate shedding of vortices from the two separation points on the strip. The determination of the threshold solidity beyond which an alternate shedding of vortices starts to occur is not within the scope of the present investigation.

In the absence of periodic forcing, the lowest W_0 measured in this experiment was attained in the wake of a non-lifting, thick, symmetrical airfoil section. The mean velocity field in the wake of the flat plate was nearly identical to the velocity field produced by the wake of a circular cylinder except for the location of the virtual origin

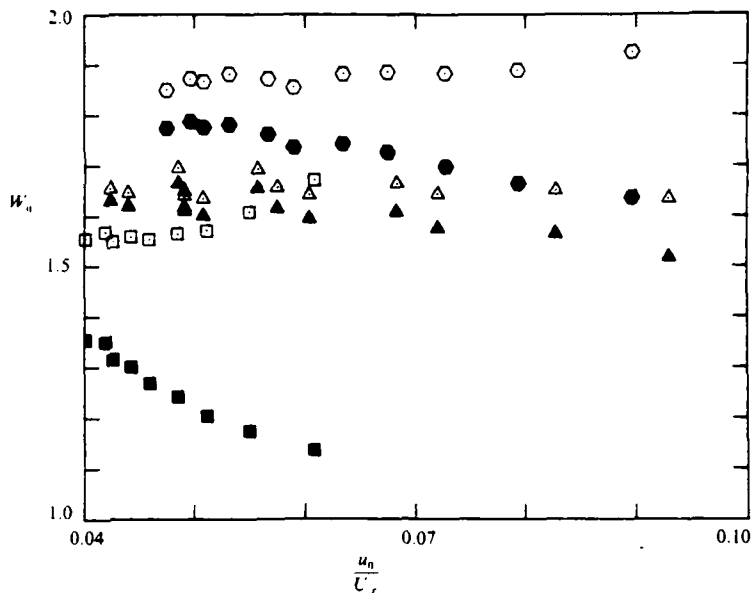


FIGURE 5. The variation of W_0 with u_0/U for three wake generators: \square —■, airfoil; \triangle —▲, 70% solidity screen; \circ —●, solid strip.

x_0 . The introduction of periodic surging reduced the effective W_0 from 1.71 to 1.56 without affecting the overall drag experienced by the body (i.e. the product $W_0 \Delta_0$). The location of the virtual origin moved downstream with increasing amplitude of the forced oscillations (table 2).

The product $W_0 \Delta_0$ represents the conservation of momentum within the context of the linearization and, therefore, its constancy for all wake generators ($W_0 \Delta_0 = 0.506 \pm 0.002$) reaffirms the suggestion that the normalized shape of the mean velocity profile (figure 3) is universal for all the wake generators considered. Some examples of the variation of $(U_x/u_0)^2$ and $(L_0/\theta)^2$ with \bar{x} are shown in figures 4(a) and (b), respectively, establishing that the coefficients of proportionality A and B [(3.9) and (3.10)] or W_0 and Δ_0 depend on the wake generator.

The mean velocity in the wake obeys the similarity scaling for $\bar{x} > 400$. The different slopes of the lines drawn in figure 4(a) result in a diversity of estimates for W_0 (figure 5), varying between 1.5 and 1.9 depending on the wake generator. The differences are large and are not attributable to experimental inaccuracy.

Only one value of x_0 was chosen for each wake generator, and it had to satisfy the dependence of both u_0 and L_0 on initial conditions. The choice of x_0 does not affect the dependence of W_0 or Δ_0 on the initial conditions, although the absolute values of W_0 and Δ_0 may vary slightly if improper values of x_0 were used. Figure 5 demonstrates this point. The open symbols refer to physical distances measured from the trailing edge of the generator (i.e. $x_0 = 0$), and therefore the values of W_0 based on these data define a sloping curve rather than a horizontal line. This effect is particularly severe whenever x_0 is large, as it is in the wake of the symmetric airfoil. It is apparent, therefore, that for the range of distances considered, the mean flow in the plane, small-deficit, turbulent wake is dependent on the initial conditions set up by the generator.

The preservation of momentum deficit in the wake produced by all the generators

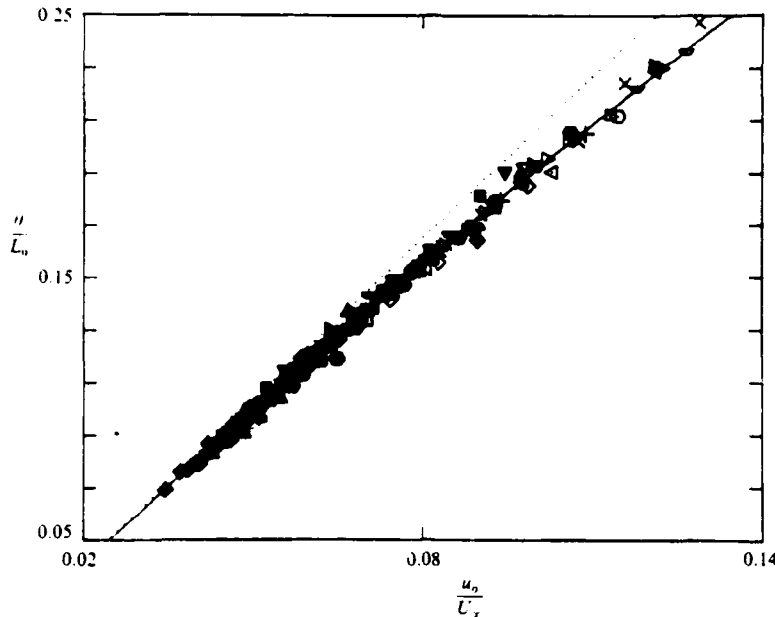


FIGURE 6. The dependence of θ/L_0 on u_0/U_∞ . Symbols represent data from all wake generators studied.

considered above is illustrated by plotting θ/L_0 versus u_0/U_∞ (figure 6). For similar velocity profiles,

$$\frac{\theta}{L_0} = \frac{u_0}{U_\infty} \left(\mathcal{J}_1 - \frac{u_0}{U_\infty} \mathcal{J}_2 \right), \quad (4.2)$$

with \mathcal{J}_n as defined in (3.6).

Equation 4.2 describes a parabola (a solid curve in figure 6), while the linear approximation $(\theta/L_0)(U_\infty/u_0) = \mathcal{J}_1$ is drawn as a dotted line. The values of \mathcal{J}_1 and \mathcal{J}_2 are 2.06 and 1.505, respectively, and are in excellent agreement with the data of Sreenivasan & Narasimha (1982). Measured values of θ/L_0 follow quite clearly the parabolic curve for all $u_0/U_\infty < 0.14$. One can obtain an expression for θ/L_0 by eliminating \bar{x} from (3.9) and (3.10), which yields

$$\frac{\theta}{L_0} = \frac{1}{W_0 A_0} \frac{u_0}{U_\infty}. \quad (4.3)$$

The quantity $(1/W_0 A_0)$ was found to be 1.97 as opposed to $\mathcal{J}_1 = 2.06$, and therefore (4.3) represents a better approximation to the data than does the linear approximation to (4.2).

4.3. The lack of universality of the turbulent field

For a self-preserving wake (Townsend 1956), the transverse distributions of the intensities and Reynolds stresses are given by (3.1), where the g functions are supposedly universal functions analogous to $f(n)$. In particular, the longitudinal component of the turbulent intensity and the shear stress are given by

$$\bar{u}^2 = u_0^2 g_{11}(\eta). \quad (4.4)$$

$$\bar{u}\bar{v} = u_0^2 g_{12}(\eta). \quad (4.5)$$

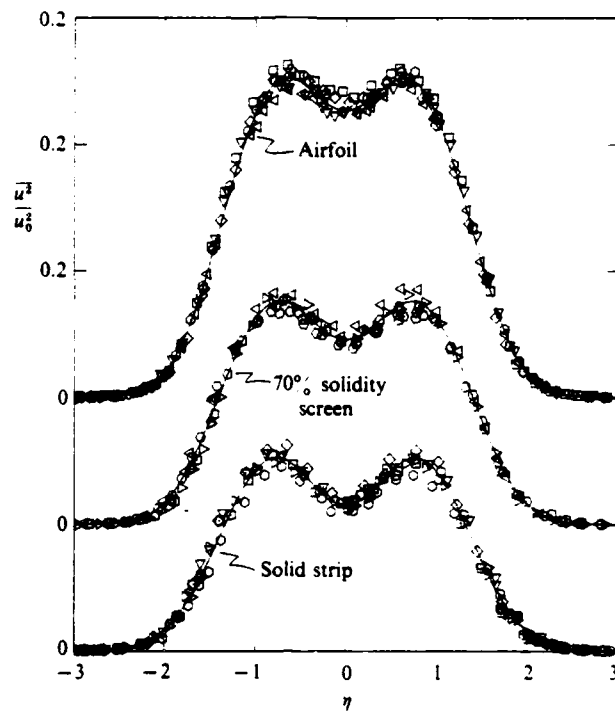


FIGURE 7. The measured distributions of $g_{11}(\eta)$ for the solid strip, the 70% solidity screen, and the symmetric airfoil. The different symbols represent different downstream locations. The solid lines represent the best fit to each data set.

The measured distributions of $g_{11}(\eta)$ for the solid strip, 70% solidity screen, and the symmetric airfoil are shown in figure 7. The data indicate that although each wake is approximately self-similar, the function $g_{11}(\eta)$ depends on the nature of the wake generator. To elucidate the differences in the measured \bar{u}^2 distributions, we plotted a normalized function defined by

$$\bar{u}^2 = \bar{u}_{\max}^2 G_{11}(\eta). \quad (4.6)$$

which is shown in figure 8 for the three data sets. A good measure in assessing the lack of universality is the ratio $\bar{u}_{\text{CL}}^2/\bar{u}_{\max}^2$ (where the subscript CL refers to the centre plane of the wake), which varies from 0.76 for the solid strip to 0.9 for the airfoil. This ratio is correlated with the rate of spread of the wake or the decay of the mean velocity on the centreline.

The degree to which each of the wakes approaches a self-preserving state can be determined from figure 9, which shows the downstream variation of the square root of \bar{u}_{\max}^2/u_0^2 . For a self-preserving state, this statistic should be a constant, independent of x . Notice that the wake behind the solid strip reaches a self-preserving state more rapidly than the wakes behind the screen or airfoil. (Recall that the airfoil wake has a large negative value of x_0 .) The self-preserving nature of $g_{12}(\eta)$, the normalized shear stress, for the airfoil can be determined from figure 10, where stress distributions at 8 downstream locations in the range $485 < \bar{x} < 800$ are presented. Similar results were obtained for the solid strip and 70% solidity screen. These data were obtained at a free-stream velocity of 7.5 m/s, rather than 14.5 m/s, because we had better control

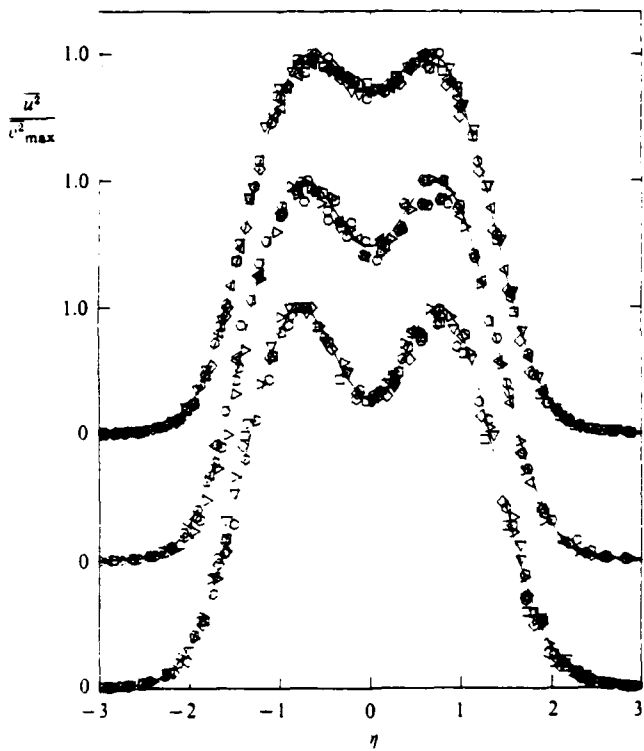


FIGURE 8. The normalized turbulent intensity distributions for the three generators. The value of $\bar{u}_{\text{CL}}^2/\bar{u}_{\max}^2$ for each generator is indicated. The solid lines represent the best fit to each data set.

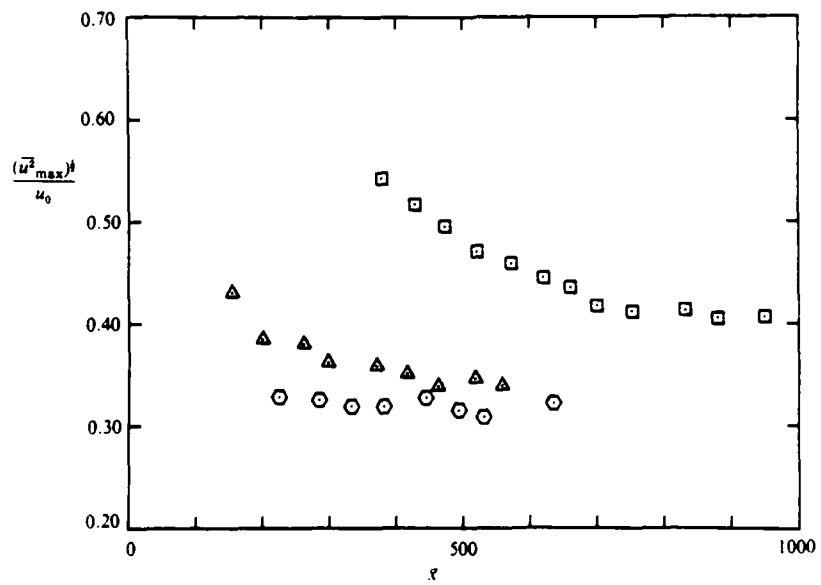


FIGURE 9. The downstream variation of $(g_{11,\max})^{\frac{1}{2}}$ for the three generators: \square , airfoil; Δ , 70% solidity screen; \circ , solid strip.

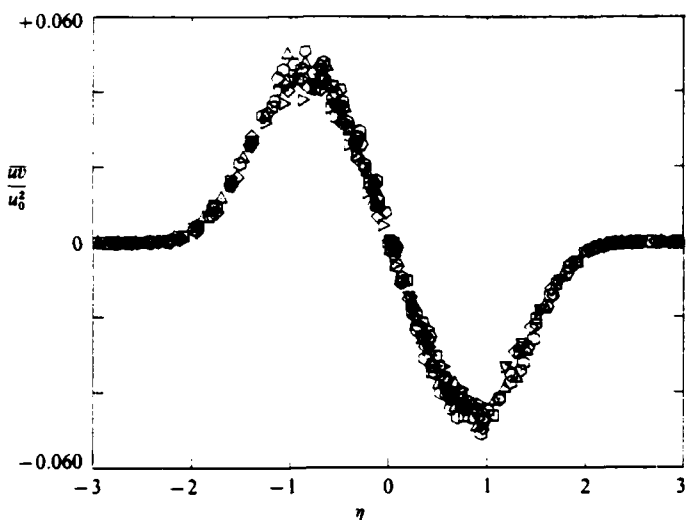


FIGURE 10. The measured distributions of $g_{12}(\eta)$ for the airfoil at eight downstream locations.

of the temperature of the airflow at the lower velocity. The temperature was maintained to within ± 0.1 °C of the calibration temperature for the X-wire runs. The corresponding Reynolds numbers, Re_0 , for the airfoil are 1260 and 1996, respectively, and certainly no significant change in the flow structure occurs between these Reynolds numbers. The function $g_{12}(\eta)$ attains a self-preserving shape more rapidly than does $g_{11}(\eta)$ for all three wake flows.

A link between the variation in the spreading rate of the mean flow and $g_{12}(\eta)$ in the self-preserving region can be obtained from the mean momentum equation, which in linearized form is given by

$$f + \eta f' = \frac{2W_0}{\Delta_0} g'_{12}. \quad (4.7)$$

This equation can be integrated to yield

$$g_{12}(\eta) = \frac{\Delta_0}{2W_0} \eta f. \quad (4.8)$$

Note that $\Delta_0/2W_0$ varies by 43% between the solid strip and the symmetric airfoil and, therefore, $g_{12}(\eta)$ must also differ by this amount, as $f(\eta)$ is a universal function. Reynolds stress distributions were measured at one downstream x -location for the two wake generators. The downstream location chosen corresponds to \bar{x} values of 614 and 733 for the solid strip and airfoil, respectively, well within the self-preserving region for each wake. The Reynolds number for the measurements is the nominal 2000, the value used to obtain the Δ_0 and W_0 data. Figure 11 shows the measured values of \bar{w}/u_0^2 for the two generators. The solid lines represent the theoretical prediction for each wake based on the linearized momentum equation and $f(\eta)$, i.e. (4.8). Note that the distribution for the airfoil definitely has larger values than that for the solid strip. Similar data were also obtained for the 70% screen and the results fell between those for the solid strip and airfoil, which is consistent with (4.8). The agreement between the data and the linearized theory provides convincing evidence for the lack of universality of the turbulent structure of two-dimensional far wakes.

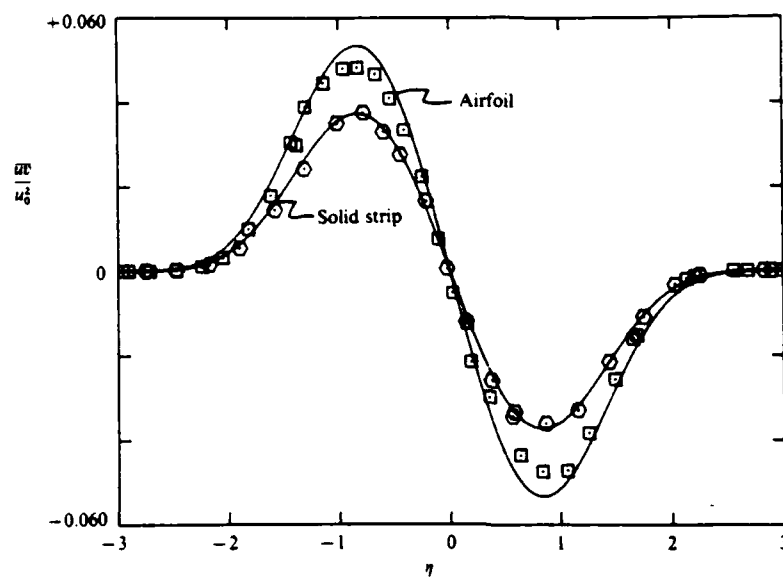


FIGURE 11. The distributions of $\bar{u}v/u_0^2$ for the solid strip and the airfoil. The solid lines represent the linearized theory prediction, equation (4.8). \square , airfoil, $\bar{x} = 733$; \circ , solid strip, $\bar{x} = 614$.

Indeed, the lack of universality of \bar{u}^2_{CL} presented by various investigators for the circular cylinder triggered the present investigation (figure 2). The peculiar shape of $G_{11}(\eta)$, which has a local minimum at $\eta = 0$, is associated with a distribution of large vortices about the centreline of the wake (see Sato & Kuriki 1961; Wygnanski, Oster & Fiedler 1979). It was therefore anticipated that large coherent structures which retain their characteristic shape and associated velocity perturbation are responsible for the apparent dependence of the wake on the conditions at its origins.

4.4. Spectra and normal modes of instability

Spectra of the streamwise component of the velocity fluctuations were measured at several \bar{x} locations in the wake behind the flat plate. The measurements presented in figure 12 were taken on the centreline at $102 < \bar{x} < 587$, while the spectra in figure 13 were measured along a curve representing the outer boundary of the wake, i.e. at $\eta = 3$. Only the most significant decade of the spectra has been plotted. The abscissa on these figures is frequency plotted on a logarithmic scale, while the ordinate is $fF(f)$ in order to represent the relative contribution to the streamwise component of intensity at a given frequency f [i.e. $\bar{u}^2 \propto \int F(f) df = \int fF(f) d(\log f)$].

The spectra measured on the centreline of the wake (figure 12) have a shape which is typically observed in any unbounded, turbulent, shear flow (Champagne 1978). The spectral distribution is broad, and the frequency range associated with the most energetic eddies gradually moves toward lower frequencies as the flow develops in the downstream direction. The insert in figure 12 shows a log-log plot of the normalized (to unity) spectra $F(f)$. The frequency has been rendered non-dimensional using the local length scale, L_0 , and U_x . The similarity of the spectral distribution indicates that the length scales associated with the energy-containing eddies ($\lambda = U_x/f$) are proportional to the width of the wake, L_0 , which is therefore an

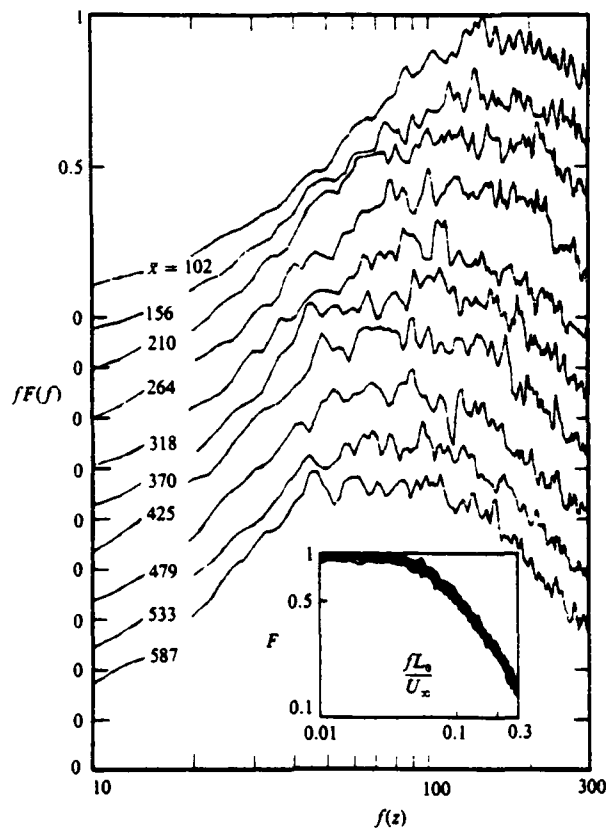


FIGURE 12. Spectra of u fluctuations on centreline of flat-plate wake at various downstream positions. Insert shows similarity of spectra when scaled by L_0 and U_∞ .

appropriate characteristic lengthscale for comparing the mean velocity profiles generated by various obstacles.

The spectral measurements at $\eta = 3$, shown in figure 13, represent fluctuations induced by the passage of the large turbulent structures in the wake since the coordinate $\eta = 3$ is located outside the turbulent interface. The insert in this figure shows that, as with the centreline spectra, these spectra also scale with the local width L_0 . Note the shift of the spectral peaks toward lower frequency with increasing \bar{x} .

Equation (3.15) was solved for the prescribed local mean velocity field and numerous real frequencies to obtain the variation of the spatial rate of amplification ($-\alpha_t$) with increasing distance from the flat plate. The results of these computations indicate that the maximum local amplification rate shifts toward lower frequencies with increasing \bar{x} . Figure 14 shows the spatial amplification rates for different frequencies. The value of \bar{x} for which a constant frequency line intercepts the \bar{x} -axis (i.e. $\alpha_t = 0$) corresponds to the streamwise location at which a wave at that frequency has undergone a maximum amplification according to locally parallel, linear, inviscid stability theory. A plot of these intercepts versus frequency, shown also in figure 14, represents the dependence of the expected predominant frequency in the wake on the distance from the trailing edge of the flat plate. The measured predominant frequency range, defined as those frequencies at $\eta = 3$ whose amplitude is within 90°,

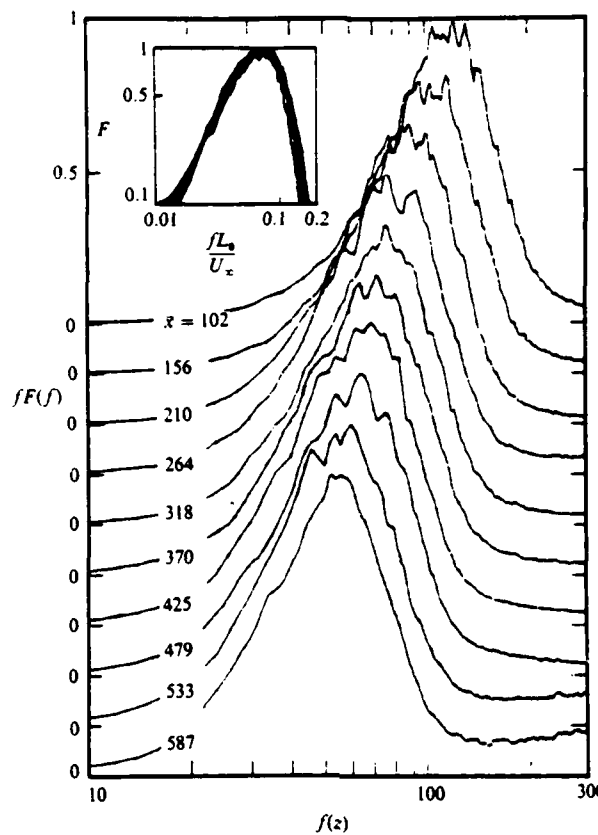


FIGURE 13. Spectra of induced u fluctuations at $\eta = 3$ in the flat-plate wake at various downstream locations. Insert shows similarity of spectra when scaled by L_0 and U_∞ .

of the peak energy value, are plotted in figure 14 and compared with the computed results. The dashed lines show the measured predominant frequency range determined for $\eta = 0$. The good agreement between the measured predominant frequencies associated with the passage of the large coherent structures and the most-amplified frequencies calculated using linear stability theory suggest that the large structures observed in this flow may be related to the two-dimensional instability modes.

4.5. The amplification of imposed sinuous oscillations

Two-dimensional sinusoidal oscillations in the direction normal to the mean flow were generated by the motion of a small flap hinged to the trailing edge of the flat plate. The frequency of the imposed oscillation was matched to the expected most-amplified fluctuations measured at $\eta = 3$ in the region of interest. A typical power spectrum measured with and without excitation is presented in figure 15. Small-amplitude oscillations do not affect the turbulent intensity in the wake nor do they affect the shape of the spectral distribution. The two spectra presented in figure 15 are almost identical, with the exception of the peak corresponding to the frequency of the excitation.

In order to be sure that the instability mechanism in the wake is actually responsible for the amplification of the imposed oscillations, measurements of spectra

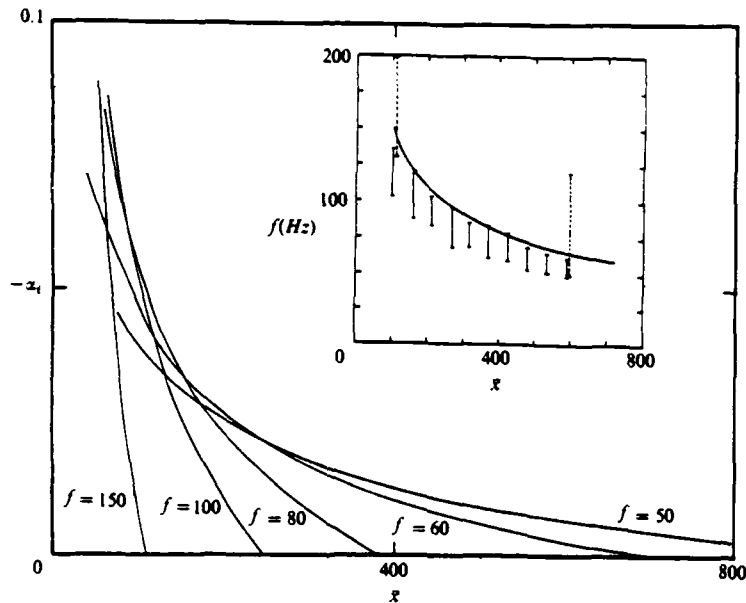


FIGURE 14. Spatial amplification rates computed for several disturbance frequencies in a wake. Insert shows expected predominant frequency (computed) compared to measured predominant frequency range as a function of \bar{x} .

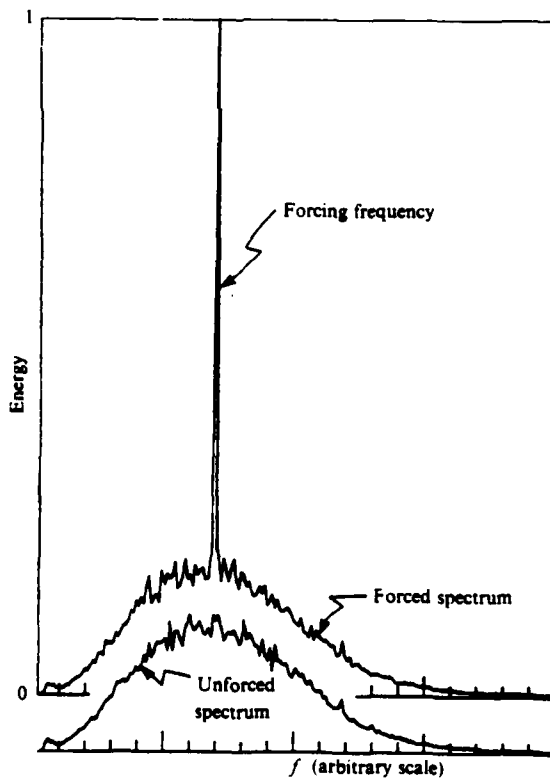


FIGURE 15. The effect of forcing on the measured u spectrum at $\bar{x} = 400$.

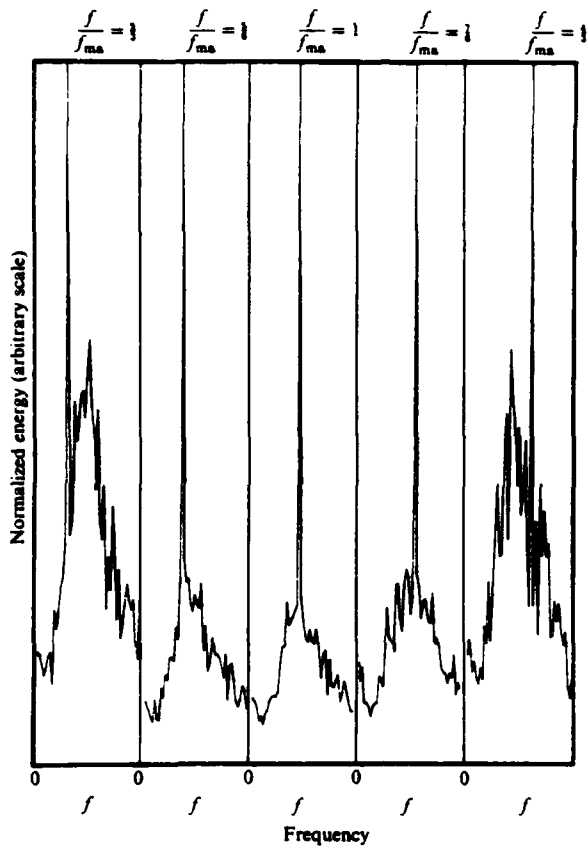


FIGURE 16. The effect of forcing frequency on the velocity spectrum at a fixed location in the wake. $\bar{x} = 400$.

were repeatedly taken at one location in the flow for a variety of forcing frequencies while all other controlled variables were unchanged. Since the background turbulence level is not significantly affected by the introduction of forcing (figure 15), the ratio of the amplitudes between the imposed wave and the background exhibits the sensitivity of the wake to the imposed sinuous perturbations. The normalized spectrum in the centre of figure 16 shows the ratio of amplitudes for the most-amplified frequency at the location considered. When the frequency of forcing was either higher or lower than the most-amplified frequency for the given location and flow conditions, the ratio between the peak amplitude and the background diminished. In view of the symmetry of the response around the most-amplified frequency (figure 16), which was repeated at other flow conditions (and therefore other frequencies), the possibility of resonance of the mechanical flap system was discarded.

The amplitude and phase of an artificially excited sinuous wave at a frequency corresponding to $f\theta/U = 6.4 \times 10^{-3}$ ($f = 20$ Hz) were calculated for the wake of the flat plate. The mean flow required for the solution of (3.15), (3.18) and (3.19) was provided by (4.1) and table 2 (i.e. $W_0 = 1.57$, $A_0 = 0.323$, $\bar{x}_0 = 48$). These equations were solved at intervals of $\bar{x} = 10$ for a rectangular window starting at $\bar{x} = 250$ and ending at $\bar{x} = 750$ and at intervals of 0.1 between $-40 \leq y/2\theta \leq 40$. For a given frequency ($\beta = 2\pi f(L_0)_{x=750}/U_\infty$), the eigenvalues $\alpha(x)$ and eigenfunctions $\phi(x, y)$ and

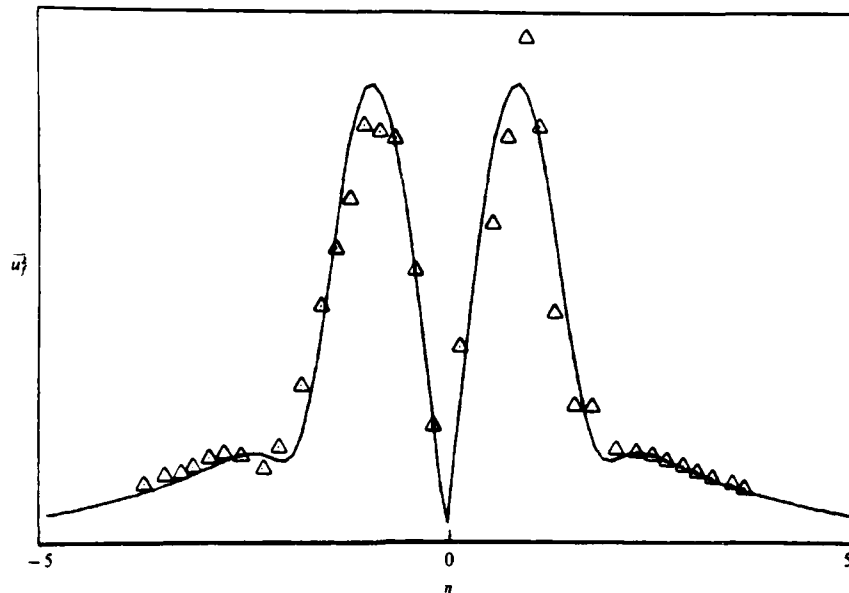


FIGURE 17. Amplitude distribution of u fluctuations phase locked to the external sinuous forcing signal. $\bar{x} = 400$.

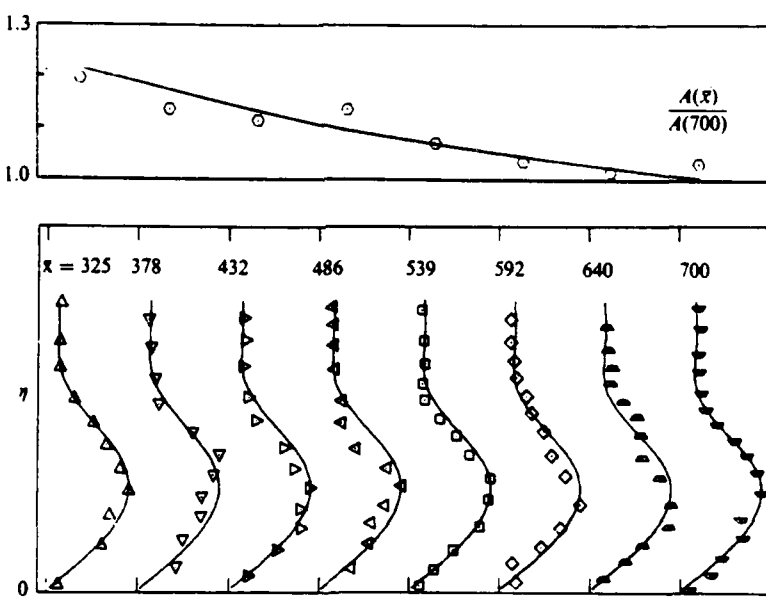


FIGURE 18. A comparison between the measured and predicted u perturbation amplitude distributions at several \bar{x} locations in a sinuously forced wake. A is not $A(x)$ of theory.

$\tilde{\phi}(x, y)$ were evaluated at each of the 51 streamwise locations. These functions, their derivatives with respect to both x - and y -coordinates, and the mean flow information were used to determine the correction term for slowly divergent flow $A(x)$ (equation (3.18)). Only the streamwise component of the velocity perturbation was measured and compared with the calculations.

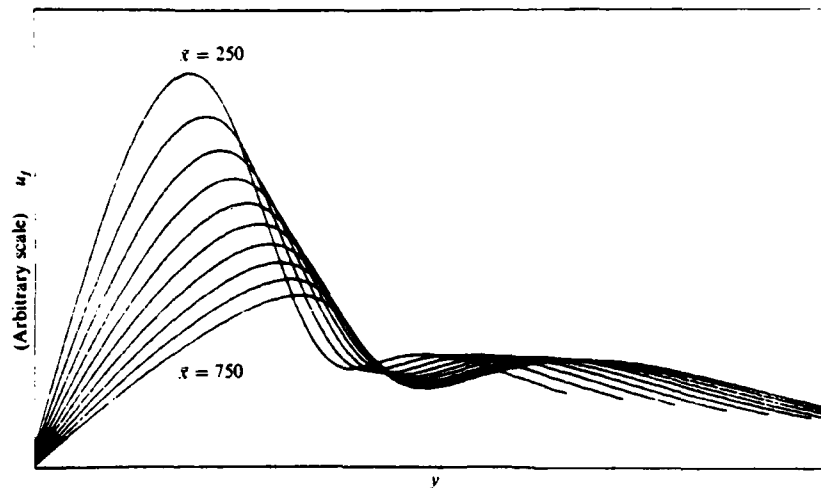


FIGURE 19. The variation of the computed eigenfunction with \bar{x} . $U_\infty = 7.4$ m/s; $\theta = 2.36$ mm; $f = 40$ Hz; $St = f\theta/U_\infty = 0.0128$.

A typical distribution of normalized amplitudes of the sinuous mode across the entire wake is shown in figure 17. The solid line represents computed values, while the triangles represent experimental results at $\bar{x} \sim 500$. The data were acquired by recording the velocity, together with the sinusoidal signal activating the flap. The velocity signal was phase-averaged over 300 cycles of the flap motion, and the Fourier transform of these average records provided the phase and amplitude estimates of the spectral elements of the velocity field, which were quite free from the random, turbulent fluctuations present in the original signals. There is little doubt that the artificially excited wavetrain can be described by an inviscid linear model, in spite of the fact that the flow is fully turbulent. One may note that the measured amplitude distribution in figure 17 is not exactly symmetrical about the centreline: the lack of symmetry is partly attributed to interference between the probe holder and traversing mechanism, to the large structures in the wake, and to the presence of the varicose mode.

A detailed comparison between the predicted amplitude distribution of the forced wave and measured amplitude profiles at eight streamwise locations is shown in figure 18. In the bottom part of this figure, the velocities were normalized by their respective maxima, which are replotted at the top. The computed maximum amplitude at $\bar{x} = 700$ was assigned the value of unity, which is the only floating constant in this comparison. The predicted and measured lateral distributions of amplitudes are in good agreement with one another, as is the decay of the maxima with increasing distance from the generator. It was surprising, at first, to note that the maximum amplitude of the forced wave actually diminished with \bar{x} , in spite of the fact that the quasi-parallel solutions based on (3.14) would predict amplification ($\alpha_t < 0$). The reasons for the apparent anomaly stems from the fact that α_t is a small negative number in the range of distances considered, and it is outweighed by the shape of the eigenfunction whose maximum amplitude diminishes with increasing \bar{x} (figure 19). A similar observation for an axisymmetric jet was made by Strange (1982). The value of the integral of the perturbation amplitude across the wake increases somewhat with increasing \bar{x} because the width of the wake increases. In fact, the product of the

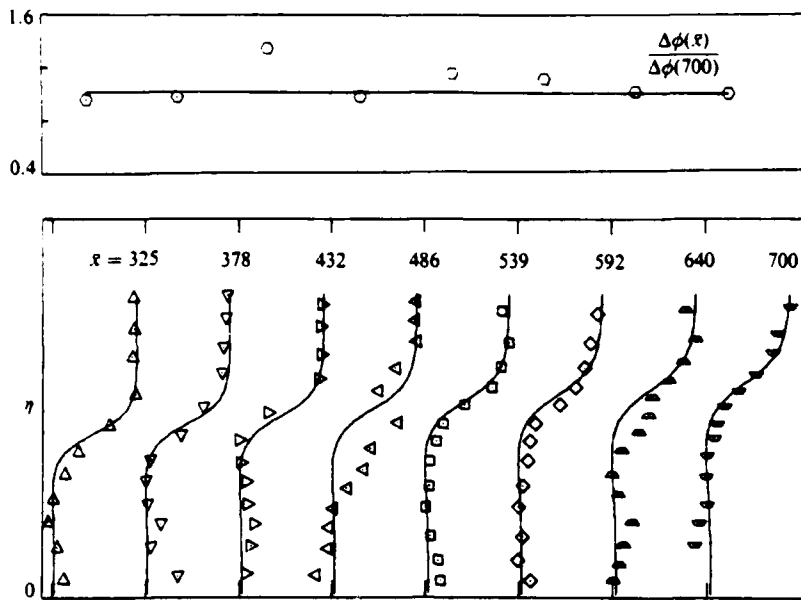


FIGURE 20. A comparison between measured and predicted phase distributions in a wake.

maximum amplitude and the local width is nearly constant between $\bar{x} = 325$ and $\bar{x} = 700$. This result could not have been predicted by the parallel flow approximation because it is sensitive to dL_0/dx and to u_0/U_∞ . The corresponding measured and computed phase profiles are shown in figure 20.

The amplification of a forced wavetrain in a turbulent, plane wake agrees in principle with similar observations made by Sato & Kuriki (1961) and Mattingly & Criminale (1972) for the growth of small disturbances in a laminar wake. In fact, only qualitative agreement was obtained by Mattingly & Criminale between experimental measurements and the predictions of the linearized spatial stability approach, while quantitative agreement is seen in the present case. Although improvements were made in both theory (inclusion of slow divergence) and experiment (forcing a sinuous mode), the type of agreement shown would not have been possible if the interaction between the imposed two-dimensional disturbances and the small-scale, three-dimensional turbulence in this flow was significant. Mattingly & Criminale attributed the discrepancies they observed to the inviscid assumption and to the neglected longitudinal gradients in the mean wake profiles; it seems to us that the inviscid assumptions can be retained as long as one considers waves which would have been growing spatially in parallel flow.

4.6. The amplification of natural disturbances in a plane, turbulent wake

Encouraged by a successful prediction of the propagation of imposed two-dimensional perturbations in this flow and intrigued by the shape of the broadband distribution of \bar{u}^2 in the wake, we proceeded to analyse the propagation of two-dimensional disturbances occurring naturally in a wake. In this case, the entire turbulent signal was Fourier analysed, instead of the phase-locked average considered in §4.5, and a particular spectral component corresponding to $f\theta/U_\infty = 1.3 \times 10^{-2}$ was examined in detail. The frequency chosen ($f = 40$ Hz at $U = 7.4$ m/s) corresponded approxi-

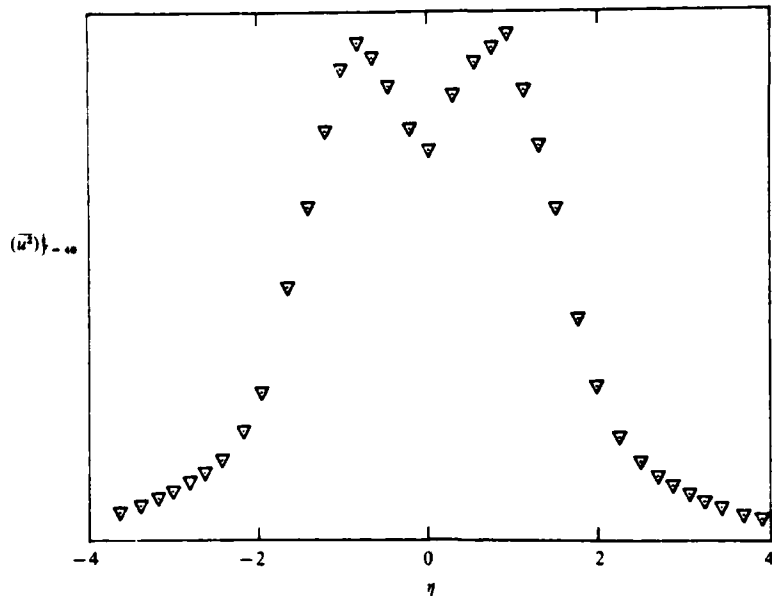


FIGURE 21. The amplitude distribution of the u component $f = 40$ Hz and $\bar{x} = 587$ in the unforced wake.

mately to the anticipated most-amplified sinuous mode in the range of \bar{x} considered. A typical profile of $(\bar{u}_f^2)^{1/2}$ in the wake of a flat plate corresponding to $\bar{x} = 587$ is shown in figure 21. The resulting lateral distribution of amplitudes of $(\bar{u}_f^2)^{1/2}$ is quite similar to the broadband distribution of u^2 shown in figure 7, although the ratio $[(\bar{u}_f^2)_{\text{CL}}/(\bar{u}_f^2)_{\text{max}}]$ is generally lower than the corresponding broadband distribution. Because the data are no longer phase locked, the actual amplitudes plotted are much larger than for the imposed wavetrain. Since the calculated amplitudes do not vanish on the centreline of the wake as predicted by the sinuous mode of inviscid amplification, another mechanism has to be considered. A hint was provided by the fact that the amplification rates ($-\alpha_i$) predicted on the basis of the parallel flow approximation were overwhelmed by the presence of longitudinal gradients in the mean flow (figure 17). It seems plausible that the same longitudinal mean flow gradients may have enhanced the relative importance of the varicose mode, which would contribute to the amplitude of the fluctuations on the centreline; otherwise, nonlinear effects and secondary instabilities may have to be considered.

The calculation procedure outlined in §4.4 was repeated for $f\theta/U_\infty = 1.3 \sim 10^{-2}$ and the appropriate mean flow parameters (table 2). The calculations were done twice: once for the sinuous motion, then a second time for the varicose mode. By assuming that, to the first order of approximation, one may simply superimpose the amplitudes of the individual modes of instability, neglecting any correlation between them, the resulting amplitudes were calculated. For the purpose of comparison between computations and experiment, it was assumed that the initial amplitudes resulting from both modes are equally important; namely, that the maximum amplitude of the varicose mode is equal to the maximum amplitude of the sinuous mode at some initial \bar{x} -distance from the generator. The results of these calculations are plotted in figure 22 for $370 \leq \bar{x} \leq 640$; the symbols in the figure represent data calculated from experimental results and filtered at $f\theta/U_\infty = 1.3 \sim 10^{-2}$. There is a qualitative

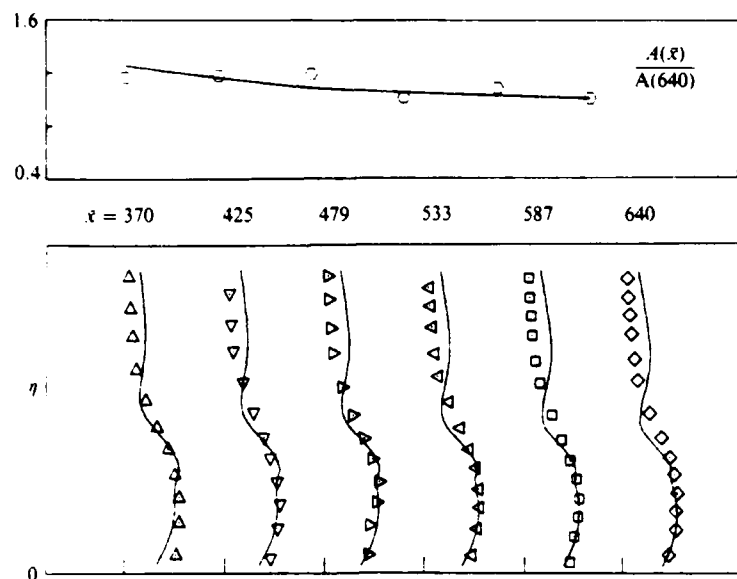


FIGURE 22. A comparison between measured and predicted u amplitude distributions at several \bar{x} locations in an unforced wake. A is not $A(x)$ of theory.



FIGURE 23. Large coherent structures photographed in the wake of the flat plate with no forcing. $\bar{x} \approx 500$ and $Re_h = 600$.

agreement between the predicted and measured lateral distributions of the \bar{u}_f^2 amplitudes, indicating that both modes of instability are probably present and can give rise to the peculiar profile of the u fluctuations in the wake. The agreement between theory and experiment in this case is not as good as for the forced sinuous wave, suggesting that either the two-dimensional approximation is invalid or the simple linear superposition neglecting the phase relation between both modes is inadequate. Another possible error stems from the nonlinear terms neglected in the present context.

In order to explore further the importance of the interaction between the two modes of instability, we resorted to flow visualization using a smoke wire. The wire was

positioned at $\bar{x} = 350$, while the camera was located at $\bar{x} = 500$. The smoke patterns were photographed at $U_x = 3.4$ m/s (corresponding to $Re_\theta = 600$), rather than at $U_x = 7.45$ m/s to enhance the quality of the results. The smoke wire did not work well at the higher velocity. Although θ is approximately 20° higher for the lower Reynolds number, this case is representative for the larger Reynolds number case ($Re_\theta = 1035$) as the large-scale turbulence should be relatively insensitive to the Reynolds number change used here. Large coherent structures are clearly visible in the wake of the flat plate (figure 23), even in the absence of any imposed oscillations. These structures are similar in appearance to the Karman vortex street because they seem to be comprised of vortices of alternating sign of vorticity, which are placed in a staggered manner on both sides of the wake centreline. Therefore, neither the varicose mode, which requires that the vortices appear in pairs distributed symmetrically about the centreline, nor the sinuous mode, which requires vortices whose centre coincides with the centreline, dominate this flow. Although the vortices are large and coherent and have a prevailing wavelength, λ_p , of approximately 10 cm, there is sufficient irregularity in their shape, size, and position to cause the spectrum of the induced fluctuation at the edge of the wake to be fairly broad (figure 13). The introduction of periodic forcing did not have a significant effect on the shape and scales of the large eddies visualized in this manner. For the unforced case, the flow-visualization results indicate that $\lambda_p/L_0 \sim 3$ for $Re_\theta = 600$. The theoretically most-amplified wave can be determined from figure 14 to have a frequency of 75 Hz corresponding to a wavelength of 9.9 cm for the higher velocity, $Re_\theta = 1035$, case. If one assumes that the normalized mean velocity profile is the same for both Reynolds number cases, the frequency of the most-amplified wave would scale with U_x , and therefore, the wavelength remains constant as $\lambda = c/f = U_x/f$. To determine L_0 for the $Re_\theta = 600$ case, we assumed L_0/θ is independent of Reynolds number in the turbulent range considered. Then, using the measured results for $Re_\theta = 1035$ (table 2), L_0 for the lower Reynolds number flow visualization case could be determined. The theoretical prediction for $Re_\theta = 600$ is $\lambda_p/L_0 = 3.5$, which is in good agreement with the flow-visualization results. Since the energy-containing eddies have a scale of the order of L_0 to $2L_0$, the wavelength of the most-amplified wave from linear stability theory is one to two times larger than the energy-containing scales of the turbulence.

The degree of two-dimensionality of these structures was first estimated by placing the smoke wire parallel to the circular cylinder but displacing it from the generator in the lateral direction in order that the smoke would not be entrained by the wake before $\bar{x} = 300$. The resulting photo (figure 24) indicates that the large eddies have a tendency to be two-dimensional, although the two-dimensionality is by no means perfect. There appears to be a variation of amplitudes along the span of the wake, as well as phase irregularities.

Coherence spectra calculated from u fluctuations sensed by two probes separated in the spanwise direction provide a quantitative measure of the two-dimensionality of the various scales. The two-point, cross-correlation function for stationary random variables $u_i(\mathbf{x}, t)$ and $u_j(\mathbf{x} + \mathbf{r}, t + \tau)$ is defined as

$$R_{ij}(\mathbf{x}, \mathbf{r}, \tau) = \overline{u_i(\mathbf{x}, t) u_j(\mathbf{x} + \mathbf{r}, t + \tau)}. \quad (4.9)$$

and the cross-spectrum.

$$\phi_{ij}(\mathbf{x}, \mathbf{r}; f) = \frac{1}{2\pi} \int_{-\infty}^{\infty} R_{ij}(\mathbf{x}, \mathbf{r}; \tau) e^{i2\pi f \tau} d\tau = C_{ij}(\mathbf{r}, \mathbf{x}; f) - iQ_{ij}(\mathbf{x}, \mathbf{r}; f) \quad (4.10)$$

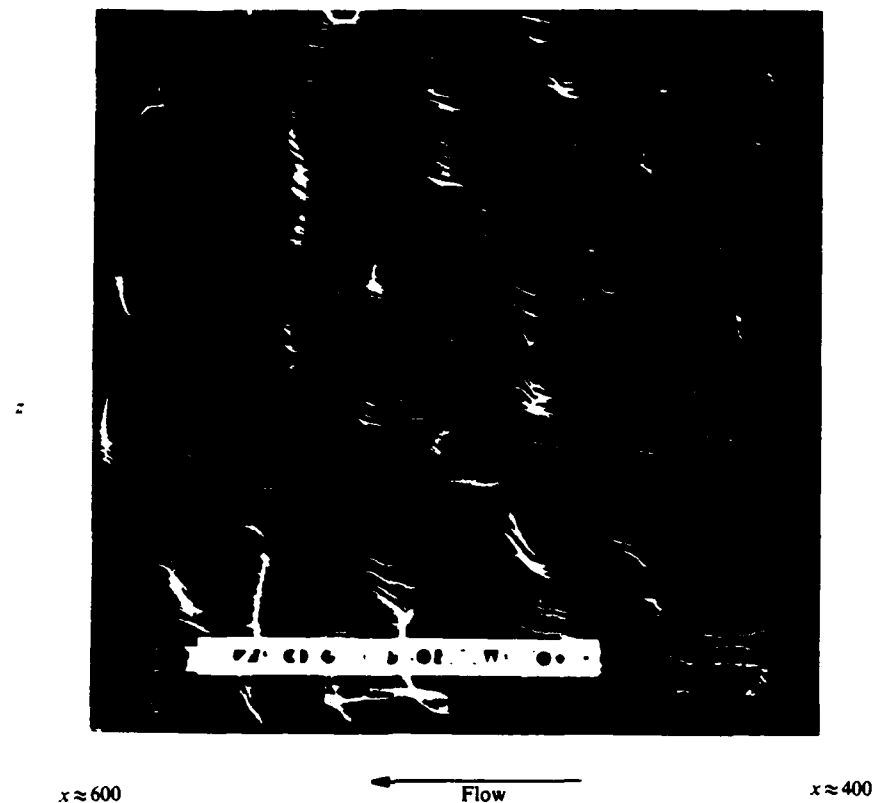


FIGURE 24. The spanwise coherence of the large eddies in the wake of a circular cylinder at $\bar{x} \approx 600$ and $Re_h = 600$.

where C_{ij} is called the cospectrum and Q_{ij} , the quadrature spectrum. The coherence spectrum is defined as

$$\text{Coh}_{ij}(\mathbf{x}, \mathbf{r}; f) = \frac{C_{ij}^2(\mathbf{x}, \mathbf{r}; f) + Q_{ij}^2(\mathbf{x}, \mathbf{r}; f)}{F_{ii}(\mathbf{x}; f) F_{jj}(\mathbf{x} + \mathbf{r}; f)}, \quad (4.11)$$

where $F_{ii}(\mathbf{x}; f)$ and $F_{jj}(\mathbf{x} + \mathbf{r}; f)$ are the familiar (one-point) energy spectra, i.e.

$$\bar{u}_i^2(\mathbf{x}) = \int_{-\infty}^{\infty} F_{ii}(\mathbf{x}; f) df. \quad (4.12)$$

The phase angle θ_{ij} can be obtained as

$$\theta_{ij}(\mathbf{x}, \mathbf{r}; f) = \tan^{-1} \left[\frac{Q_{ij}}{C_{ij}} \right]. \quad (4.13)$$

The coherence spectrum is bounded, and its value must be between 0 and 1. We will consider the component $\text{Coh}_{11}(\mathbf{x}, \Delta z; f)$, which represents the degree of spatial correlation between the Fourier components of $u_1(\mathbf{x}, t)$ and $u_1(\mathbf{x} + \mathbf{k}\Delta z, t + \tau)$ at the same frequency, where \mathbf{k} is a unit vector in the z - or spanwise-direction.

A spanwise rake containing six hot-wire probes spaced from 1.1 to 2.54 cm apart was used for the coherence data. Measurements were taken in the wake of the flat plate, with and without excitation, at $\bar{x} = 430$ and 646, with the rake located at $\eta = 0$.

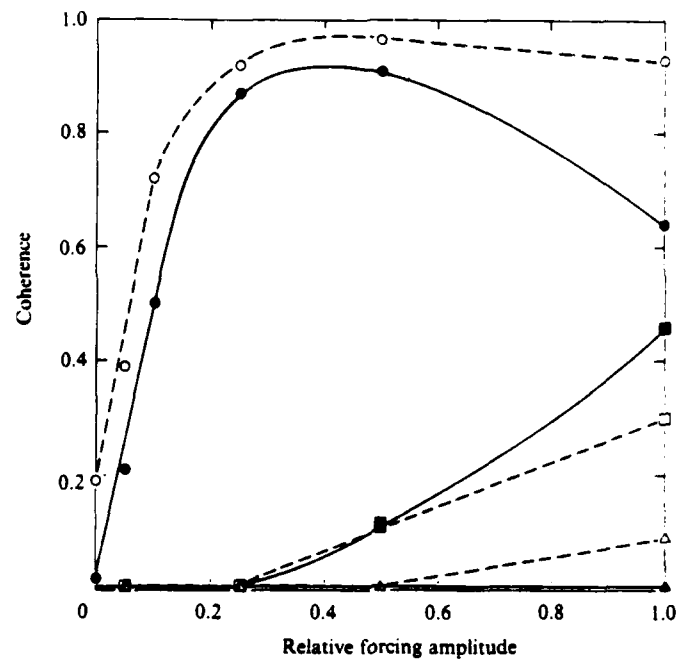


FIGURE 25. The response of the wake to various sinuous forcing levels. $\bar{x} = 646$ and $\eta = 0.6$. ●, $f = 50$ Hz, $\Delta z/L_0 = 10$; ○, $f = 50$ Hz, $\Delta z/L_0 = 0.4$; ■, $f = 100$ Hz, $\Delta z/L_0 = 10$; □, $f = 100$ Hz, $\Delta z/L_0 = 0.4$; ▲, $f = 150$ Hz, $\Delta z/L_0 = 10$; △, $f = 150$ Hz, $\Delta z/L_0 = 0.4$.

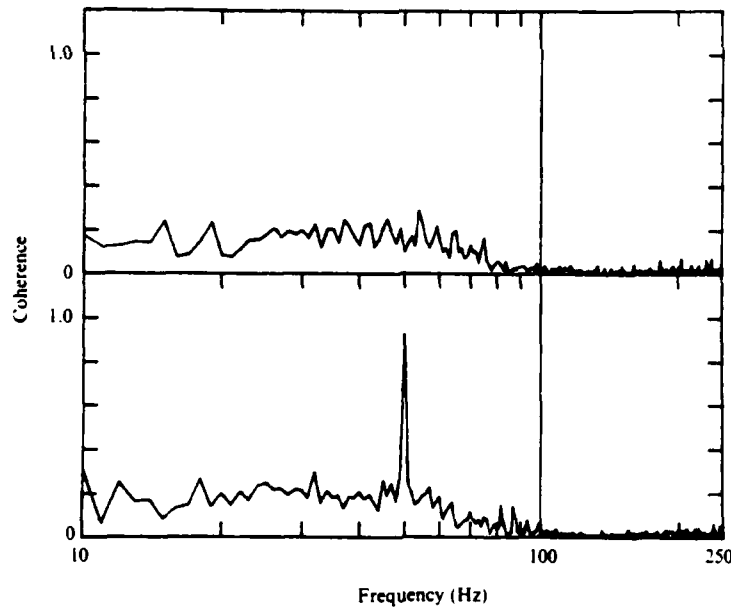


FIGURE 26. Coherence spectra measured at $\bar{x} = 646$, $\eta = 0.6$, and $\Delta z/L_0 = 0.4$ in the wake of the flat plate. Upper trace without forcing. Lower trace with forcing at 50 Hz.

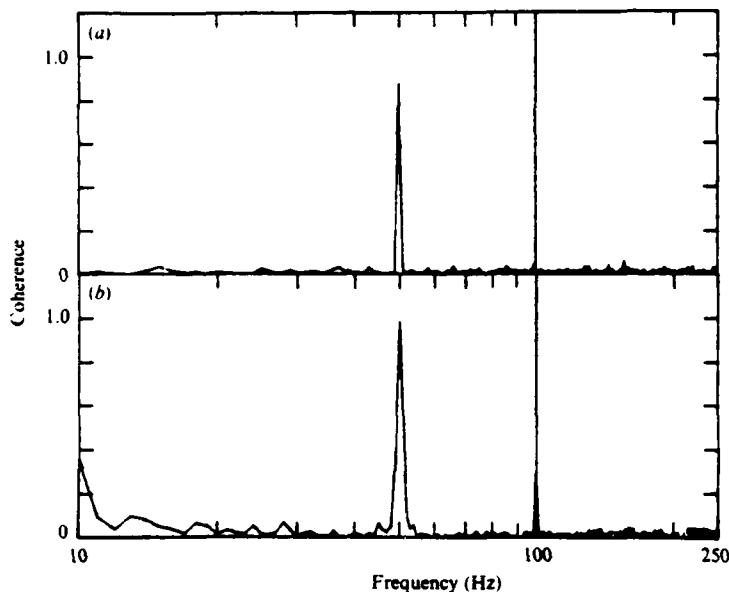


FIGURE 27. (a) Coherence spectrum measured at $\bar{x} = 646$, $\eta = 0.6$, and $\Delta z/L_0 = 10$, with forcing at 50 Hz. (b) Same as (a) except $\eta = 3$.

0.6, and 3. The lateral position $\eta = 0.6$ approximately corresponds to the location at which u -fluctuations are most energetic. The response of the wake at $\bar{x} = 646$ and $\eta = 0.6$ to various levels of excitation is shown in figure 25 for two Δz spacings, 1.1 and 25.4 cm apart. The values of the coherence at the excitation frequency (50.0 Hz) and its first and second harmonics as a function of amplitude are presented. All amplitudes are scaled by the highest amplitude of oscillation. Where the relative forcing amplitude was less than 0.25, the coherence spectrum responded in a linear manner. For amplitudes in the range of 0.25 to 0.5, the value of the coherence at the forcing frequency is nearly independent of Δz in the range investigated, at least up to $\Delta z/L_0 = 10$. The relative amount of energy tied up with the forcing frequency can be determined from the spectrum of the velocity fluctuations. In the case, the spectral peak at 50 Hz was one order of magnitude above the 'background' turbulent fluctuations.

Figure 26 shows the coherence spectra measured at $\bar{x} = 646$, $\eta = 0.6$, and $\Delta z/L_0 = 0.4$, with and without forcing. The forcing frequency was 50 Hz, corresponding to the expected predominant frequency at this \bar{x} , and the relative amplitude of forcing was 0.25. The effect of forcing sharply enhances the value of the coherence at the forcing frequency to 0.92, with little effect on the rest of the spectrum. The corresponding data for $\Delta z/L_0 = 10$ are shown in figure 27(a), where only the data for the forced case are presented. The coherence for the unforced case at this separation vanished at all frequencies. For the forced case, the entire correlation is contained in the spectral spike at 50 Hz, for which the coherence is 0.87. Similar results were obtained at forcing levels as low as 0.05, where the peak correlation was 0.21 and 50 Hz. At $\eta = 3$ (figure 27b), a much higher coherence at the forcing frequency was measured (0.98), indicating that the large structure in the wake must be highly two-dimensional to generate such a result for the large spanwise separation, $\Delta z/L_0 = 10$. For the unforced case, the coherence is nearly zero from 10 to 260 Hz.

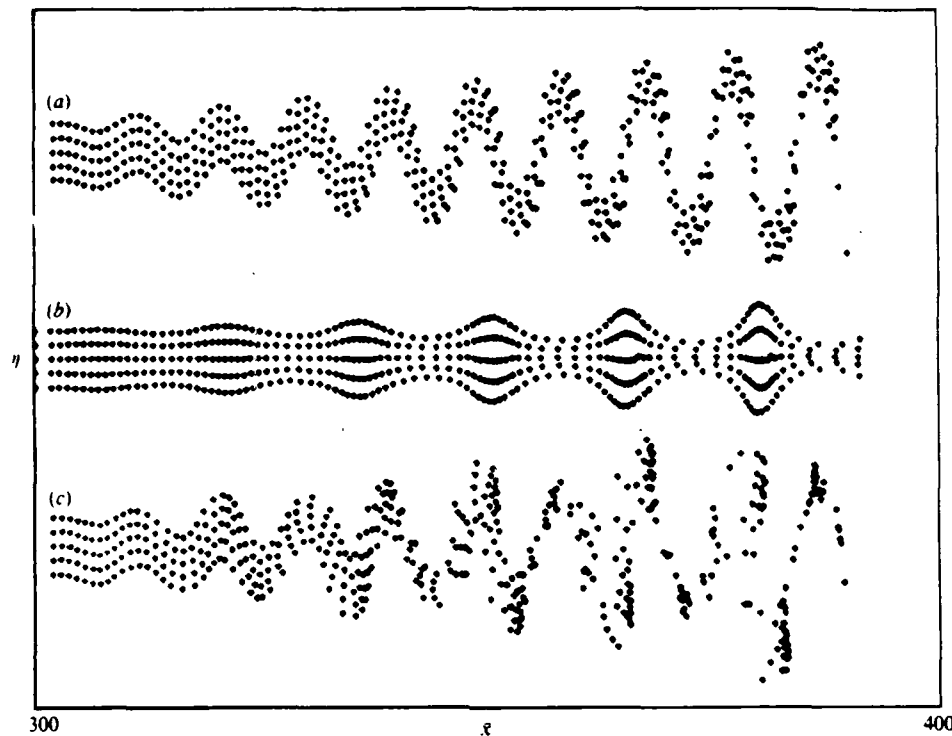


FIGURE 28. Streak-lines computed assuming spatial instability of parallel flow at $\bar{x} = 300$: (a) sinuous, most-amplified mode; (b) varicose, most-amplified mode; (c) combined modes.

The results indicate that a slight amount of forcing generates a strong two-dimensional wave in the wake at the forcing frequency.

Is the proposed model capable of explaining the large structures observed in figure 23? For this purpose, some streak-lines had to be calculated. Since the calculations were aimed at a qualitative understanding of this phenomenon, a parallel flow approximation was invoked locally. It was assumed that the particles were uniformly released at $\bar{x} = 300$, where $u_0/U_\infty = 0.06$. The prevailing wavelength from figure 23 was used to determine β corresponding to the spatially most-amplified sinuous wavetrain in this mean flow. Both u and v components of the perturbation velocity were calculated across the entire wake, and the corresponding particle paths were established from the equations

$$\frac{dx}{dt} = U[x(t), y(t), t]; \quad \frac{dy}{dt} = V[x(t), y(t), t]. \quad (4.14)$$

(For a detailed description of the procedure, see Michalke 1965.) The initial amplitude of the u -component of the velocity perturbations was $0.025 U_\infty$. This corresponds to 30% of u_0 , which is a constant in these calculations.

Five of the streak-lines calculated taking only the sinuous mode into consideration are shown in figure 28(a). The streak-lines have a sinusoidal pattern undulating about the centreline of the wake. The amplitude of the undulations increases with increasing distance from the source; at large distances, most of the particles congregate at the outer edge of the wake.

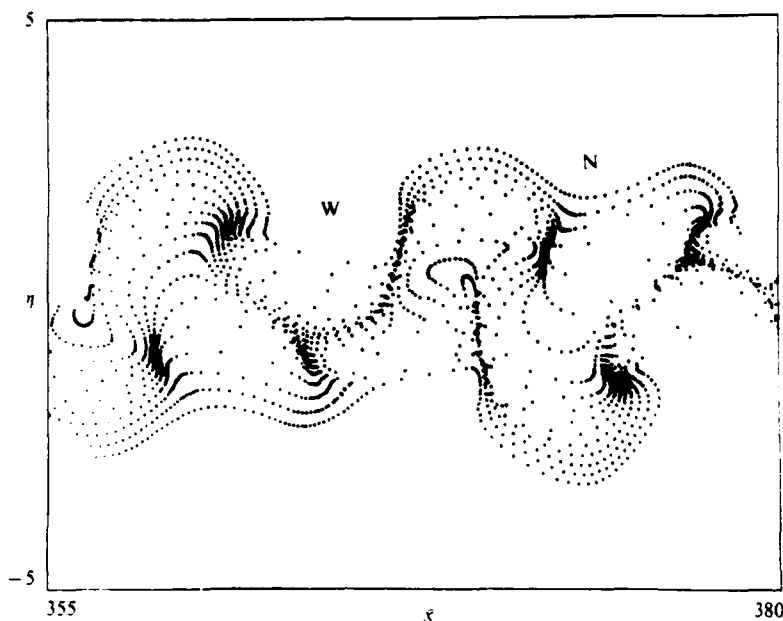


FIGURE 29. Streak-lines from figure 28(c) plotted on larger scale to show staggered nature of particle congregation.

The corresponding, most strongly amplified varicose mode has a perturbation frequency equal to $\frac{1}{3}$ of the frequency of the prevailing sinuous mode (not quite a subharmonic frequency). The computed streak-lines for the varicose mode are shown in figure 28(b). The particles in this figure congregate in lumps, which are symmetrical about the centreline of the wake. The streak-lines shown in figure 28(a) or (b) bear *no resemblance* to the observed coherent structures seen in figure 23.

The streak-lines shown in figure 28(c) represent the combined motion of both modes of instability when the coefficient of the velocity perturbation is still maintained at 0.025. The initial ratio between the amplitudes of u and v in the varicose mode and the sinuous mode was 0.7. (This number simply appeared because the eigenfunctions were not normalized: changing the initial ratio by a factor of two made no substantial difference in the pattern.) The initial phase relation between the modes was assumed to be zero. (Changing this number also had no effect on the basic pattern at some distance downstream from the source location.) The phase velocities of the two modes are not equal and differ by a few per cent.

The prevailing wavelength of the streak-lines (figure 28c) still corresponds to the prevailing wavelength of the sinuous mode, but the presence of the varicose mode not only modulates the streak-lines but also contributes to an apparent chaotic behaviour. Most important is the fact that these streak-lines, when replotted on a larger scale, resemble the pattern observed in the smoke photographs (figure 23). Namely, the particles congregate in a staggered manner about the centreline and the large eddies are, at times, separated by deep incursions of 'potential' fluid. Sometimes, these incursions are narrow (marked by the letter 'N' in figure 29) and, sometimes, they are wide (marked by 'W'). It therefore transpires that only the combination of both modes can successfully describe the flow.

The distributions of vorticity for the three cases considered in figure 28 were

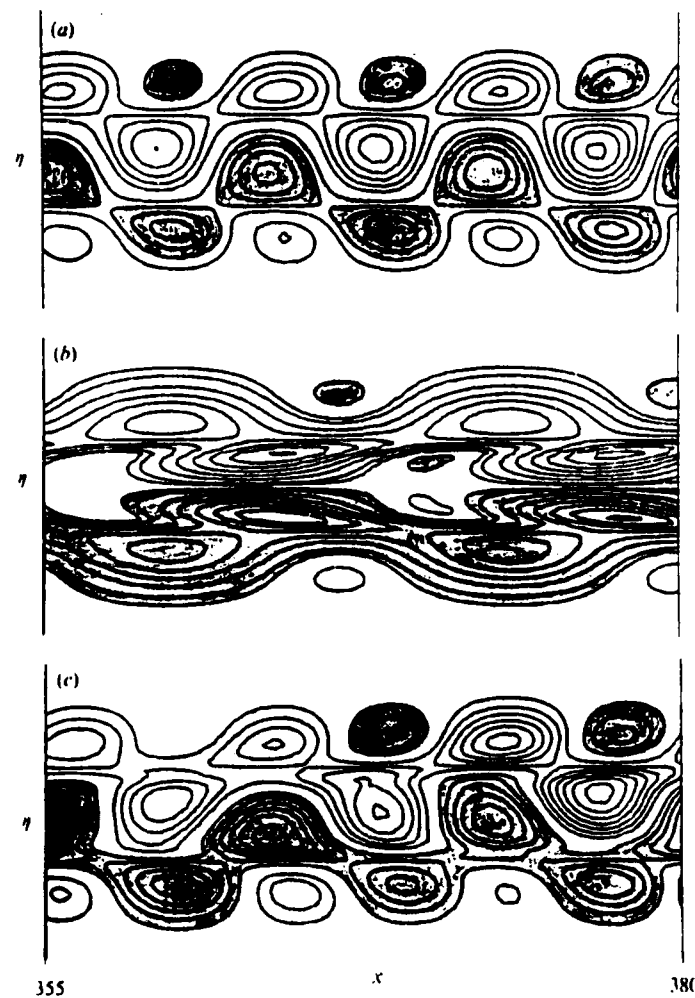


FIGURE 30. Vorticity perturbation contours computed for the three cases of streak-lines shown in figure 28: (a) sinuous, most-amplified mode; (b) varicose, most-amplified mode; (c) combined modes.

calculated directly from the eigenfunctions solved, because the vorticity perturbation

$$\omega(y) = -\frac{U''}{U - \beta/x} \phi. \quad (4.15)$$

and the total vorticity

$$\Omega(x, y, t) = -U + 0.015 RP \{ \omega(y) \exp [i(\alpha x - \beta t)] \}. \quad (4.16)$$

which is, of course, periodic in time. The vorticity contours plotted in figure 30 were calculated for $t = 2\pi/\beta$ and for $355 \leq \bar{x} \leq 385$, as in figure 29. (The shaded regions

correspond to negative vorticity.) By neglecting either the varicose mode [figure 30a] or the sinuous mode [figure 30b], the resulting vorticity contours appear to be very regular. The contours are either symmetrical or antisymmetrical about the centreline and indicate intensification of vorticity with increasing \bar{x} . The vorticity contours resulting from the combined two modes of instability [figure 30c] are surprisingly similar to the contours produced by the sinuous mode alone. One may notice, however, that the intensity of the contours in figure 30c are modulated by the varicose mode, even if they are not severely distorted by the addition of this mode. A simple superposition of figure 30c on figure 28 leads to the conclusion that a congregation of particles observed in a *still photograph* does not necessarily correspond to a concentration of vorticity.

5. Discussion

The velocity and length scales in a plane, turbulent, and supposedly self-preserving wake are dependent on inflow conditions and, therefore, on the shape and size of the obstacle generating the wake. We could not prove that these scales will not become universal functions of (x/θ) at extremely large values of (x/θ) , but the distances at which this may (or may not) occur may be so large as to have no practical impact on the problem. The range of x/θ values in the present study extended up to 2000, corresponding to $u_0/U \sim 0.03$. The dependence of the plane mixing layer on inflow conditions was observed some years ago (Champagne, Pao & Wygnanski, 1976) and traced to the presence of large coherent structures (Oster & Wygnanski 1982). The existence of large coherent structures in a wake, however, was often confused with vortex shedding, which was so ably discussed by Karman (1912) in the lee of a circular cylinder at low Reynolds numbers. The large eddies proposed by Townsend (1956) and Grant (1958) bear little resemblance to the structures observed presently, although Townsend suggested that the large eddies present in fully turbulent free shear flows might have been generated by hydrodynamic instability of the mean flow.

What is the cause for the apparent dependence of the small-deficit wake on the shape of the generator? The nature of the flow in the vicinity of the generator, including any vortices shed by the generator, can provide a plausible explanation for this phenomenon. The frequency, amplitude, and the predominant mode of the initial perturbation vary from one geometry to another. For all geometries investigated, the *predominant* mode of shedding was sinuous, but the presence of the varicose mode was also detected in the vicinity of the low-solidity screens and circular cylinder. The strongest sinuous oscillations were observed downstream of the thick symmetrical airfoil because the initiation of separation from one surface changed the circulation around the airfoil, moving the front stagnation point toward the separated surface and therefore initiating a separation from the opposite surface. The amplitude at the shedding frequency was three orders of magnitude stronger than the background turbulence. The amplitudes of the oscillations generated by a circular cylinder and by the screens were approximately two orders of magnitude above the background, while the amplitude of the oscillations downstream of the solid strip held normal to the flow was of the same order of magnitude as the background.

It is also suspected that the lower the frequency of the shedding, the more persistent the initial effects will be: in fact, the frequency of shedding downstream of the symmetrical airfoil of a given thickness depends on the chord length, provided the flow separates upstream of the trailing edge. The effects of frequency, however, appear to be less significant than the effects of amplitude. A detailed investigation

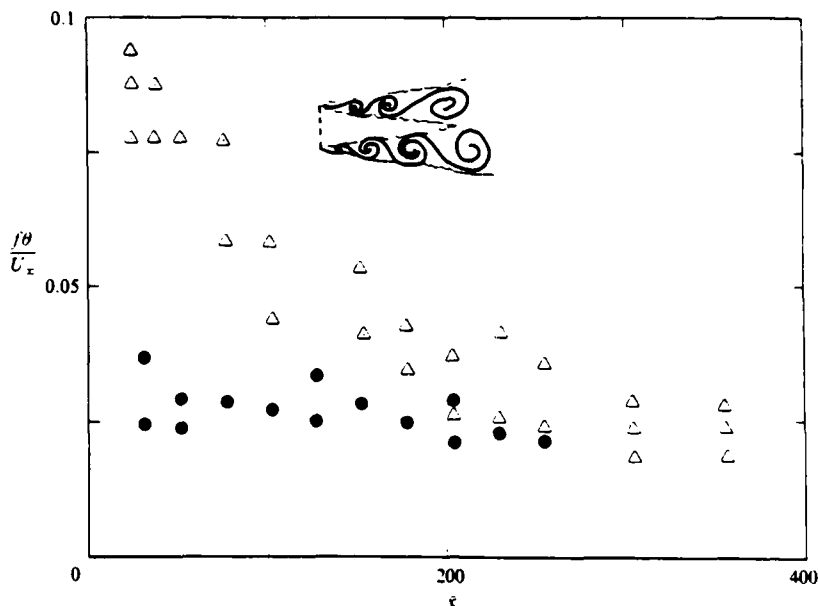


FIGURE 31. The measured predominant frequencies in the wake of: (a) ●, a circular $\frac{1}{6}$ in. cylinder, $Re_d = 2000$; (b) △, the 30% solidity screen, $Re_d = 2000$.

of the near wake has been undertaken in order to determine the effects of inflow condition more precisely.

Cimbala *et al.* (1981) observed, with the aid of a smoke wire, the evolution of large coherent structures in a wake of a circular cylinder up to $Re_d < 2000$ and in a wake of two screens at comparable Re . These structures became apparent some 200 diameters downstream of the cylinder and had a regular frequency two to three times lower than the Strouhal frequency. They were unable, however, to corroborate their results with spectral measurements for their high-Reynolds-number case and attributed it to the high turbulence level in their tunnel. Some measurements of spectra at the outer edge of the wake were carried out for two wake generators: (i) a circular cylinder at $Re_d = 2500$ corresponding to $Re_d = 5000$ and (ii) a screen having 45% solidity, also at $Re_d = 2500$. In the immediate neighbourhood of the cylinder, the predominant spectral peak (not shown) corresponded to the shedding frequency of the cylinder, i.e. at $St_d = 0.206$ or $St_d = 0.10$. At $\bar{x} > 50$, the predominant spectral peak dropped quite abruptly to $St_d \approx 0.03$. Thereafter, the evolution of the spectral peak was rather slow and is hardly detectable on the scale shown in figure 31. The spectral peaks associated with the screen tailored to produce the same momentum thickness as the circular cylinder are similar to those mentioned above at $\bar{x} > 250$. The big difference between the two flows occurs at $50 < \bar{x} < 250$, where the characteristic frequency of the spectral peaks generated by the screen decreases slowly with \bar{x} . At $\bar{x} > 150$, one may detect the appearance of an additional peak in the spectrum, which roughly corresponds to the spectral peak in the far wake of the circular cylinder; this peak amplifies quickly and dominates the spectrum at $\bar{x} > 200$. It seems that the coherent structures in the near wake of this particular screen retain some of their characteristics up to $\bar{x} = 250$, while in the wake of the circular cylinder, this transition is accomplished at $\bar{x} = 50$. It is believed that the shear layers generated in the wake of the screen (see insert in figure 31) undergo an instability process

reminiscent of the plane mixing layer (Gaster *et al.* 1985), generating eddies whose characteristic frequency decreases in the direction of streaming. Whether these eddies grow by entraining fluid from the surrounding stream or by a process of amalgamation remains to be seen.

Since Cimbala *et al.* (1981) did not observe any vortex amalgamation in their visualization experiments, one would be inclined to think that the gradual decrease in the characteristic frequency stemming from an increase in the wavelength of these eddies is caused by entrainment. In any event, once the scale of these eddies becomes comparable to the width of the screen, an interaction between two shear layers of opposing vorticity has to occur before the wake will become 'fully developed'. It is possible that a phase accommodation ensues, resulting in a slow evolution of the typical large structures existing in the self-preserving region. The evolution of the fully developed wake is currently being investigated, but the importance of initial conditions is evident in figure 31.

The mutual interaction between the large coherent structures and the mean flow is outside the scope of the linear stability theory. However, the dependence of the mean flow field on the initial conditions, and consequently on the large coherent structures, poses precisely such a problem. The notion that the free-stream turbulence and the shape of the generator may have an effect on the development of a self-preserving wake was proposed by Symes & Fink (1977). These authors observed that the wake generated by a rectangular cylinder did not evolve in the same manner as the wake generated by a circular cylinder, but the most important observation stems from the fact that the evolution of the wake was sensitive to grid turbulence, whose integral scale was an order of magnitude larger than the scale of the generator. This suggested that the externally imposed turbulence interacted with the flow far downstream, where the typical scales in the wake and in the free stream became comparable. It also implied that an instability mechanism might be responsible for this result. The present investigation confirmed this notion, although nonlinear terms have to be considered in order to assess the interaction between the mean flow and the imposed oscillation. Perhaps, an integral approach similar to the one used by Ko, Kubota & Lees (1970) might predict such an interaction through the Reynolds stress. The concept of flow equilibrium and self-preservation has to be carefully reconsidered in view of the present findings, in spite of the fact that the normalized shape of the mean velocity profile was not affected. The dependence of the lateral distribution of the turbulent intensities on the nature of the generator (figure 7) and the relatively poor collapse of the dimensionless data onto a single function for a given wake generator raise the possibility that the flow is not in equilibrium. Although this possibility was considered remote at the start of this investigation, a plot showing the difference between the maximum intensity $(\bar{u}^2)_{\max}$ and the intensity on the centreline of the wake $(\bar{u}^2)_{CL}$ normalized by u_0^2 is shown in figure 32 for the wake of the flat plate. If the flow was in perfect equilibrium, then $(\bar{u}^2)_{\max} - (\bar{u}^2)_{CL}/u_0^2$ should have been constant at all \bar{x} . Although this plot is very susceptible to experimental inaccuracies and should be treated with due caution, the lack of constancy might have been caused by a nonlinear interaction between the varicose mode and the sinuous mode of instability. The possible interaction between the two modes will be investigated in detail by forcing the wake simultaneously with a combination of modes.

The assumption of parallel flow (3.2) makes the eigenfunction $\phi(y)$ and the eigenvalues α and β invariant with respect to streamwise distance from the generator. Thus, for $\beta = 0$ (i.e. spatially amplified waves), only a single mode containing the

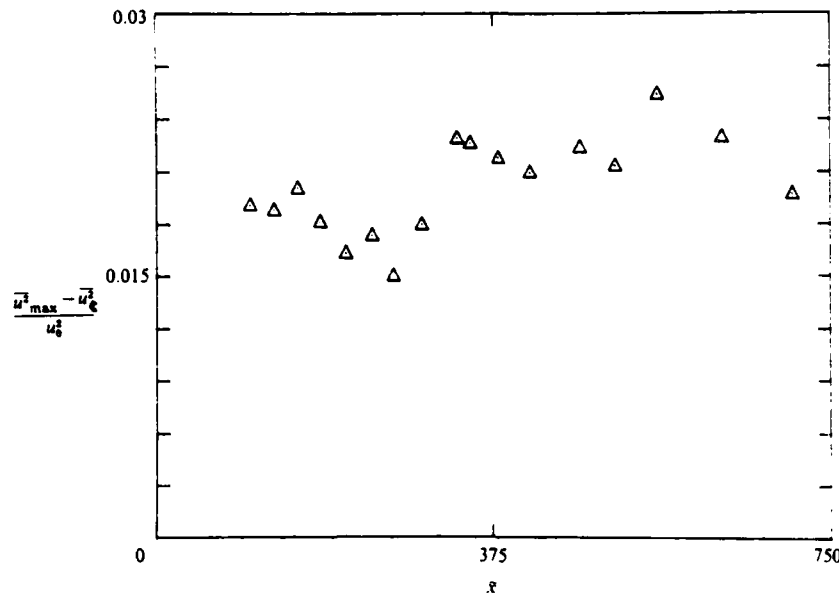


FIGURE 32. The variation of turbulent intensity defect on the centreline of the wake of a flat plate.

largest $|-z_i|$ need be considered. However, the amplification rates in the small-deficit, plane wake are so small that one cannot disregard one mode of instability in favour of another simply because its $|-z_i|$ is the largest. The long distances required for an unstable wave to amplify increase the relative significance of the longitudinal gradients in the mean velocity. By neglecting the varicose mode in favour of the sinuous one, Sato & Kuriki (1961) had to resort to nonlinear effects in their attempt to explain the cause for the generation of two rows of vortices. Mattingly & Criminale (1972) offered an alternate explanation, which is based on the vorticity distribution of the sinuous mode being superposed on the mean vorticity. The generation of a vortex structure reminiscent of a Karman vortex street can quite easily be attributed to the superposition of the two instability modes, keeping in mind that the most unstable frequency of the varicose mode is only slightly higher than a subharmonic of the most unstable sinuous mode. Sinuous forcing of the flow has little effect on the shape of the large eddies visualized by smoke until the amplitude of the forcing becomes high. In this case, the smoke pattern is more regular and the eddies are located closer to the centreline than in the corresponding unforced wake.

6. Conclusions

It was experimentally observed that the characteristic velocity and length scales, u_0 and L_0 , when suitably scaled by the momentum thickness and the free-stream velocity, do not exhibit universal behaviour and do depend on the inflow conditions and therefore on the geometry of the wake generator. The mean velocity profiles for each wake, when normalized by their own velocity and length scales, are self-preserving and are also identical for all wake generators. The distributions of the turbulence intensities normalized in the same manner are almost self-preserving, but they are dependent on the geometry of the wake generator.

Linear inviscid stability theory, in which the divergence of the mean flow was taken into account, predicts quite well the amplification and the transverse distributions of amplitudes and phases of externally imposed sinuous waves in a fully developed turbulent wake generated by a flat plate. It appears that the large, coherent, vortex structures occurring naturally in a wake can be modelled to some extent by linear stability theory. Furthermore, the interaction of the two possible modes of instability may be responsible for the apparent Karman vortex street-type of structures observed visually in the small-deficit, turbulent wake.

The project was supported by the Air Force Office of Scientific Research under Contract No. F49620-79-C-0224. I. Wygnanski would like to express his thanks to AFOSR for providing the opportunity for him to devote his entire sabbatical stay to this project. The authors would like to thank Dr M. Gaster, who provided the initial impetus for the theoretical approach.

REFERENCES

BOUTHIER, M. 1972 *J. Méc.* **11**, 599.
BROWN, G. L. & ROSHKO, A. 1974 *J. Fluid Mech.* **64**, 775.
CHAMPAGNE, F. H. 1978 *J. Fluid Mech.* **86**, 67.
CHAMPAGNE, F. H., PAO, Y. H. & WYGNANSKI, I. J. 1976 *J. Fluid Mech.* **74**, 209.
CIMBALA, J., NAGIB, H. & ROSHKO, A. 1981 *Bull. Am. Phys. Soc.* Ser. **11**, 2.
CRIGHTON, D. G. & GASTER, M. 1976 *J. Fluid Mech.* **77**, 297.
FREYMUTH, P. 1966 *J. Fluid Mech.* **25**, 683.
GASTER, M., KIT, E. & WYGNANSKI, I. 1985 *J. Fluid Mech.* **150**, 23.
GRANT, H. L. 1958 *J. Fluid Mech.* **4**, 149.
KARMAN, TH. v. 1912 *Nachr. Ges. Wiss. Göttingen* 547.
KO, D. R. S., KUBOTA, T. & LEES, L. 1970 *J. Fluid Mech.* **40**, 315.
MARASLI, B. 1983 Master's thesis, AME Dept., University of Arizona.
MATTINGLY, G. E. & CRIMINALE, W. O. 1972 *J. Fluid Mech.* **51**, 233.
MICHALKE, A. 1965 *J. Fluid Mech.* **23**, 521.
NARASIMHA, R. & PRABHU, A. 1972 *J. Fluid Mech.* **54**, 1.
OSTER, D. & WYGNANSKI, I. 1982 *J. Fluid Mech.* **123**, 91.
SATO, H. & KURIKI, K. 1961 *J. Fluid Mech.* **11**, 321.
SREENIVASAN, K. R. 1981 *AIAA J.* **19**, 1365.
SREENIVASAN, K. R. & NARASIMHA, R. 1982 *Trans. ASME J. Fluids Engng* **104**, 167.
STRANGE, P. J. R. 1982 Ph.D. thesis, University of Leeds.
SYMES, C. R. & FINK, L. E. 1977 In *Structures and Mechanisms of Turbulence I*, proceedings, p. 86. Berlin.
TOWNSEND, A. A. 1947 *Proc. R. Soc. Lond.* **A190**, 551.
TOWNSEND, A. A. 1949 *Austral. J. Sci.* **2**, 451.
TOWNSEND, A. A. 1956 *The Structure of Turbulent Shear Flow*. Cambridge University Press.
TOWNSEND, A. A. 1970 *The Structure of Turbulent Shear Flow*, 2nd edn. Cambridge University Press.
ÜBEROI, M. S. & FREYMUTH, P. 1969 *Phys. Fluids* **12**, 1359.
WYGNANSKI, I., OSTER, D. & FIEDLER, H. 1979 In *Proc. 2nd Symp. on Turbulent Shear Flows*, London.
YAMADA, H., KAWATA, Y., OSAKA, H. & KAGEYAMA, Y. 1980 Tech. Rep. Yamaguchi University, Japan, vol. 2, no. 4.
ZABUSKI, N. J. & DEEM, G. S. 1971 *J. Fluid Mech.* **47**, 353.

EFFECT OF SPATIALLY TRAVELING SINUOUS WAVES ON THE GROWTH OF A TWO-DIMENSIONAL TURBULENT WAKE

F. H. Champagne, B. Marasli, and I. Wygnanski

Department of Aerospace and Mechanical Engineering
University of Arizona, Tucson, AZ 85721, USA

The results of experiments to control the growth rate of a turbulent wake behind a flat plate will be presented. Sinuous disturbances at several amplitudes and frequencies were introduced to the wake by oscillating a small flap attached to the trailing edge of the plate. The Strouhal numbers of the perturbations were specially chosen so that the downstream location of the neutral point (where the spatial amplification rate obtained from linear stability theory vanishes) was well within the range of measurements. The streamwise evolution of these perturbation waves and their effect on the growth of the turbulent wake was investigated experimentally in a low turbulence level wind tunnel.

The flat plate is 30 cm long, 6.4 mm thick, and 61 cm wide. The leading edge is rounded and the trailing edge is tapered. Trip wires were placed on the plate to ensure that the boundary layers were turbulent. The flap is 5 mm long and is hinged to the trailing edge of the plate. The free stream velocity, U_∞ , was 7.5 m/sec and the resulting momentum thickness, θ , was 2.3 mm. The momentum thickness is defined by

$$\theta = \int_{-\infty}^{\infty} \frac{\bar{U}}{U_\infty} \left[1 - \frac{\bar{U}}{U_\infty} \right] dy$$

and is constant for the two-dimensional wake in a zero pressure gradient. The Reynolds number, based on θ , was 1000 and the wake was fully turbulent. Measurements of the velocity field were made using a rake of five X-wires. The velocity signals were decomposed into a mean part, f , a wave component, f' , and a fluctuating turbulent component, f'' [1]. Further details regarding the experimental facility can be found in Wygnanski, Champagne, and Marasli [2].

The streamwise variation of the half-width of the wake, L_0 , and the centerline velocity deficit, u_0 , are used to characterize the development of the mean velocity field. For the unforced wake, the flow is approximately self-preserving with $L_0 \sim x^{1/2}$ and $u_0 \sim x^{-1/2}$. Figure 1 shows $L_0 U_\infty / (u_0 \theta)$, a nondimensional growth parameter, plotted versus $x/2\theta$ for the unforced case and for a forcing frequency, f , of 70 Hz at several forcing amplitudes. θ remains effectively constant for these cases. The forcing levels are specified by the value of \tilde{u}_{rms} / u_0 at a given downstream location from the plate, $x = 25$ cm. For the cases labeled low, medium, and high amplitude, these values are 0.17, 0.30, and 0.89, respectively. The streamwise variation of the individual parameters L_0 and u_0^{-1} is similar to that of the nondimensional growth parameter. The unforced case shows linear behavior, as the L_0 / u_0 ratio is proportional to x , while the behavior of the forced wake depends on the amplitude level.

The rate of growth of the forced cases is initially larger than that for the unforced case. Depending on the level of forcing, however, the wake stops growing at some downstream location and appears to be in a state of nearly parallel flow. In the high-amplitude case, the wake even contracted some and then resumed growing at a slower rate. The downstream location where the wake stops growing in each case roughly corresponds to the location of the neutral point for that case. The exact location of the neutral point is difficult to determine, as nonlinear terms are not negligible near the end of the amplified

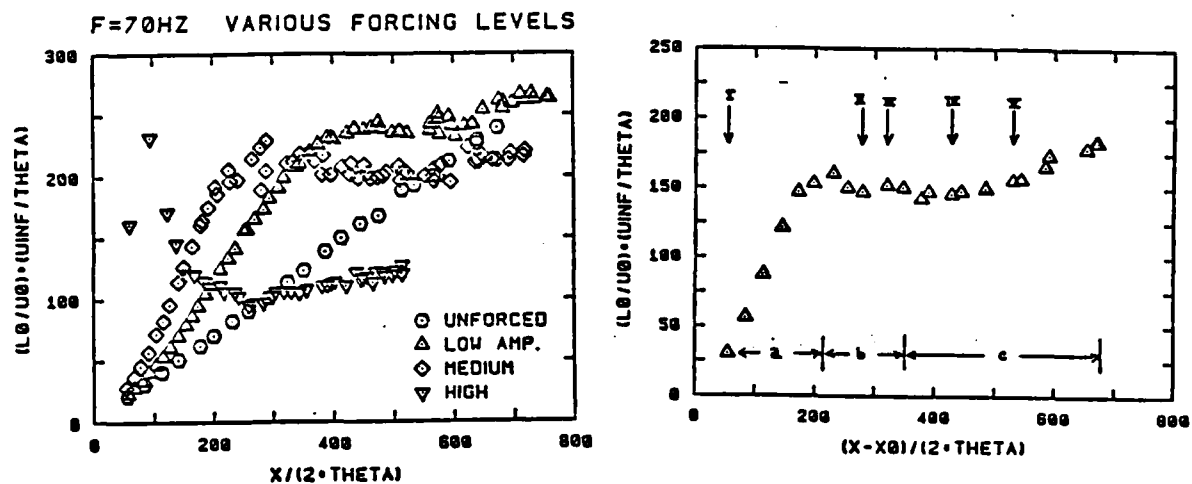


Fig. 1. The downstream development of the growth parameter for $f = 70$ Hz and various forcing levels.

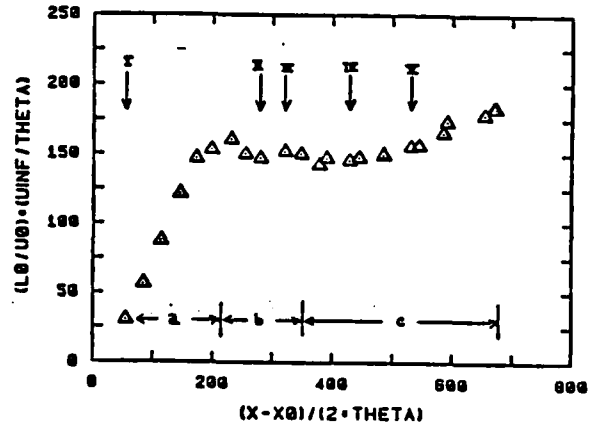


Fig. 2. The downstream evolution of the growth parameter for a medium amplitude forcing and $f = 80$ Hz. Downstream regions defined.

region. The variation in the growth rate of the wake is caused by the nonlinear interaction of the perturbation wave with the mean flow. In the region upstream of the neutral point, the disturbances are being amplified and energy is transferred from the mean flow to the disturbance. The wave-induced stress, $\bar{u}\bar{v}$, changes sign through the neutral point, so downstream of the neutral point energy is transferred from the disturbance to the mean flow. This demonstrates that the lateral rate of spread of the wake is closely linked with the growth of the disturbance wave; amplification of the wave results in a transfer of energy from the mean flow and a divergence of the mean flow. Further evidence to substantiate this can be obtained by noting that the initial divergence of the wake increases with increasing forcing amplitude. The contraction of the wake may be attributed to the transfer of energy from the disturbance wave to the mean flow in the damped region beyond the neutral point.

To consider some of the interesting features of the downstream development of a sinuous wave, let's examine the case of a medium-amplitude 80-Hz wave. Figure 2 shows the nondimensional growth variable $L_0 U_\infty / U_0 \theta$ versus $(x - x_0)/2\theta$. The measured mean velocity profiles for various downstream locations are presented in Fig. 3 in self-preserving form. Figure 3a shows the profiles for the downstream region labeled a. These profiles agree well with those for the unforced case shown by the solid curve, which represents a curve fit to the unforced profiles. The profiles for the region b, located just past the neutral point, differ from the unforced data, as shown in Fig. 3b. Farther downstream in region c, the changes are more significant. The three regions defined in Fig. 3 correspond to the amplified, neutral, and damped regions, respectively, in the context of linear stability theory.

Solution of the inviscid Orr-Sommerfeld equation using the appropriate measured mean velocity profile gives the eigenfunction distributions typical for each region. The amplitude and phase of the u and v components of the disturbance wave were computed. The phase of the u component changes sign in the damped region, while the phase of the v component does not change sign. Therefore, the sign of the wave-induced or coherent Reynolds stress changes in the neutral region. The computed wave-induced or coherent stress distributions are shown in Fig. 4. Four plots are presented for the neutral region showing the downstream evolution of the change in sign of the wave-induced Reynolds stress. The measured coherent, turbulent, and total Reynolds stress for the three regions are displayed in Fig. 5 for comparison. The vertical markers above the data presented in Fig. 2 indicate the measurement locations for the data shown. Three data sets are shown for the neutral region, demonstrating the change in sign of the coherent stress. Each distribution has been

normalized by the maximum value of the total stress corresponding to that downstream location, so the relative amount of coherent and turbulent stress can be determined. Figure 5a shows the measured stresses in the amplified region. Notice that the sign of the coherent stress is the same as that of the turbulent stress, while its magnitude is roughly twice that of the turbulent stress. In Fig. 5e, the measured stresses in the damped region c are presented. Note that the sign of the coherent stress has changed and its magnitude is now only one-third of that of the turbulent stress.

Further experimental results will be presented, along with comparison with linear stability theory predictions.

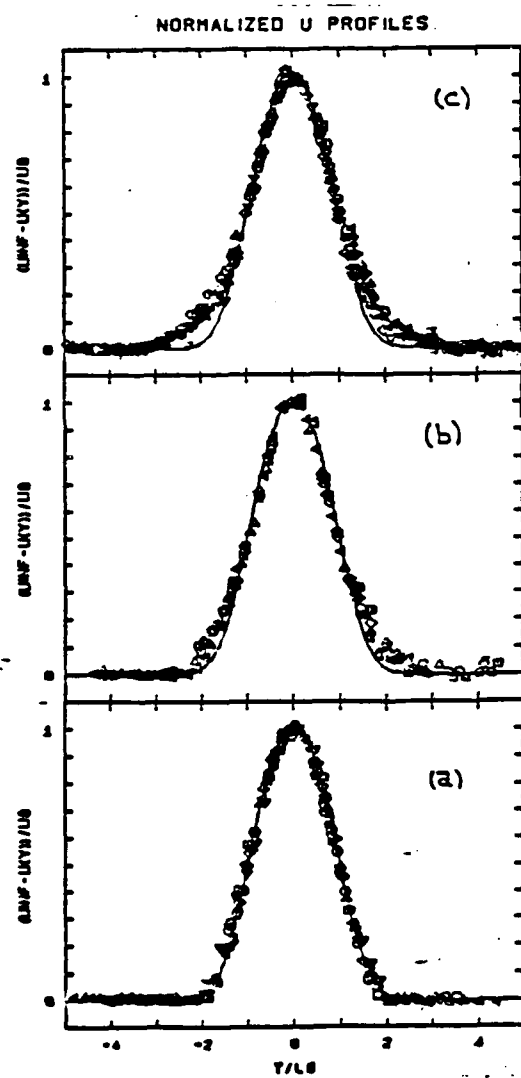


Fig. 3. Measured mean velocity profiles in the three defined regions: (a) the amplified region; (b) the neutral region; (c) the damped region.

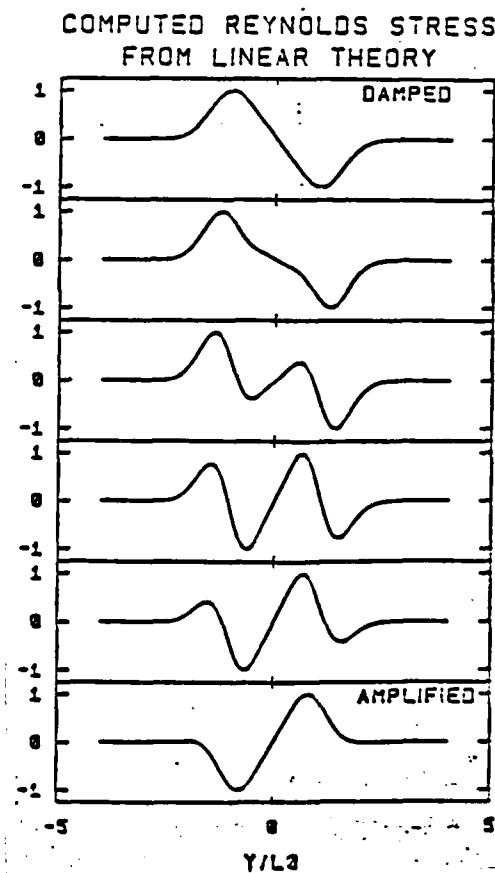


Fig. 4. Computed wave-induced Reynolds stress distribution for amplified, neutral, and damped regions for linear stability theory. Four plots are presented for the neutral region.

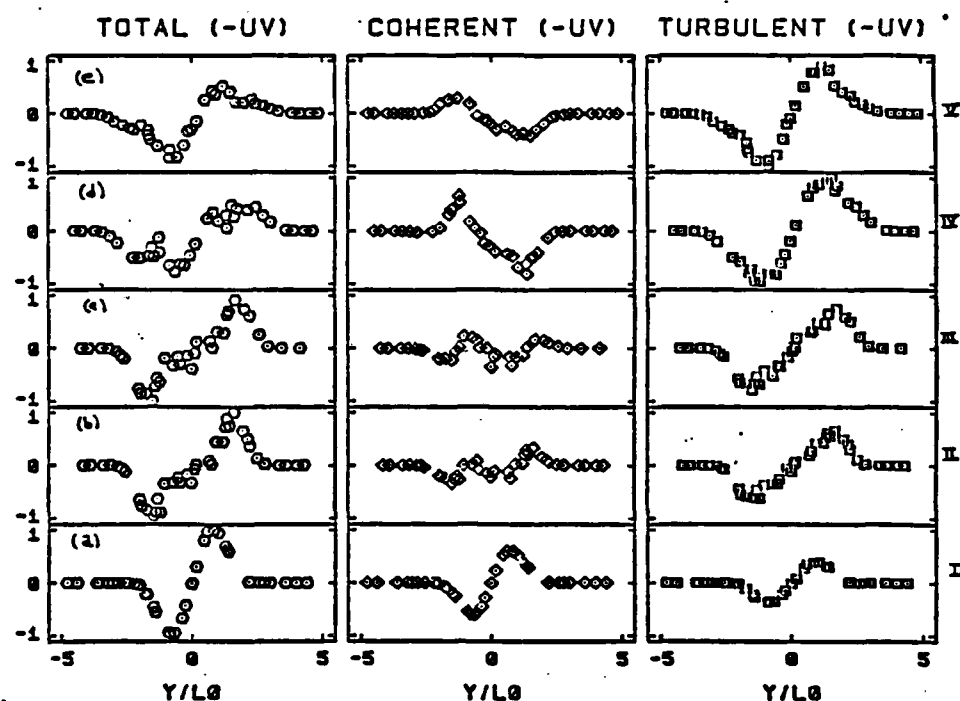


Fig. 5. Typical measured distributions of total, wave-induced or coherent, and turbulent Reynolds stresses for the downstream locations identified in Fig. 2.

References

- [1] Reynolds, W. C. and Hussain, A. K. M. F.: J. Fluid Mech. 54, 263 (1972).
- [2] Wygnanski, I., Champagne, F., and Marasli, B.: J. Fluid Mech. 168, 31 (1986).